Prussian Blue analogue materials for magnetic and energy storage applications



Maximilian Schart

St Edmund Hall

University of Oxford

A thesis submitted for the degree of

Doctor of Philosophy

Trinity 2023

Acknowledgements

I would like to extend my gratitude to my supervisor Prof. Mauro Pasta for giving me the chance to work in his research group. I am grateful for the plentiful advice and suggestions, as well as all the resources and opportunities that allowed me to conduct my research.

I would like to thank my college adviser Prof. Jeff Tseng, for the insightful discussions and your interest in my progress, both academic and personal.

I want to thank Dr Ramón Torres-Cavanillas for his help carrying out magnetic measurements and all the helpful discussions.

I am thankful to Dr Pascal Manuel and Dr Dmitry Khalyavin at the WISH beamline at the ISIS Neutron and Muon Source for neutron diffraction measurements and the introduction to Fullprof.

Thank you to the team at the Chemistry Teaching Labs for allowing me to access to their well-maintained instruments.

Dr Soochan Kim and Dr Krishnakanth Sada, thank you for everything you taught me about electrode castings and cell assembly.

Ruomu Zhang, thank you for carrying out TEM characterisation on my samples.

I want to thank the Prussian Blue analogues subgroup, especially Dr Samuel Wheeler and Dr Kevin Hurlbutt, from whom I've learned so much about this fascinating materials system, both experimentally and theoretically.

I would like to thank all my friends at the Pasta group for creating a supportive atmosphere both inside and outside the lab.

Dr Sophia De Sousa Coutinho, thank you for being a great instrument co-superuser and for keeping a light mood when there were issues.

Muyang Shi, thank you for being a terrific flatmate during the many lockdowns we've endured. The chats and laughs with you kept me sane.

Giulia, Brigita, Mu, Shobhan, Marco, Brandon and Alissa, I could not have hoped for better companions along this journey. I am grateful for every time you helped me out, lightened my mood and shared both good and difficult times with me. Your friendship is by far the most precious outcome of my last four years here.

I want to thank my family, my mother Anita, my father Manfred and my brother Andreas for your constant, unconditional support and encouragement every step of the way. None of this would have been possible without you.

To my partner Annika, thank you for always being there for me, for putting up with me being away for all these years and the countless times you cheered me up and made my life better. I am incredibly grateful and lucky to have you by my side.

Abstract

Upon its discovery in the 18th century, Prussian Blue, the first synthetic pigment, gained fame for its intense colour. Over the years since, many multifunctional properties have been discovered in its analogue materials. Members of the Prussian Blue analogue (PBA) family have shown promise for a wide variety of technological applications, ranging from energy and gas storage to catalysis and information storage. These materials have yielded room-temperature molecular magnetic materials as well as the currently most promising cathode materials for Na- and K-ion batteries. The diversity in applications of PBA materials can be attributed to their uniquely tunable structure and chemistry. Still, many compositions remain unexplored, largely due to challenges in their synthesis. This is especially true for air- and moisture-sensitive compounds. These issues have restrained the search for new PBA materials, including the highly desired first air-stable room-temperature molecular magnet and a PBA anode material that matches the high performance of current cathode materials.

The aim of this thesis is to widen the composition space of PBAs by using an optimised non-aqueous synthesis methodology. Vacancy-free chromium hexacyanochromate is targeted as one of the most promising compositions for both its magnetism and low-potential electrochemistry. This material is explored via a thorough physicochemical characterisation, as well as the discussion of its magnetic and electrochemical properties. A combination of magnetic measurements reveal that the magnetic ordering temperature is below room temperature, likely limited by the material's small particle size. In Na- and K-ion electrochemical cells, the material exhibits two reversible low-potential redox reactions, resulting in a high-capacity PBA anode material. Based on the success in the synthesis of chromium hexacyanochromate, the non-aqueous synthesis is extended to hexacyanoferrate-based PBAs. The approach successfully yields vacancy-less mixed-valence materials, which are usually unobtainable from standard syntheses. Furthermore, the results provide a deeper understanding of the PBA formation mechanism and the boundaries of the employed synthetic approach.

The work presented in this thesis provides important insights on the way towards molecular magnetic devices and future battery chemistries based on PBAs.

Contents

Publication list **viii**

1 Introduction **1**
1.1 Structural and electronic properties of Prussian Blue analogues . . . 2
1.1.1 Hexacyanometallate Complexes . . . 2
1.1.2 Prussian Blue analogues . . . 4
1.2 Synthesis of Prussian Blue analogues . . . 7
1.3 Applications of Prussian Blue analogues . . . 10
1.3.1 Molecular Magnets . . . 10
1.3.1.1 Principles of Magnetic Order . . . 11
1.3.1.2 Magnetic Interactions in Molecular Magnets . . . 15
1.3.1.3 Approaches to molecular magnetic materials . . . 17
1.3.1.4 PBAs as molecular magnets . . . 19
1.3.2 Electrochemical Energy Storage . . . 25
1.3.2.1 Working principle of batteries . . . 25
1.3.2.2 Electrode materials for Na- and K-ion batteries . . . 28
1.3.2.3 PBAs as electrode materials . . . 29
1.4 Thesis objectives . . . 35

2 Methods **37**
2.1 Physicochemical characterisation . . . 38
2.1.1 Powder X-ray and neutron diffraction . . . 38
2.1.1.1 Working principle . . . 38
2.1.1.2 Experimental setup . . . 41
2.1.2 Fourier-transform infrared spectroscopy . . . 42
2.1.2.1 Working principle . . . 42
2.1.2.2 Experimental setup . . . 43
2.1.3 Simultaneous thermal analysis . . . 43
2.1.3.1 Working principle . . . 43
2.1.3.2 Experimental setup . . . 45
2.1.4 Inductively coupled plasma elemental analysis . . . 45
2.1.4.1 Working principle . . . 45

2.1.4.2 Experimental setup . . . 47
2.1.5 Scanning electron microscopy . . . 48
2.1.5.1 Working principle . . . 48
2.1.5.2 Experimental setup . . . 49
2.2 Magnetic characterisation . . . 49
2.2.1 Superconducting quantum interference device magnetometer 49
2.2.1.1 Working principle . . . 49
2.2.1.2 Experimental setup . . . 50
2.2.2 Temperature-dependent magnetisation . . . 51
2.2.3 Field-dependent magnetisation . . . 53
2.3 Electrochemical characterisation . . . 54
2.3.1 Electrode preparation . . . 54
2.3.1.1 Main considerations . . . 54
2.3.1.2 Experimental procedure . . . 55
2.3.2 Two- and three-electrode cells . . . 56
2.3.2.1 Working principle . . . 56
2.3.2.2 Experimental setup . . . 58
2.3.3 Voltammetry . . . 59
2.3.4 Galvanostatic cycling . . . 60
2.4 Other methods . . . 61
2.5 Chemicals . . . 62

3 Optimised synthesis and characterisation of chromium hexacyanochromate 64
3.1 Abstract . . . 64
3.2 Motivation . . . 65
3.3 Synthesis of reduced chromium hexacyanochromate . . . 69
3.4 Chemically oxidised chromium hexacyanochromate . . . 77
3.5 Synthesis of mixed-valence chromium hexacyanochromate . . . 84
3.6 The oxidation states of chromium hexacyanochromate . . . 86
3.7 Conclusion . . . 90
3.8 Experimental . . . 90

4 Magnetic and electrochemical properties of chromium hexacyanochromate 93
4.1 Abstract . . . 93
4.2 Motivation . . . 94
4.3 Magnetic properties . . . 97
4.4 Electrochemical properties . . . 106
4.4.1 K-ion cells . . . 107

4.4.2 Na-ion cells . . . 113
4.5 Conclusion . . . 116
4.6 Experimental . . . 117

5 Non-aqueous synthesis of transition metal hexacyanoferrates 118
5.1 Abstract . . . 118
5.2 Motivation . . . 119
5.3 Reduced-state materials . . . 121
5.4 Mixed-valence materials . . . 122
5.5 Conclusion . . . 130
5.6 Experimental . . . 131

6 Conclusion and outlook 133
6.1 Conclusion . . . 133
6.2 Outlook . . . 135

References 138

Publication list

Schart, M.; Wheeler, S.; Torres-Cavanillas, R.; Hurlbutt, K.; Manuel, P.; Khalyavin, D.; Zhang, R.; Volonakis, G.; Bogani, L.; Goodwin, A. L.; Pasta, M. Non-aqueous synthesis of vacancy-free chromium hexacyanochromate. (in preparation)

Schart, M.; Pasta, M. Vacancy-suppressing effect of solvents in Prussian Blue analogues. (in preparation)

Olbrich, L. F.; Xiao, A. W.; Schart, M.; Ihli, J.; Sanghadasa, M.; Pasta, M. Iron Fluoride Lithium Metal Batteries in Ionic Liquid Electrolytes. *Advanced Energy Materials* (submitted)

Galatolo, G., Alshangiti, O., Di Mino, C., Matthews, G., Xiao, A. W., Rees, G., Schart, M., Chart, Y., Pasta, M. Advancing fluoride-ion batteries with a Pb-PbF2 counter electrode and a diluted liquid electrolyte. *ACS Energy Letters* (under review)

Torres-Cavanillas, R.; Chen, H.; Schart, M.; Jagger, B.; Pinilla, E.; Castells-Gil, J.; Pasta, M.; Bogani, L. Field Effect Transistors from a two-dimensional artificial carbon allotrope. (in preparation)

1 Introduction

Contents

1.1 Structural and electronic properties of Prussian Blue analogues 2
1.1.1 Hexacyanometallate Complexes 2
1.1.2 Prussian Blue analogues 4
1.2 Synthesis of Prussian Blue analogues 7
1.3 Applications of Prussian Blue analogues 10
1.3.1 Molecular Magnets 10
1.3.2 Electrochemical Energy Storage 25
1.4 Thesis objectives 35

This chapter introduces Prussian Blue analogues (PBAs), a family of crystalline inorganic materials studied in this thesis. Prussian Blue (PB), a blue pigment with chemical composition $Fe[Fe(CN)_6]_{3/4}$, was discovered in the early 18th century as the first synthetic pigment,[1] however its structure and chemistry hadn't been unambiguously resolved until the 1970s.[2] Works on PBAs, materials which possess the Prussian Blue-type crystal structure, but whose Fe centres are at least partially replaced by other transition metals, started soon after the discovery of PB.[3] Today, a wealth of PBAs with different compositions are known. This tunability gives rise to materials with vastly different physicochemical properties, which has fuelled research on PBAs in several directions, beyond fundamental characterisation to

battery electrode materials,[4, 5] molecular magnets,[6] gas storage, wastewater treatment, biomedical applications, catalysis and others.

The following section introduces the most important aspects governing the composition, crystallography and electronic structure of PBAs. Afterwards, the most common synthetic schemes are introduced. Lastly, the implications of the resulting physicochemical aspects on the magnetic and electrochemical properties of PBAs are discussed. Given the large amount of published work, this chapter cannot encompass all aspects of PBA research, but rather aims to lay out the concepts required for the understanding of the thesis.

1.1 Structural and electronic properties of Prussian Blue analogues

PBAs are classical examples of coordination polymers, in which transition metal centres are bridged by cyanide ligands. Hexacyanometallates can be regarded as the monomers of these materials. When these are combined with transition metal cations acting as linkers, three-dimensional extended crystals form. This section focuses on the origin of the physicochemical properties of PBAs from monomer to coordination polymer.

1.1.1 Hexacyanometallate Complexes

Hexacyanometallates $M(CN)_6{}^{i-6}$ are complexes in which a (usually charged) transition metal atom M^{i+} is coordinated by six terminal cyanide ligands. The $C{\equiv}N^-$ ligands bond strongly and highly covalently to the the transition metal centre via the carbon end.[7, 8] Cyanide thereby possesses both σ-donating and π-accepting qualities.[9] Through σ electron donation, cyanide ligands stabilise transition metals in high oxidation states.[9] On the other hand, π-backbonding provides a means of charge delocalisation through the overlap of the metal's d_{xy}, d_{xz} and d_{yz} orbitals with the ligands' π^* antibonding orbitals. This effect removes electron density from the metal and strengthens the metal-carbon bonds, while weakening the carbon-nitrogen bond within the ligand. Because of the negative charge carried

by $C{\equiv}N^-$, this electron removing effect is less pronounced as for the isoelectric CO or NO^+, however strong enough to stabilise transition metals in low oxidation states. The ligands arrange octahedrally around the central transition metal. As described by ligand field theory, this octahedral coordination geometry affects the degeneracy of the transition metal's d-orbitals. π backbonding lowers the energy of the three orbitals with t_{2g} symmetry, thus stabilising them. On the other hand, electron repulsion effectively raises the energy of the two e_g orbitals, giving the latter a strongly antibonding character. In the case of cyanide as ligand, this octahedral energy splitting Δ_{oct} is large, which is reflected in its classification as strong ligand in the spectrochemical series.[10] This bonding environment defines the complexes' physical and chemical properties.

Firstly, it enables a wide variety of $M(CN)_6{}^{i-6}$ compositions, with M=V, Cr, Mn, Fe, Ru, Co, Pt, Pd and Ir being reported. For reasons stated above, also a wide range of oxidation states is stabilised. Unusually low oxidation states are found in $M{=}Cr^0$,[11] while the highest are found in $M{=}Mn^{IV}$, Pt^{IV} and Pd^{IV}.[12] Interestingly, even at low oxidation states, the ligand field stabilisation is usually sufficient to prevent the complex from dissociating from the high electrostatic repulsion between the negatively charged ligands. A noteworthy exception to this is $Cr(CN)_6{}^{4-}$, which will be discussed in section 3. So far, no stable hexacyanometallate with e_g electrons are known, which underlines their highly antibonding nature.

Secondly, hexacyanometallates generally assume a low-spin electronic ground state. This is a result of their large Δ_{oct}, which is usually greater than the electron pairing energy.

Thirdly, the d-orbital splitting gives rise to the observation of Jahn-Teller distortions in hexacyanometallates. This effect describes the spontaneous contraction or elongation of metal-ligand bonds, which averts degenerate electronic configurations and lowers the electronic ground state energy.[13, 14]

Further consequences include the occurrence of d-d electron transitions under absorption of photons, which typically lies in the visible range and gives these complexes their colour.

1.1.2 Prussian Blue analogues

Since the cyanide anion is a bidentate ligand, hexacyanometallates can be polymerised by transition metal ions coordinating to the nitrogen ends of the ligand. In order to provide maximum ligand field stabilisation, also these N-coordinated transition metal centres are octahedrally coordinated by cyanide ligands. The so-created three-dimensional coordination polymers are called PBAs. Compared to the C-coordinated transition metal centres, the N coordination creates a weaker ligand field, giving the bonds a weakly covalent and dominantly ionic nature.[15] As a result, Δ_{oct} are about three times lower and N-coordinated transition metals are often, but not exclusively, in a high-spin electron configuration.[15]

In order to explain structural and electronic features in detail, we need to look into the range of possible compositions. The general formula of PBAs is

$$\mathrm{A}_x\mathrm{P}^i[\mathrm{R}^j(\mathrm{CN})_6]_{1-y} \cdot z\,\mathrm{Sol}, \tag{1.1}$$

where P^i and R^j are the nitrogen- and carbon-coordinated transition metal centres, respectively, A are inserted ions (usually alkali metal ions), and Sol are solvent molecules (usually $\mathrm{H_2O}$). These constituents make up a typically face-centered cubic crystal structure, which is shown in fig. 1.1.[16] P and R transition metals occupy the corners of the subcubes and are bridged by cyanide ligands. The length of the cyanide ligands opens up large interstitial sites of about 3 Å diameter[17] which are connected in three dimensions by wide channels along the $\langle 100\rangle$, $\langle 010\rangle$ and $\langle 001\rangle$ directions, which makes the structure of PBAs resemble an open framework.[18] A cations occupy these interstitial sites of the structure. y quantifies the amount of hexacyanometallate vacancies in the structure. This structural feature has wide implications on the physicochemical properties of PBAs and will be in the centre of attention throughout this thesis. z is the amount of solvent molecules Sol present in the structure. Solvent molecules are present in two distinct positions: zeolitic solvent in the interstices, and coordinated solvent bonded to the undercoordinated P transition metals surrounding vacancies. The insertion of A cations and the occurrence of $\mathrm{R(CN)_6}^{j-6}$ vacancies are a consequence of the necessary

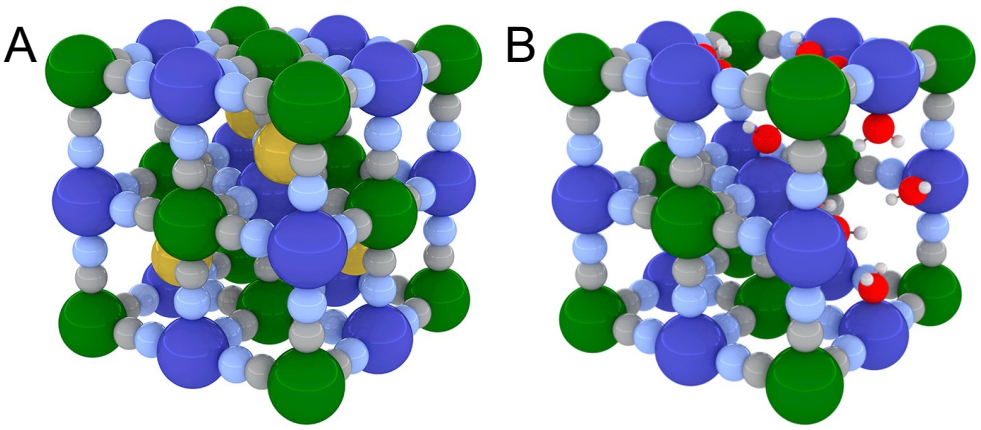


Figure 1.1: Schematic PBA structure. P (dark blue), R (green), C (grey) and N (light blue), A^+ atoms and water molecules (red and white). Cation-inserted structure (A); Structure with hexacyanometallate vacancies and coordinated water molecules (B). Adapted with permission from [4]. Copyright 2018 Elsevier Inc.

charge neutrality in the material. If the oxidation states of P and R do not fulfill $i + j = 6$, as it is the case for reduced and mixed-valence PBAs, ion insertion and vacancy formation provide means to compensate for the excess negative charge carried by the $C{\equiv}N^-$ ligands. Which of the two charge neutrality mechanisms is assumed and what is the driving force behind them, is not fully understood. However, their sensibility to synthesis conditions was discovered early, with findings of 'soluble' Prussian Blue $KFe[Fe(CN)_6]$ or 'insoluble' Prussian Blue $Fe[Fe(CN)_6]_{3/4}$ when the precursor ratios are altered.[19, 20]

All of the features of the PBA composition are subject to a large variability, which is why materials with vastly different physicochemical properties are achievable. Reported A species include alkali metal cations from Li^+ to Cs^+, as well as $NH_4{}^+$. The R species include the aforementioned transition metals found already in the hexacyanometallate complexes, V, Cr, Mn, Fe, Ru, Co, Pt, Pd and Ir. On the P site, the variety is even larger, with V, Cr, Mn, Fe, Co, Ni, Cu, Zn, Cd, In and others having been reported. P and R can assume various oxidation states, which further adds to PBAs' chemical complexity. Because of the ionic bonding to the cyanide ligand, the P sites' e_g orbitals have a less antibonding quality, which is why the occupation of these orbitals is allowed and does not destabilise the materials. Chemically, however, the weaker bonding to the cyanide ligands makes

the P transition metal a point of attack for ligand substitution reactions, which causes the instability of PBAs in basic environments.[21, 22]

Crystallographic parameters and deviations from the prototypical cubic $Fm\bar{3}m$ crystal structure are a result of the interplay of bonding and electrostatic interactions in the material. As such, they are highly dependent on the P and R site species, amount and nature of inserted A cations and presence of $R(CN)_6{}^{j-6}$ vacancies and solvent molecules. The lattice parameter is largely dependent on the metal-ligand bonding, in particular the backbonding abilities of the R transition metal covalently bonded to the $C{\equiv}N^-$ ligand, as well as the polarising power of the ionically bonded P transition metal, given by the extent of its Lewis acidity.[23] These factors are dependent on the elemental nature as well as the oxidation state of the transition metals. This instance allows for the commonly used determination of oxidation states of PBAs via vibrational spectroscopy of the cyanide stretch frequency.[24–26]

In PBAs, there are several effects which can lead to symmetry-lowering distortions of the crystal structure.[27] Due to the octahedrally coordinated transition metals, certain PBAs are prone to cooperative Jahn-Teller distortions. This effect has been observed in PBAs in which P has an uneven electron occupation of its e_g orbitals, e.g. in the case of Cu^{2+} and Mn^{3+}. In PBAs with a low fraction of vacancies y, the local contractions and elongations of the individual metal-ligand bond lengths align, i.e. they become cooperative. This leads to a global distortion of the crystal lattice along one axis, lowering the symmetry to tetragonal.[28–32] It is noteworthy that a low vacancy content is a prerequisite for the Jahn-Teller distortions to become cooperative. In the high-vacancy PBAs $Cu[Fe(CN)_6]_{2/3}$, $Cu[Co(CN)_6]_{2/3}$ and $Li_xMn[Fe(CN)_6]_{0.83}$, the structure remains cubic.[31, 33–36] This indicates a 'buffering' function of vacancies against the cooperativity of this effect by accommodating individual distortions. Another common type of distortions in PBAs arises from the electrostatic interactions between inserted A^+ cations and the anionic $C{\equiv}N^-$ ligands. The attractive force pulls inserted ions in the interstitial sites off-centre along the $\langle 111 \rangle$ direction in order to minimise distance. This is typically accompanied by tilts of the $R(CN)_6{}^{6-j}$ octahedra which lowers the crystal

symmetry to typically rhombohedral or monoclinic in PBAs with high Li^+, Na^+ or K^+ content.[37–40] The larger A=Rb^+ and Cs^+ activate this distortion less, because of their smaller charge density and the resulting weaker polarisation.[41, 42]

The wide composition space and unique crystallographic and electronic structures lead to a wealth of unique properties and effects, such as a small-polaron-type electron conduction[43, 44], electrochromism,[45, 46] negative thermal expansion,[47, 48] optically induced charge transfer[49, 50], magnetic superexchange interactions[6, 51] and reversible electrochemical redox coupled with storage of even large ions such as Cs^+.[4, 52] What has boosted the exploration of PBAs is that much of this variability is achieved via facile synthetic methods, which will be discussed in the following section.

1.2 Synthesis of Prussian Blue analogues

Over the years, many synthetic methods have been developed to achieve PBAs of different composition, vacancy content, crystallinity and morphology. The vast majority of studies uses one of three main types of synthetic approaches:

- Precipitation reaction of hexacyanometallate complexes or simple cyanides with transition metal ions,
- Electrodeposition including electrophoresis and electroplating,
- Decomposition of hexacyanometallate complexes.

Precipitation syntheses make use of the high solubility of precursors and insolubility of PBAs, commonly in water. The formation reaction takes the general form

$$x\,\mathrm{A}^+ + \mathrm{P}^{i+} + (1\text{-y})\,\mathrm{R(CN)_6}^{j-6} + z\,\mathrm{Sol} \longrightarrow \mathrm{A}_x\mathrm{P}^i[\mathrm{R}^j(\mathrm{CN})_6]_{1-y} \cdot z\,\mathrm{Sol}. \qquad (1.2)$$

We know from classical nucleation theory that at a critical concentration the precipitate nucleates spontaneously.[53] The solubility limit of PBAs is very low, which means that saturation is reached quickly. In experiments, PBA materials often crash out of solution immediately after mixing the precursor solutions. This

means that using practically relevant concentrations, the concentration of PBA constantly jumps over the critical concentration upon mixing, thus forming new nucleates. Because of the low critical concentration, only small amounts of ions are present to grow the nucleates. Therefore, in this nucleation-dominated regime PBAs with non-uniform and small particle sizes form (see fig. 1.2A). These materials often exhibit high contents of hexacyanometallate vacancies because of the fast reaction and the kinetic advantage of vacancy formation over ion insertion. This kinetic effect can be lifted by increasing the concentration of counterions during synthesis, leading to decreased vacancy concentrations.[30, 42, 54–57] In recent years, the use of chelating agents has proven effective in controlling crystallite growth. Chelated P^{i+} ions need to detach from the chelant before they can react, which results in a slow release of precursors. This way, the concentration of free P^{i+} stays low throughout the synthesis, which can increase the particle growth stage. As a result, larger particles with a more uniform distribution have been achieved.[40, 58] Because the de-chelation step becomes rate-limiting, kinetic differences in the charge neutrality mechanisms become irrelevant and the resulting material assumes its thermodynamically favoured structure, rather than the kinetically favoured highly vacant state. Many examples show that for reduced materials ($i + j = 4$), this is the low-vacancy structure, while mixed-valence materials ($i + j = 5$) still form with a high vacancy concentration.[59] For the synthesis of materials where the $R(CN)_6{}^{j-6}$ complex is not obtainable, PBAs can be precipitated from transition metal ions and simple cyanides, forming the hexacyanometallate as reaction intermediate. To avoid the formation of materials with mixed P and R site compositions, this is often used for P = R PBAs[57] or for materials where the metals can only occupy one site in the structure.[60] Overall, precipitation syntheses allow for high tunability, given by the choice of reaction conditions such as temperature, precursor concentrations and ratios, additives, mixing rate, stirring speed, solvent, volume and others. The downside to this large parameter space, however, is given by challenges regarding reproducibility.

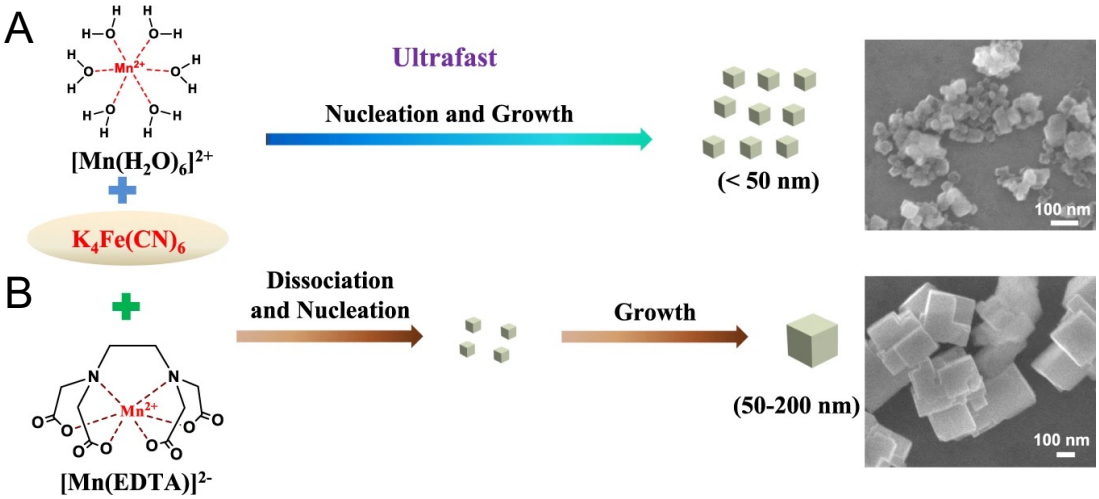


Figure 1.2: Comparison of precipitation syntheses of manganese(II) hexacyanoferrate(II) without (A) and with EDTA as chelating agent (B). Larger, uniform particle sizes are achieved by using the chelant, as shown in SEM images. Adapted with permission from [61]. Copyright 2021 the authors.

Another widely employed synthesis technique for PBAs is electrodeposition. Usually, a method based on electrophoresis is used. The technique requires a conductive surface (electrode) which is immersed in an electrolyte solution containing the same precursors used in precipitation synthesis, but in high dilution (usually $\approx 1\,\mathrm{mM}$), so that negligible spontaneous nucleation occurs. By periodically changing the potential of the electrode, precursors move toward the surface due to electrostatic forces, where they nucleate and grow. This way, PBA thin films are achieved. The electrode potential presents an important parameter to choose. When the potential crosses the reduction or oxidation potential of one or several of the dissolved precursors, their oxidation states can change before material formation, which leads to the often unwanted coexistence of different phases.[62–65] This, however, can be made use of for the synthesis of PBAs from precursors in unreactive oxidation states, in a technique resembling electroplating. For this kind of electrodeposition, the electrode potential is typically kept at a constant, reductive or oxidative potential with respect to the present transition metal species. Precursors reduce or oxidise at the electrode surface, which can enhance their reactivity and lead to PBA formation. For both kinds of electrodeposition, results show that this technique lacks control over the morphology, crystallinity and vacancy content of the formed

materials, with parameters like choice of electrode material dramatically altering the materials' structure.[66, 67]

A more niche synthesis technique is based on the partial decomposition of hexacyanometallate complexes. For this synthesis, a $R(CN)^{j-6}$ complex is decomposed often via the addition of a concentrated strong acid (usually HCl), releasing free R^{j+} ions which react with intact complexes to form a PBA. This method is often referred to as "single metal source" synthesis because of the presence of a single transition metal salt. Obviously, only PBAs with a P = R composition can be achieved this way. So far, this synthesis has been used to produce PB, Prussian White and Berlin Green particles of high crystallinity and uniform morphology, caused by the slow release of free ions.[68–71] Apart from the limitation on accessible compositions, the release of toxic free CN^- is a drawback of this method.

1.3 Applications of Prussian Blue analogues

Since their early discovery, PBAs have shown promise in a large variety of applications. Among them are the fields of molecular magnetism, which became intensely studied in the 1990s, when high magnetic ordering temperatures were discovered in PBAs,[6] and energy storage, which led to the commercialisation of a PBA cathode material in sodium-ion batteries.[72] These two applications are the focus of this thesis and are introduced in the following sections.

1.3.1 Molecular Magnets

Magnetic materials are at the heart of numerous modern technologies from information storage to medical treatments, from motors to sensors. In many applications, permanent magnets on the basis of alloys are employed because of their robust magnetisation, high ordering temperatures and scalable preparation by means of metallurgy.[73–75] A more recent class of magnetic materials are molecular magnets, which include organic and metal-organic compounds.[76] These materials are synthesised by low-temperature chemical processes and possess unique, highly tunable features. The property of interest in this work is the high-temperature

collective magnetic ordering in PBAs. It has been in the centre of attention in the magnetic research on PBAs due to its importance for applications. Research in this field has shown promising results, discovering PBA materials which are among the highest-ordering molecular magnets in general.[77]

1.3.1.1 Principles of Magnetic Order

Magnetic properties of materials are classified by their response to magnetic fields. We can group materials into three broad categories: diamagnetic, paramagnetic and magnetically ordered. Diamagnetism is a weak effect describing the orientation of small induced magnetic dipoles antiparallel to the external field that caused it. This effect appears to some degree in all materials, however is usually weak enough to only be of concern in compounds with only completely filled orbitals, where none of the other types of magnetism are present. When atoms in a material possess half-filled electronic orbitals, they act as magnetic dipoles because of the presence of unpaired electrons. In contrast to the induced magnetic moment in a diamagnetic material, these dipoles persist in the absence of a magnetic field. Their magnetic moment is a result of the orbital $\mathbf{L}$ and spin angular momentum $\mathbf{S}$ of the atoms' electrons, which couple to the total angular momentum $\mathbf{J} = \mathbf{L} + \mathbf{S}$ with the total angular momentum quantum number J. In paramagnetic materials, these magnetic dipoles interact weakly enough to be considered independent. In the absence of an external magnetic field, their magnetic moments are randomly oriented. When an external field is applied, the individual magnetic dipoles line up parallel to the applied field, to an extent depending on the field strength. Magnetically ordered materials also possess atoms with unpaired electrons. In contrast to paramagnets however, they are strongly interacting. These interactions lead to magnetic order in the absence of an external field. The most common types of magnetic order are ferromagnetism, where magnetic moments are aligned in parallel, ferrimagnetism, where magnetic moments are in antiparallel alignment but do not compensate each other, and antiferromagnetism, where magnetic moments are in antiparallel alignment and compensate fully. All magnetical order is lost above a transition temperature,

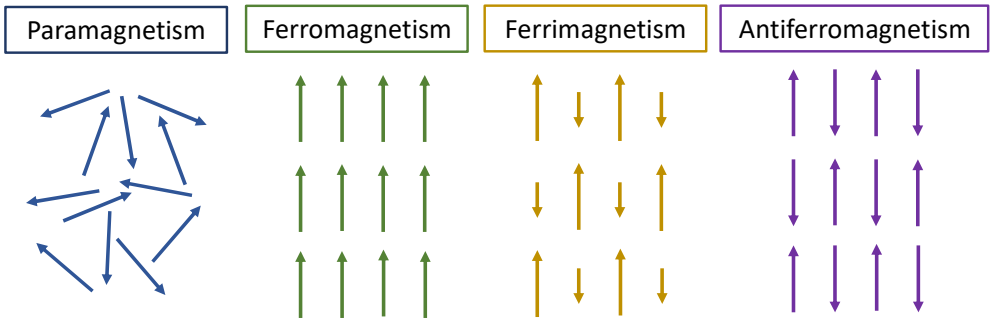


Figure 1.3: Schematic spin orientation in different magnetic materials.

which is characteristic for a given material. The critical temperature is called Curie temperature T_C for ferromagnets and ferrimagnets and Néel temperature T_N for antiferromagnets. Above this temperature, thermal fluctuations become dominant and destroy the magnetic order, leaving the material in a paramagnetic state.[78] A schematic of the spin orientation in different magnetic materials is shown in fig. 1.3.

The different types of magnetic behaviour can be determined by magnetic measurements. Central to the discussion of magnetic properties is the material's response to an external magnetic field H, described by its magnetic susceptibility χ:

$$\chi = \frac{dM}{dH} \approx \frac{M}{H}, \tag{1.3}$$

where M is the measured magnetisation. In the limit of $H \to \infty$, the magnetisation approaches the saturation magnetisation M_{sat}. For a material with n equal magnetic moment carriers, it is given by

$$M_{sat} = ng\mu_B \mathsf{J}, \tag{1.4}$$

where g is the Landé g-factor, μ_B is the Bohr magneton and J is the total angular momentum quantum number. Measuring the saturation magnetisation thus allows for the quantification of spin centres n.

The types of magnetism can be discriminated by their characteristic temperature-dependent susceptibility curves. In paramagnetic materials, χ decays with increasing temperature T as described by the Curie Law

$$\chi = \frac{C}{T}, \tag{1.5}$$

where C is the material-specific Curie constant (per mole) given by

$$C = N_A g^2 \mu_B^2 \mathsf{J}(\mathsf{J}+1)/3k_B, \tag{1.6}$$

with the Avogadro number N_A and the Boltzmann constant k_B. If the interactions of magnetic dipoles with each other are considered, as must be done for magnetically ordered materials, the temperature dependent susceptibility deviates from the Curie Law. In the Weiss model, the effect of interacting magnetic dipoles is captured by a mean molecular field, which has proven to often agree with experiments. From this model, we get the following expression, known as the Curie-Weiss law, for χ above the materials' critical temperature, i.e. in the paramagnetic region:

$$\chi = \frac{C}{T - \Theta}, \tag{1.7}$$

where Θ is the Weiss constant or Weiss temperature. Θ contains information about the type and strength of magnetic dipole interactions within a material. For a compound with a single species of interacting magnetic dipoles, the Weiss constant is defined by[79]

$$\Theta = \frac{zJ\mathsf{J}(\mathsf{J}+1)}{3k_B}, \tag{1.8}$$

where z is the number of interacting nearest neighbours and J is the exchange interaction parameter (also called exchange constant or exchange integral), which describes the strength of intermolecular interactions between spin centres and will be further studied in section 1.3.1.2. If $\Theta > 0$ (i.e. $J > 0$), the material is ferromagnetic and $\Theta = T_C$. If $\Theta < 0$, (i.e. $J < 0$), the interactions are antiferromagnetic and Θ is expected to be T_N. For $\Theta = 0$, equation 1.7 collapses to the Curie Law (equation 1.5) and the material is paramagnetic. The Curie-Weiss law is usually evaluated in χ^{-1} *vs* T plots. The typical responses of antiferromagnetic, paramagnetic and ferromagnetic materials are shown schematically in fig. 1.4. Ferrimagnetic materials generally have a more complex χ *vs* T behaviour because of their multiple molecular fields acting on the individual magnetic sublattices.[78, 80]

The behaviour of ordered materials below their critical temperature is determined by their ordering type. When a ferro- or ferrimagnetic material is cooled to below

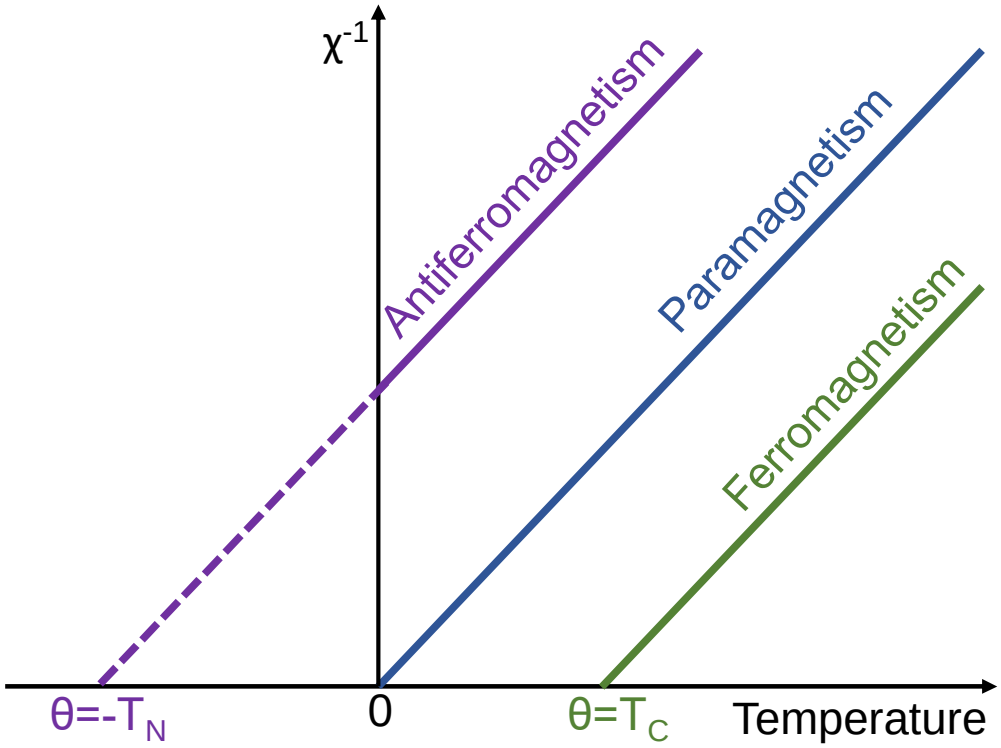


Figure 1.4: χ^{-1} *vs* T behaviour of different magnetic materials. According to the Curie-Weiss law, the Weiss temperature can be determined via linear interpolation to $\chi^{-1} = 0$, which allows for the determination of critical temperatures.

T_C, its magnetic dipoles and domains suddenly and spontaneously align collectively along one axis, usually a so-called 'easy axis' for which the magnetic alignment is lowest in energy. Since the magnetic moments do not cancel each other out in these materials, this alignment causes the susceptibility to jump to a macroscopic positive value at the Curie temperature. While the shape of χ *vs* T is similar for ferro- and ferrimagnets, they can be distinguished by the characteristic shape of their χT *vs* T plots. In ferrimagnetic materials, a characteristic minimum in χT can be observed above T_C, which is absent in ferromagnetic materials.[81–83] In the case of antiferromagnetic materials below T_N, the magnetic dipoles assume their ground state antiparallel arrangement and cancel each other such that the net magnetisation is zero. The exchange interactions lock this arrangement in place, resulting in a low susceptibility. In this region, χ is dependent on the direction of the applied field with respect to the axis along which magnetic dipoles are arranged.

Apart from M_{sat}, C, T_C and T_N, other important parameters commonly used to

describe magnetic behaviour are the remnant magnetisation M_{rem}, the coercive field H_c and the blocking temperature T_b. As discussed above, ferro- and ferrimagnetic materials maintain a non-zero magnetisation after an aligning external magnetic field is switched off. The magnetisation at this point, *i.e.* $H = 0$ is called the remnant magnetisation M_{rem}. In order to demagnetise an ordered material, an opposing external field needs to be applied. The field strength needed to decrease the magnetisation to $M = 0$ is called the coercive field H_c. It is a measure of how robust a material's magnetisation is against magnetic perturbation. Both M_{rem} and H_c are important for the description of magnetically ordered materials.

Throughout this work, we will solely be concerned with 3d transition metals in crystal field environments. In this case, the interaction with ligands quenches the spin-orbit coupling introduced at the beginning of this section. This phenomenon is known as 'orbital quenching' and results in a orbital contribution of $\mathbf{L} = 0$ to the total angular momentum $\mathbf{J}$ which determines the magnetic moment of an atom. Therefore, the magnetic moment of an orbital-quenched atom is simply $\mathbf{J} = \mathbf{S}$, the total spin carried by the atom's i electrons, $S = \sum_i m_{s,i}$. In the following chapters only the case of $\mathbf{J} = \mathbf{S}$ will be carried forward.

1.3.1.2 Magnetic Interactions in Molecular Magnets

One might think that the molecular field leading to magnetically ordered materials stems from the purely classical magnetic interactions between dipoles. However, simple approximations make evident that the magnetic dipolar interactions between adjacent magnetic moments are too weak to account for ordering temperatures significantly above 1 K.[78] The dominant interaction causing the high molecular fields and thus leading to high-temperature ordering phenomena is called exchange interaction. It arises from quantum mechanical effects of electron interactions and is a direct effect of the fermionic nature of electrons, which forbids wavefunctions which behave symmetric under particle exchange. The spin-dependent part of the Hamiltonian for such a system can be described in the Heisenberg model via

the phenomenological Hamiltonian

$$\hat{H} = -\frac{1}{2}\sum_{ij} J_{ij}\mathbf{S_i}\cdot\mathbf{S_j}, \tag{1.9}$$

where J_{ij} is the general exchange interaction parameter between any two spin centres i and j, that appeared in equation 1.8 before. We can see from this relation that J is in fact a central parameter which determines the type of ground state magnetic ordering as well as its robustness against thermal fluctuations. As such, it is central to the research of high-temperature ordering in magnetic materials.

We can use the refined mean field theory by Néel to determine the temperature-dependence of magnetic order. In materials with two interpenetrating sublattices A and B of respectively identical spin carriers, where each atom in A is coordinated by z atoms in B, and interactions with next-nearest neighbours can be neglected, equation 1.8 takes the form[84]

$$T_{critical} = \frac{z|J|\sqrt{S_A(S_A+1)S_B(S_B+1)}}{3k_BT}, \tag{1.10}$$

where the critical temperature $T_{critical}$ is T_N for antiferromagnets, and T_C for ferro- and ferrimagnets, respectively. Equation 1.10 clearly identifies three key parameters to tune in order to achieve a desired ordering temperature: the number or nearest neighbours z, the spin on each sublattice S_i and the exchange interaction parameter J. Conceptually, modifying z and S is straightforward and poses solely synthetic challenges. To manipulate J, we need to understand the underlying electronic orbital interactions in more detail.

The relationship between magnetic orbital symmetry and exchange constant J has been studied by Kahn[85–87], Hoffmann[88] and Noodleman[89]. Although quantitatively differing[90], the three models arrive at the same qualitative outcomes: the exchange constant between two electrons on neighbouring sites J_i consists of a ferromagnetic and antiferromagnetic contribution:

$$J_i = J_{i,FM} + J_{i,AF}. \tag{1.11}$$

Here, $J_{i,FM}$ is > 0 and favours parallel alignment of neighbouring electron spins, whereas $J_{i,AF}$ is < 0 and favours antiparallel orientation. $J_{i,AF}$ becomes more

negative when the overlap between the interacting orbitals increases.[91–93] From this relation and simple orbital geometry, we can deduce a very useful, qualitative rule for the exchange interaction between electrons on neighbouring octahedrally coordinated transition metals: interactions between orthogonal e_g – t_{2g} orbitals have zero overlap and therefore are ferromagnetic ($J_i > 0$), whereas t_{2g} – t_{2g} interactions are antiferromagnetic ($J_i < 0$) in nature. In compounds where two neighbouring spin centres possess n_A and n_B uncoupled electrons, respectively, the total exchange constant J is the sum of all individual orbital interactions over all i pathways,[6]

$$J = \left(\sum_i J_i \right) / n_A n_B. \tag{1.12}$$

This relation, combined with the above equation 1.10 identifies additional strategies to modify a material's ordering type and critical temperature. If the aim is a ferromagnetic material with maximum T_C, the number of ferromagnetic e_g – t_{2g} interaction must be maximised, while antiferromagnetic t_{2g} – t_{2g} interactions are to be avoided.[6] For an antiferromagnetically coupled material with maximum ordering temperature, the ideal case is vice versa. Combining these insights allows for the design of molecular magnetic materials with tailored properties.[94, 95]

1.3.1.3 Approaches to molecular magnetic materials

Several different approaches have been developed to exploit molecular magnetic properties. A first discrimination can be made between single-molecule magnets (SMMs) and molecule-based magnets (MBMs). SMMs comprise discrete molecular entities with a single or a cluster of spin carriers.[96] Their magnetic properties have a purely molecular origin, while long-range magnetic interactions are absent.[97] This chemistry has gained interest for their quantum mechanical properties such as quantum tunneling and magnetic anisotropy, which lend these material promising for *e.g.* spintronics applications.[98–100] In order to achieve long-range magnetic order with high ordering temperatures, however, this approach is unsuitable.

For this goal, MBMs have been investigated. MBMs are materials of different dimensionalities that are typically formed from molecular building blocks and contain

a large number of spin carriers. In contrast to SMMs, the magnetic properties of MBMs are governed by long-range magnetic interactions, thus enabling cooperative magnetic order. Several approaches to MBMs have been established, which can be categorised as organic, organometallic or inorganic, depending on the nature of the spin carriers.[97, 101]

In organic magnets, the spin arises purely from half-filled p orbitals.[97] Magnetic ordering has been reported in a number of these radicals, with the highest reported ordering temperature being 36 K in a sulfur-nitrogen radical.[102] Although the mechanisms are well understood, the necessities of close contact (to ensure strong magnetic interaction) and stabilisation of the radical remain challenges that have been limiting the ordering temperatures of purely organic materials.[103] The organometallic approach combines spin-carrying organic building blocks with transition metal spin centres. In these materials, organic radicals are used as anionic spin carriers, while the cationic spin carriers can be either organometallics such as metallocenes (organometallic-radical approach) or bare metal ions (metal-radical approach).[97, 104] Ordering temperatures achieved via the organometallic-radical approach are comparatively low, with a T_C of 8.8 K reported for a manganocenium-based tetracyanoethylene (TCNE) compound.[105] In contrast, the metal-radical approach has been much more successful in reaching high ordering temperatures. This group of materials include the two room-temperature molecular ferrimagnets $V^{II}[TCNE]_x$ ($x \approx 2$), a non-stoichiometric, amorphous compound with an ordering temperature of 400 K,[106, 107] and a crystalline chromium(II)-pyrazine compound ordering at 242 °C,[108] currently the highest ordering temperature reported for a molecular magnet. Both these compounds are highly air-sensitive, possibly limiting their applicability. Lastly, an inorganic approach to molecular magnetic materials can be taken. Here, metallic spin carriers are linked and held in place by non-magnetic organic ligands.[97, 101] The magnetic interactions between linked spin centres are typically governed by a superexchange mechanism via the bridging ligand. Although a variety of ligands has been studied, cyanide has shown to be an especially suitable choice, for reasons discussed below.[109, 110] A wide range

of ordering temperatures have been reported for cyanide-bridged materials, the highest of which, 376 K, found in a V–Cr PBA.[111] This compound and the above mentioned organometallics are the only known molecular magnets exhibiting room-temperature ordering known to date.

1.3.1.4 PBAs as molecular magnets

The magnetic properties of PB were first studied by Davidson and Welo as early as 1928 with the aim of understanding the structure and electronic state of the material.[112] Magnetic ordering in PBAs was discovered in the 1950s and 1960s through the early works by Bozorth *et al.*,[113] Holden *et al.*[114] and Ito *et al.* [115] in PBAs of various compositions, finding Curie temperatures between 3 K in a material prepared from Co^{2+} and $Co(CN)_6{}^{3-}$ up to 50 K in a PBA prepared from Mn^{2+} and $Mn(CN)_6{}^{3-}$.[113] These early results hint at the wide range of ordering temperatures achievable for different PBA compositions.

Because of their octahedral coordination and often equal nearest-neighbour distance, PBAs are regarded as 'textbook' materials to apply the orbital models introduced above to. Although the presence of deviations from the prototypical cubic crystal structure can influence the exchange interaction,[116] PBAs follow the simple rules of orthogonality and overlap discussed above.[117] Because of the large separation of spin centres of ≈ 5 Å, magnetic ordering arises from ligand-mediated superexchange interactions between the P and R sublattices. Next-nearest neighbour interactions are weak in PBA materials, which can be seen from the low ordering temperature of PB, 5.6 K, which only possesses magnetic orbitals on the P sublattice.[115, 118] They are therefore usually neglected and equation 1.10 can be applied to these materials with excellent agreement. The superexchange interaction is mediated via the cyanides' σ and π electron delocalisation mechanisms, which has been studied extensively.[117, 119–122] It has been found that antiferromagnetic interactions are mainly mediated by means of electron delocalisation onto the cyanide ligands' π^* antibonding orbitals.[123] Therefore, more diffuse, higher-energy t_{2g} orbitals in lower-charged transition metal centres enable more efficient backbonding,

which leads to stronger antiferromagnetic orbital interactions. Therefore, the strongest orbital interactions J_i are expected for PBAs with early 3 d transition metals in lower oxidation states.

From equation 1.12 we know that not only the strength of individual orbital interactions, but also the number of ferro- and antiferromagnetic interaction pathways are crucial. Because the carbon-coordinated R can only possess t_{2g} electrons, the following three situations arise:[6]

1. In case P has solely e_g magnetic orbitals, the interactions with the t_{2g} magnetic orbitals of R are ferromagnetic, $J_i > 0$. All interaction pathways are ferromagnetic, therefore the overall exchange is ferromagnetic ($J > 0$). This situation is apparent when P is in a d^8 or d^9 configuration.

2. When P possesses only t_{2g} magnetic orbitals, the interactions with the t_{2g} magnetic orbitals present on R are antiferromagnetic, $J_i < 0$. All interaction pathways are antiferromagnetic, therefore the overall exchange is antiferromagnetic ($J < 0$). This is the case for a P electron configuration of d^2 or d^3.

3. If both e_g and t_{2g} magnetic orbitals are present on P, some of the interaction pathways with the t_{2g} orbitals of R are ferromagnetic, $J_i > 0$, while the others are antiferromagnetic $J_i < 0$. This case is more complex, as the type of magnetic ordering, i.e. the sign of J depends on the individual orbital exchange integrals J_i, as well as the respective numbers of ferro- and antiferromagnetic pathways. This situation arises for P configurations of d^4 through d^7.

Fig. 1.5 shows the electronic configurations of 3 d transition metal ions known to form magnetic PBAs in either the P site, R site or both. All above considerations provide us with a framework to identify the key parameters, which are the d-electron configurations and oxidation states of P and R, the number of coordinated magnetic neighbours z and, to a lesser degree, the spins S_P and S_R, to predict the magnetic

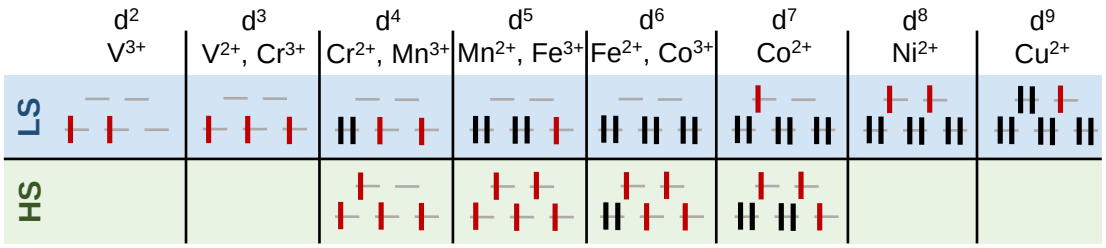


Figure 1.5: Electronic configuration of 3*d* transition metals in low-spin (blue box) and high-spin (green box) known to form magnetic PBA materials. Electrons in half-filled (magnetic) orbitals are indicated in red, whereas compensated orbital electrons are shown in black.

properties of PBAs and use the wide range of accessible compositions to design materials with tailored magnetism.

The validity of the arguments presented above is apparent when compared to experimental findings. PBAs with P=Ni^{II} and Cu^{II} fall into the first category, where all interactions are ferromagnetic. Experiments confirm that all such materials are in fact ferromagnets.[124–129] Studies on ferromagnetic PBAs are scarce and existing results do not give a clear answer on the influence of the number of ferromagnetic interaction pathways on the ordering temperature. Because of the different numbers of uncoupled e_g electrons, one expects twice as many ferromagnetic pathways for P=Ni^{II} PBAs as for P=Cu^{II} and therefore higher ordering temperatures. While this has been confirmed for R=Fe^{III}[125, 128, 130], results for R=Cr^{III} are inconclusive.[6, 124, 130]

In PBAs with P=V^{II}, V^{III} or Cr^{III}, the second situation arises and one expects solely antiferromagnetic interactions. Experimental results show that these materials are indeed ferrimagnetic.[83, 111, 131–134] So far, perfect spin compensation has not been achieved experimentally, which is why no PBA antiferromagnet has been reported.

As expected, the third case, where both ferro- and antiferromagnetic orbital interactions are present, requires a more diversified look. This category of materials comprises PBAs with P=Mn^{II}, Fe^{II} and Co^{II}. In experiments, these materials show vastly different results. It was found that Mn^{II} in the P site results in ferrimagnetic materials.[28, 123, 128, 135–137] Co^{II} exhibits antiferromagnetic order

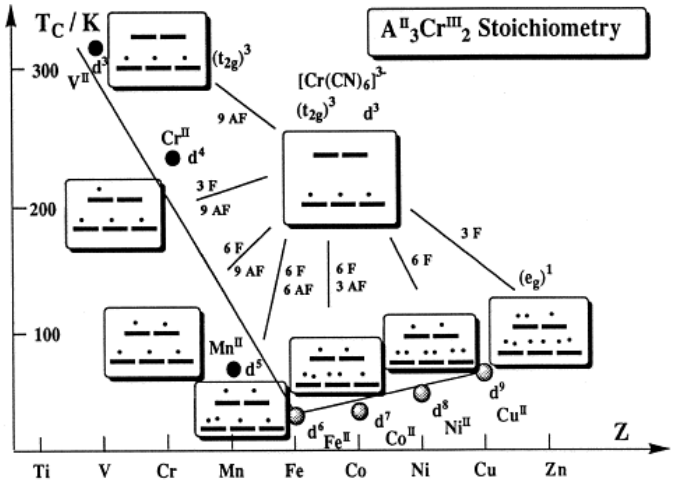


Figure 1.6: Ordering temperature in $P^{II}[Cr^{III}]_{2/3}$, P= V, Cr, Mn, Fe, Co, Ni and Cu. The found ordering temperature is strongly dependent on the number of ferromagnetic (F) and antiferromagnetic (AF) pathways. Reprinted with permission from [110]. Copyright 1999 Elsevier Science S.A.

with R=Fe^{III},[128, 138, 139], but ferromagnetic order with R=Cr^{III}.[140, 141] Fe in the P site leads to ferromagnetic materials.[142–145] These materials' magnetic behaviours are determined by their different amounts of ferro- and antiferromagnetic interaction pathways. Because the respective interactions correspond to exchange parameters J_i of opposite sign, these materials typically exhibit lower ordering temperatures compared to the purely ferro- or antiferromagnetic cases (see equation 1.12 and fig. 1.6). It is noteworthy that a number of these materials show stimuli-responsive magnetism. Because of the 'tug of war' between ferro- and antiferromagnetic contributions, their magnetic properties can be sensitive to small changes in the electronic structure. It has been shown that stimuli such as irradiation with visible light, changes in humidity or pressure, can lead to macroscopic changes in the magnetisation, ordering temperature and type.[143, 144, 146–149]

The effect of increased backbonding is confirmed by comparing the isoelectric compounds $Cs_2Mn[V^{II}(CN)_6]$, $Cs_2Mn[Cr^{III}(CN)_6]$ and $Cs_2Mn[Mn^{IV}(CN)_6]$. When going from R= V^{II} to the higher charged Mn^{IV}, the materials' ordering temperature decreases from 125 K, over 90 K to 49 K,respectively.[28, 123, 136]

Lastly, comparing highly vacant PBAs with vacancy-free materials of same elemental composition allows us to examine the effect of coordination on the

magnetic ordering temperature. Equation 1.10 indicates a proportional dependence of T_C on z. Experimental studies on nickel(II) hexacyanochromate(III) and manganese(II) hexacyanochromate(III) agree with this relation, finding 90 K for both the low-vacancy materials $CsNi[Cr(CN)_6]$ and $CsMn[Cr(CN)_6]$, which is close to the theoretical value of 6/4 times the values for the highly vacant $Ni[Cr(CN)_6]_{2/3}$ and $Mn[Cr(CN)_6]_{2/3}$, which are 60 K and 66 K, respectively.[6, 28, 124]

In short, the presented theories correctly describe and predict magnetic properties of PBAs and therefore present a robust framework to target specific compositions. These theories have enabled the search for high ordering temperatures, which presents one of the crucial requirements towards the applicability of devices incorporating magnetic PBAs. It is immediately clear that on the R site, a d^3 configuration is desirable to achieve high ordering temperatures. It possesses the maximum number of uncoupled electrons in the t_{2g} orbitals, resulting in $S = 3/2$. Because of the difficulties in preparing the extremely air-sensitive $V(CN)_6^{4-}$, usually the easy-to-source and stable $Cr(CN)_6^{3-}$ is used as precursor. The optimal choice of P depends on the desired ordering type (ferro- or antiferromagnetic). In either case, the number of interaction pathways of the desired type needs to be maximised, while at the same time avoiding the other.

The highest ordering temperature for a ferromagnetic material was found experimentally in $CsNi[Cr(CN)_6]$, which possesses the ideal magnetic electronic configuration of $e_g^2 - t_{2g}^3$, resulting in the maximum possible $2 \cdot 3 = 6$ ferromagnetic pathways. The T_C found for this material is 90 K. It is apparent that ferromagnetic ordering is not a viable way to achieve room-temperature magnetic ordering in PBAs. The focus has therefore shifted to antiferromagnetically coupled PBAs. This has resulted in numerous attempts to achieve vacancy-less vanadium(II) hexacyanochromate(III), which has a magnetic electronic configuration of $t_{2g}^3 - t_{2g}^3$, and therefore the maximum number of $3 \cdot 3 = 9$ antiferromagnetic interaction pathways.[111, 132, 133, 150, 151] The current record is held by $KV[Cr(CN)_6]$ synthesised using a sol-gel method, exhibiting a T_C of 376 K (see fig. 1.7A).[111] Although the reported composition leads to assume an ideal material, the material

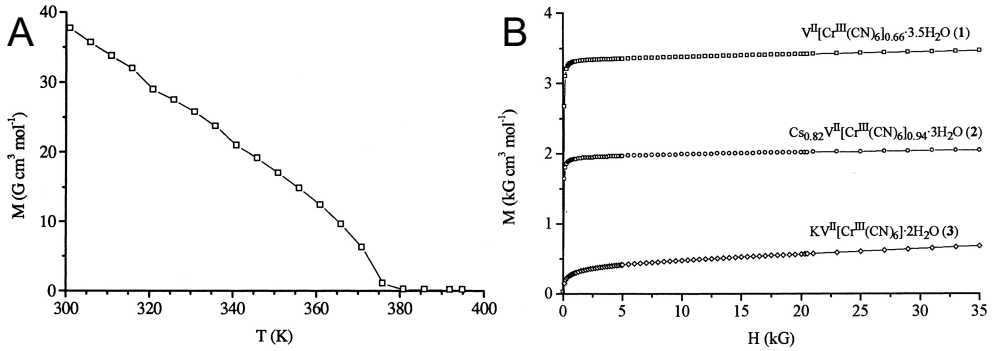


Figure 1.7: Magnetic properties of KV[Cr] synthesised by a sol-gel method. Temperature-dependent magnetisation measurements (A) reveal an ordering temperature of 376 K. Field-dependent magnetisation of KV[Cr] and related compounds (B), showing a non-zero saturation magnetisation indicating deviations from the ideal stoichiometry. Adapted with permission from [111]. Copyright 1999 American Chemical Society.

does not possess the ideal stoichiometry. This circumstance is manifested in a non-zero remnant magnetisation, corresponding to a vacancy content of 4% or oxidation of 12% of the V^{II} centres, as shown in fig. 1.7B. The synthesis of this composition is elusive and typically leads to materials of low crystallinity or amorphous structure. Since these efforts by Holmes and Girolami in 1999, no notable improvements on high-T_C magnetic PBAs could be made. Because of the presence of divalent vanadium, the compound and its precursors are very sensitive to oxidation in air. Conflicting results on the magnetic ordering temperature of the vanadyl-compounds formed upon oxidation in air have been reported, with Hatlevik *et al.* claiming T_C stays at 372 K after extended air and oxygen exposure,[133] whereas according to Ferlay *et al.*, the ordering temperature drops to 115 K.[152] Recently, Hu *et al.* presented a strategy to encapsulate particles in a polymer matrix, thus protecting the material from oxidation.[153]

Vanadium(II) hexacyanochromate(III) still remains as the only PBA composition with a magnetic ordering temperature above room temperature. It currently ranks as the material with the third highest T_C, after a recently discovered Cr^{II}-pyrazine based compound ($T_C = 515$ K)[108] and $V^{II}[TCNE]_x$ ($T_C \approx 400$ K).[106, 154–156] All of these materials are extremely air-sensitive, thus possibly limiting their applicability.

1.3.2 Electrochemical Energy Storage

Work on the electrochemistry of PBAs started with studies on PB and ruthenium purple, first demonstrating the redox activity of PBAs.[157–161] By the early 2000s, the electrochemical properties of a number of hexacyanoferrate compositions were known,[162] however only in the 2010s were PBAs targeted as novel chemistry for rechargeable batteries. By now, PBAs are regarded as one of the most promising electrode materials families for Na-ion and K-ion batteries,[4, 163, 164] fields which have gained much interest due to the forecasted problems in the supply of raw materials for Li-ion batteries.[165]

As discussed in section 1.1, the cyanide ligand environment allows the transition metals P and R to adopt different oxidation states without loss of structure. This builds the basis of the use of PBAs as active materials in electrochemical energy storage applications. Before looking at the unique qualities of PBAs as battery electrode materials, the basic working principle of batteries is briefly introduced.

1.3.2.1 Working principle of batteries

Batteries are electrochemical energy storage systems that use the thermodynamics of redox reactions to provide usable electric energy. In spontaneous redox reactions, reactants change their chemistry under exchange of electrons to form a thermodynamically more stable state. Such processes often release large amounts of energy, examples for which are burning of rocket fuel or explosives. In batteries, the constituent reduction and oxidation reactions happen at the cathode and anode, respectively, which are spatially separated. When reduction and oxidation reactions are isolated, the respective charge transfer between the two so-called half-reactions cannot take place, leading to a polarisation which immediately stops the reactions from proceeding. Only when the two reactions are ionically connected via a common ionic conductor, the electrolyte, and electronically connected by an electric circuit, can the reaction continue. The reaction stops when all reactants of at least one of the half-reactions have undergone the transition to their more stable chemistry. The total amount of electrical charge that can be carried from the anode to the

cathode is called the capacity of the battery. For better comparison, the capacity is usually normalised via the mass or volume of the system, described by the specific capacity and volumetric capacity, respectively. Multiplying these numbers with the average voltage between the anode and cathode gives the amount of energy stored in the system per unit mass or volume, referred to as the specific energy and the volumetric energy density. The voltage under standard conditions, E^0, is determined by the thermodynamics of the two half-reactions, precisely the Gibbs free energy of reaction ΔG^0 via:

$$E^0 = \frac{\Delta G^0}{zF}, \tag{1.13}$$

where z is the number of electrons transferred per reaction and F is the Faraday constant. This relation is dependent on both reactions, which is impractical for the study of individual half-reactions. For this reason, reaction potentials are reported with respect to a reference counter-reaction. This can be done purely mathematically by subtracting the potential difference between the experimental counter-reaction and the chosen reference from the measured voltage, or experimentally through the choice of the physical reference electrode. E^0 for a large number of reactions have been measured and are available. The potential of the reaction $2\,H^+ + 2\,e^- \rightleftharpoons H_2$ at standard conditions, the so-called standard hydrogen electrode (SHE), is defined as 0 V by the IUPAC and is usually used as a universal reference in tables of standard potentials.[166] This way, the voltage in an electrochemical cell can be expressed as the difference between the potentials of the reduction and oxidation reactions:

$$E_{\text{cell}} = E_{\text{red}} - E_{\text{ox}}. \tag{1.14}$$

When a current is drawn from a battery, the usable voltage is lowered due to losses in the cell. These are caused by a variety of processes, such as interfacial charge transfer, ionic transport and ohmic processes and others, all of which require so-called overpotentials to achieve a certain current.[167, 168]

In secondary batteries, the reduction and oxidation reactions need to be practically reversible. Since there is a decrease in Gibbs free energy during battery

discharge that drives the reaction (see equation 1.13), the back-reaction possesses a $\Delta G > 0$, which means that energy must be spent to charge a battery. The required charging voltage is higher than the equilibrium potential difference of the electrode reactions, again due to the required overpotentials. These losses during discharge and charge lead to a voltage hysteresis which is the cause of energy efficiencies $< 100\%$.

Another important metric describing batteries is the coulombic efficiency (CE). It is defined as the ratio between the discharge capacity and charge capacity of a battery. CEs above 100% can arise from side reactions involving electron exchange, while CEs below 100% show capacity loss. The CE is often employed to quantify the degradation of battery cells per cycle and is therefore an indicator for the cycle life.

In modern Li-ion batteries, the cell components comprise a lithiated graphite anode, often a layered transition metal oxide cathode, and an electrolyte consisting of a Li^+ salt dissolved in organic carbonate-based solvents. During discharge, Li^+ ions are extracted from their positions in graphite interlayers, travel through the electrolyte and intercalate into the cathode material. During charge, this process is reversed and Li^+ shuttles from the cathode and intercalates into the anode. The anodic reaction happens at a potential of about 0.1 V, while the cathode reaction has a potential of around 4 V, both *vs* Li^+/Li, leading to an overall cell voltage of around 3.9 V.[169] These insertion-type Li-ion batteries power many of the daily used mobile devices, from cell phones to electric vehicles. However, this cell chemistry cannot satisfy the requirements set by all different fields of applications where energy storage is needed. The importance of factors such as cost, energy density, specific energy, cycle life, calendar life, power density, safety, abundance and others varies vastly between different applications. This has caused battery science to not only focus on reaching higher energy densities or specific energies *e.g.* by increasing cell voltage and atom utilisation, but rather to spread out and find alternative chemistries excluding scarce elements and hazardous compounds.

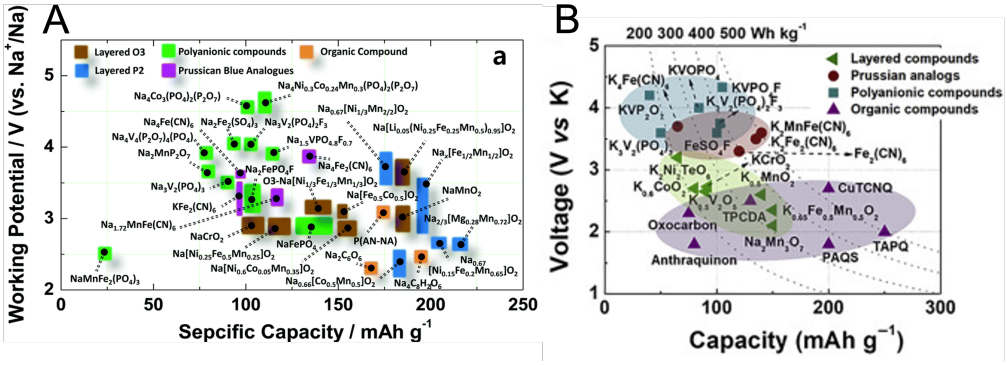


Figure 1.8: Comparison of leading cathode chemistries for NIBs (A) and KIBs (B). (A) Adapted from ref. [174] with permission from the Royal Society of Chemistry. (B) Adapted from [171] Copyright (2019), with permission from Elsevier.

1.3.2.2 Electrode materials for Na- and K-ion batteries

Na-ion and K-ion batteries (NIBs and KIBs) are emergent technologies fuelled by the desire to move away from the constricted raw materials supply for Li-ion batteries.[170] The change to inserting ions with larger ionic radii imposes challenges to the electrode materials used. The suitability of a wide range of chemistries for both cathode and anode materials has been investigated and the most promising candidates are summarised here.

In both NIBs and KIBs, the most promising cathode chemistries are based on (layered) transition metal oxides, polyanionic compounds and PBAs. The state-of-the art materials in each category are sodium/potassium manganese oxides (with or without transition metal substitutions), sodium/potassium vanadium phosphate and fluorophosphate and the PBAs $A_2Mn[Fe(CN)_6]$ and $A_2Fe[Fe(CN)_6]$, respectively.[164, 171–173] Their performance varies with use of the two inserting ions, as summarised in fig. 1.8.

In high-energy density cells, these cathodes are coupled with a low-potential anode, cycled in an organic electrolyte. For these applications, carbon-based anode materials are regarded as the most promising chemistry.[164] In KIBs, potassiated graphite shows a high capacity of 260 mA h g^{-1} at an average voltage of 0.3 V *vs* K^+/K with high high rate capability and cycle life.[175] The inability of Na^+ ions to intercalate into graphite prevents the use of the same material for NIBs.[176]

However, the amorphous hard carbon shows favourable performance in NIBs. With a capacity of up to $410\,\mathrm{mA\,h\,g^{-1}}$ and an average voltage of $0.3\,\mathrm{V}$ *vs* $\mathrm{Na^+/Na}$, hard carbon is regarded as the leading anode in high-energy density NIBs.[177, 178]

In applications where rate capability, cycle life, cost and safety arguments justify a penalty in energy density, the use of aqueous electrolytes can be beneficial. Due to the limited stability window of water, the carbon-based materials mentioned above are unsuitable as anode in aqueous NIBs and KIBs. In aqueous NIBs, sodium titanium phosphate is considered promising due to its capacity of $123\,\mathrm{mA\,h\,g^{-1}}$ and a potential of around $-0.6\,\mathrm{V}$ *vs* SHE.[179, 180] However, it suffers from a low rate capability which is a consequence of its low electronic conductivity.[181] Other approaches include organic compounds or vanadium oxides as possible anodes in aqueous NIBs. Compared to the Na-ion counterpart, research into aqueous KIBs is still at an early stage. Tests with potassium titanium phosphate showed a capacity of $78\,\mathrm{mA\,h\,g^{-1}}$ at a potential of around $-0.8\,\mathrm{V}$ *vs* SHE.[182] Organic compounds, vanadium oxides and alloys are also investigated as possible anode materials for aqueous KIBs.[183]

The compositional variability of PBAs opens up the possibility of using this chemistry as both cathode and anode in NIBs and KIBs. This way, the high rate capability of PBA materials in aqueous electrolytes can be utilised fully, which can enable high-rate batteries. Such a cell was demonstrated by Pasta *et al.*, who combined a $\mathrm{K_{0.05}Cu[Fe(CN)_6]_{0.67}}$ cathode with a $\mathrm{K_{0.11}Mn[Mn(CN)_6]_{80.83}}$ anode in an aqueous $\mathrm{Na^+}$ electrolyte.[18] The PBA full cell exhibited an energy efficiency of $84.2\,\%$ at a rate of $50C$ without measurable capacity loss after 1000 cycles. These results encourage the search for PBA compositions with high-capacity low-potential redox, as outlined below.

1.3.2.3 PBAs as electrode materials

PBAs have been identified as promising electrode materials for rechargeable batteries as they combine several desirable qualities. First, they exhibit a high specific capacity for ion storage with materials exhibiting up to three redox processes per formula

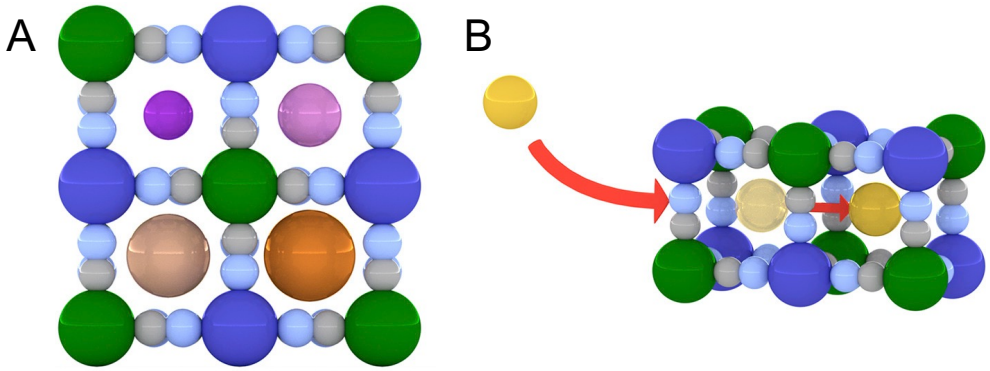


Figure 1.9: Schematic of relative sizes of (clockwise from top left) Li^+, Na^+, Rb^+ and K^+ in the PBA interstices; ionic diffusion channels through the material along the ⟨100⟩ direction. Adapted with permission from [4]. Copyright 1999 Elsevier Inc.

unit.[57, 184] Second, their large interstitial sites and diffusion channels along the ⟨100⟩ direction allow for the insertion and fast mobility of larger ions, leading to high rate capabilities with ions such as Na^+ and K^+ (see fig. 1.9). Third, due to their open framework structure, they exhibit minimal lattice distortions and strain upon cycling, which results in high reversibilities and long cycle lives. Lastly, the facile and scalable synthesis of a large variety of PBA compositions allows for low-cost cathode materials based on abundant elements.

The insertion of ions into PBAs follows the reduction of a transition metal centre as a charge balance mechanism. Analogous to the as-synthesised materials, inserted ions occupy the interstitial sites within the sub-cubes of the PBA. When the material is subsequently oxidised, the inserted ion leaves the structure again in a reversible process. It is apparent that the ability of P and R to undergo reversible redox reactions dictate the electrochemical properties of the material.

An early work by Scholz and Dostal demonstrated how varied the redox behaviour of different PBA compositions is.[185] They showed that the redox potential of R in the PBA is closely related to the potentials of the dissolved $R(CN)_6^{j-6}$ complex. The materials under investigation were based on the complexes $Fe(CN)_6^{3-/4-}$, $Cr(CN)_6^{3-/4-}$ and $Mn(CN)_6^{3-/4-}$, which possess reduction potentials of 0.344 V, −1.140 V and −0.240 V *vs* SHE in solution, respectively. However, the potentials of R in the materials lie about 300 mV to 800 mV higher than the dissolved complex.

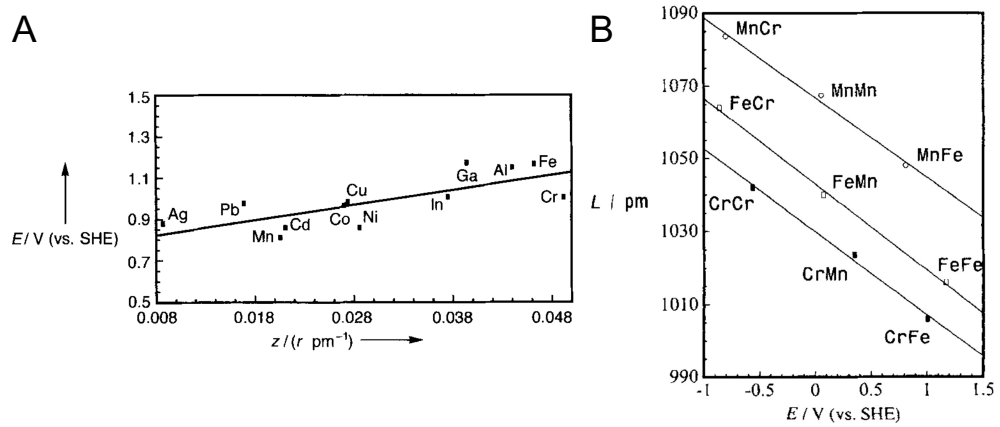


Figure 1.10: Dependence of the formal electrochemical potentials of hexacyanoferrate-based PBA materials on the charge/radius ratio of the P-site species (A); variation of electrochemical potential and lattice parameter (L) with PBA composition. Adapted with permission from [185]. Copyright 1996 VCH Verlagsgesellschaft mbH.

The authors found a statistically significant correlation between the formal potentials of transition metal hexacyanoferrates with the P site's ionic potential, which is given by its charge divided by its effective radius (fig. 1.10A). Noteworthy, this correlation also holds when including the dissolved hexacyanoferrate complex. These result suggest that the formal potentials vary with different polarisation strengths at the nitrogen end of the cyanide ligand caused by different P species. From a ligand chemistry perspective, increased polarisation on the N end enhances the delocalisation of the R site's d electrons onto the cyanide ligand through π backbonding. This in turn lowers the energy of the R site's t_{2g} electrons, therefore stabilises the reduced state and in effect increases the oxidation potential.[185] The extent of π backbonding also influences the lattice parameter, which leads to a linear correlation between reduction potential and lattice parameter for a given R species (fig. 1.10B). Depending on the choice of transition metals, the formal potentials of the tested compositions are up to about 2 V apart.

Besides the transition metal species in the framework, also the inserting ions affect the reduction potentials of PBAs. It has been shown that the reduction potentials for a number of PBA compositions increase in the order $Li^+ < Na^+ < K^+ < Rb^+ < Cs^+$.[17, 186, 187] Changes in reduction potential have also been found for multivalent inserting ions.[54, 188] As the redox potential is determined by the

overall Gibbs free energy of the insertion reaction, two contributions to this effect have been identified. Firstly, the free energy of solvation varies between the inserting species.[185] This quantity is dependent on the ions' charge density and its absolute value decreases from Li^+ to Cs^+. In experiments, a linear correlation between hydration energy and redox potential has been found.[187] This contribution has been identified as the main contribution to the varying redox potentials.[4, 185, 187] A second contribution is posed by differences in ion-host lattice interactions among the different inserting ions. This effect has been theoretically investigated by materials modelling and has been found to result in the same trend in reduction potentials.[189] For the performance in batteries, the higher potentials from using larger inserting ions potentially result in higher cell voltages, which could increase energy density. On the other hand, larger ions have been reported to exhibit slower mass transport within the PBA lattice, which could limit rate capabilities.[190, 191]

Due to this large spread in electrochemical potentials and their unique features, PBAs have been investigated both as cathode and anode materials in rechargeable metal ion batteries. In the following, the most notable results from these two strands of research are analysed.

The highest redox potentials in PBAs are found for hexacyanoferrates, which make them candidates for cathode materials. A wide range of materials with P=V, Cr, Mn, Fe, Co, Ni, Cu, In and others have been tested in aqueous and non-aqueous electrolytes and with a variety of inserting ions. The specific capacity of these materials varies vastly, which is mostly due to different numbers of redox processes obtainable per formula unit, as well as the amount of hexacyanometallate vacancies in the structure. The effect of these two parameters on the number of stored electrons is apparent when taking a look at the reactions. The following examples describe the theoretical redox reactions of a highly vacant copper hexacyanoferrate, vacancy-free copper hexacyanoferrate and a vacancy-free manganese hexacyanoferrate in a potassium-ion electrolyte:

$$Cu^{II}[Fe^{III}(CN)_6]_{2/3} + \frac{2}{3}\,e^- + \frac{2}{3}\,K^+ \rightleftharpoons K_{2/3}Cu^{II}[Fe^{II}(CN)_6]_{2/3} \tag{1.15}$$

$$KCu^{II}[Fe^{III}(CN)_6] + e^- + K^+ \rightleftharpoons K_2Cu^{II}[Fe^{II}(CN)_6] \tag{1.16}$$

$$Mn^{III}[Fe^{III}(CN)_6] + 2\,e^- + 2\,K^+ \rightleftharpoons K_2Mn^{II}[Fe^{II}(CN)_6] \tag{1.17}$$

Comparing the reactions 1.15 and 1.16, it becomes clear that vacancies are detrimental for an electrode material's capacity. Vacancies reduce the amount of available redox-active R site transition metals and acts as a positive point defect, thus lowering the ability to store cations in the structure.[192, 193] Therefore, vacancies must be avoided in order to achieve high specific capacities.

When both P and R are redox-active, the capacity can be further increased, as can be seen when comparing the reactions 1.16 and 1.17. Two redox reactions are found in vanadium,[194] manganese,[54, 57, 58, 195–197] cobalt[198–200] and iron hexacyanoferrate,[68, 201–204] while other hexacyanoferrate-based materials do not show P-site redox.[29, 192, 193, 205–207] The theoretical specific capacity of vacancy-free PBAs with two redox centres is about $170\,mA\,h\,g^{-1}$, as high as lithium iron phosphate, which is widely employed in modern commercial Li-ion batteries.[208, 209]

For the reasons explained above, work in recent years has been targeted to the synthesis of PBA cathode materials with suppressed vacancies in order to increase capacities.[52, 210, 211] Synthetic adjustments such as an increase in counterions during coprecipitation has lead to a decrease in vacancy contents,[42, 54–57, 212], while the synthesis from chelated precursors and single-metal-source syntheses yield virtually vacancy-free PBAs.[29, 40, 58, 61, 69, 200, 201, 213] Specifically, $A_2Fe[Fe(CN)]_6$ and $A_2Mn[Fe(CN)_6]$ have been in the centre of attention because of their two redox centres, high redox potentials, controllable synthesis and elemental abundance for the use in Na- and K-ion batteries. Through the elimination of vacancies, state-of-the-art PBA cathodes of these compositions are able to reach the theoretical capacity.[61, 69] The vacancy-reduction has another advantageous effect: fewer coordinated water molecules are present, which makes the materials easier to dehydrate. This in turn leads to fewer parasitic reactions and better performance in high-voltage cells with non-aqueous electrolytes.[214, 215]

The high rate capability and long cycle life found for PBA cathode materials in aqueous electrolytes lead to the desire to pair them with PBA anode materials and achieve high-power, long-life cells.[18] Materials based on hexacyanomanganates and hexacyanochromates exhibit redox potentials at the lower end of the stability window of aqueous electrolytes and are therefore candidates as anode materials in these systems.[185, 216, 217] Pasta *et al.* employed manganese hexacyanomanganate in an aqueous Na^+ electrolyte. The results confirmed the two low-potential redox processes measured by Scholz and Dostal[185] near $-0.7\,V$ ($Mn^{II}-N{\equiv}C-Mn^{II/I}$) and $0\,V$ ($Mn^{II}-N{\equiv}C-Mn^{III/II}$), as well as a third, high-potential process at $0.7\,V$ ($Mn^{III/II}-N{\equiv}C-Mn^{III}$), all *vs* SHE. A following work using a low-vacancy $Na_{1.96}Mn[Mn(CN)_6]_{0.99}$ and an organic electrolyte, a total of $209\,mA\,h\,g^{-1}$ of charge could be reversibly stored via the three electrochemical reactions.[57] Because of the large difference in the redox potentials, only the lowest plateau with a capacity of $67\,mA\,h\,g^{-1}$ has been considered for utilisation as anode in a later work.[218] A logical step towards higher energy densities is to study hexacyanochromate-based PBA compositions, for which even lower redox potentials have been found.[142, 185] Wheeler *et al.* reported the performance of manganese hexacyanochromate in a highly concentrated water-in-salt Na^+ electrolyte.[60] The material exhibited the lowest redox potential of any PBA reported to date, at $-0.86\,V$ *vs* SHE (see fig. 1.11A). The material achieved a reversible capacity of $62\,mA\,h\,g^{-1}$, owing to one redox process per formula unit and a high vacancy content of 30%. Nakamoto *et al.* reported a capacity of around $70\,mA\,h\,g^{-1}$ for the same composition.[219] In an attempt to achieve higher capacities, the composition chromium hexacyanochromate was targeted. Two redox reactions are predicted for this material at similarly low potentials, which could give this composition the highest usable capacity yet.[220] In fact, Chen *et al.* reported two redox reactions at $-0.64\,V$ and $-0.75\,V$, delivering a capacity of $108\,mA\,h\,g^{-1}$ (see fig. 1.11B).[221] Despite the material possessing $y = 1/3$ $Cr(CN)_6{}^{3-}$ vacancies, this marks the highest specific capacity among the reported PBA anode materials.

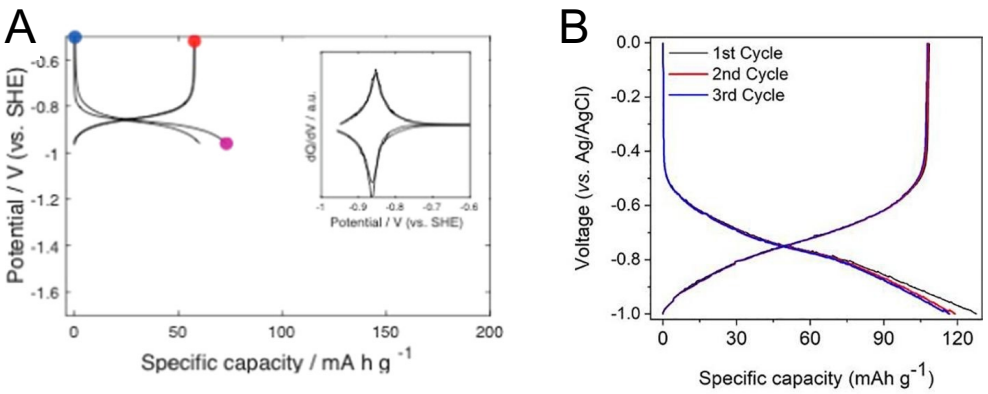


Figure 1.11: Galvanostatic (dis)charge profiles of low-potential hexacyanochromate-based PBA materials. $Mn[Cr]_{2/3}$ cycled in a water-in-salt Na^+ ion electrolyte (A). Reprinted with permission from [60]. Copyright 2019 American Chemical Society. $Cr[Cr]_{2/3}$ cycled in a water-in-salt Na^+ ion electrolyte (B). Reprinted with permission from [221]. Copyright 2021 Elsevier B.V.

The lowest potentials found in PBA materials are still $> 1.7\,V$ above Na^+/Na. This leads to significantly lower cell voltages compared to carbon-based anode materials, rendering PBA anodes impractical for high-energy density cells. High-rate aqueous cells remain the possible application for low-potential PBA composition.

Higher capacities at even lower potentials have been reported for different hexacyanoferrates[222, 223] and hexacyanocobaltates[224]. However, a comprehensive study by Shibata *et al.* showed that PBAs lose their crystal structure at the potentials used in these studies.[225] They conclude that the capacity stems from a conversion reaction of the formed metal oxide decomposition products instead of the PBA itself.

1.4 Thesis objectives

From the theories and past work reported above, clear pathways towards PBAs with improved magnetic and electrochemical properties can be derived. Experimentally, these have been impeded in large parts by synthetic challenges for many of the identified promising compositions. This thesis aims at pushing the boundaries of accessible PBA compositions by optimising a synthesis methodology recently developed in this group. The targeted materials are chosen for their predicted high magnetic ordering temperature and promising electrochemical properties to be

studied as molecular magnets and possible anode materials for future aqueous K- and Na-ion batteries. In more detail, the objectives set for this work are the following:

Chapter 3: Optimised synthesis and characterisation of chromium hexacyanochromate

- Optimise a non-aqueous synthesis route with regard to an increase in particle size and control over the material's oxidation state
- Characterise the composition and structure of the resulting materials using quantitative physicochemical methods
- Unravel the conflicting reports concerning this composition's oxidation states

Chapter 4: Magnetic and electrochemical properties of chromium hexacyanochromate

- Determine the synthesised material's spin arrangement and magnetic ordering temperature
- Investigate and qualify the low-potential redox behaviour and capacity of the composition in non-aqueous K^+ and Na^+ electrolytes
- Evaluate the material's long-term cycling stability

Chapter 5: Non-aqueous synthesis of transition metal hexacyanoferrates

- Explore the universality of the non-aqueous synthesis strategy
- Analyse vacancy-suppressing solvent effect in hexacyanoferrate-based PBAs
- Find the boundaries of vacancy suppression and study its fundamental mechanism

2 Methods

Contents

2.1 Physicochemical characterisation 38
2.1.1 Powder X-ray and neutron diffraction 38
2.1.2 Fourier-transform infrared spectroscopy 42
2.1.3 Simultaneous thermal analysis 43
2.1.4 Inductively coupled plasma elemental analysis 45
2.1.5 Scanning electron microscopy 48
2.2 Magnetic characterisation 49
2.2.1 Superconducting quantum interference device magnetometer 49
2.2.2 Temperature-dependent magnetisation 51
2.2.3 Field-dependent magnetisation 53
2.3 Electrochemical characterisation 54
2.3.1 Electrode preparation 54
2.3.2 Two- and three-electrode cells 56
2.3.3 Voltammetry 59
2.3.4 Galvanostatic cycling 60
2.4 Other methods 61
2.5 Chemicals 62

This chapter aims to introduce the physicochemical, magnetic and electrochemical characterisation techniques used in this thesis. The working principle for each of the techniques is outlined before the experimental setup and specimen preparation used in this thesis are presented. The measurements can be grouped into three sections, physicochemical, magnetic and electrochemical, and will be

explained below.

2.1 Physicochemical characterisation

2.1.1 Powder X-ray and neutron diffraction

2.1.1.1 Working principle

Diffraction techniques are standard techniques for the study of the internal structure of materials. They are based on the scattering of incident waves off atoms in a sample and the interference of the scattered beam. Photons are often used as diffracting species. Because of the particle-wave duality, also particles like neutrons and electrons can be used as probe, with their wavelength determined by their de Broglie wavelength,

$$\lambda = \frac{h}{p}, \tag{2.1}$$

where λ is the wavelength of the particle, h is Planck's constant and p is the particle's momentum.[226] In order for diffraction to occur, the wavelength of the incident photons must be in the same order of magnitude as the distance between scattering centres.[227] Typical repeat distances in crystalline materials are in the order of 1 Å. This requires photons in the X-ray energy range, which possess suitable wavelengths to meet this criterion. In the case of neutrons, which are supplied by spallation processes or nuclear reactors, the hot neutrons from the source are cooled by passing through a moderator in order to achieve usable wavelength ranges.

In diffraction experiments, the incident beam is guided onto the specimen. The photons or neutrons scatter off atoms in the specimen and, due to their wave nature, interfere upon exiting the material. If the material exhibits crystalline order, different lattice planes with Miller indices (hkl) and interplanar distances d_{hkl} are present. As shown in fig. 2.1, the waves exiting the materials at an exit angle θ' equalling twice the incident angle θ interfere constructively if they obey the relation known as Bragg's law[228]

$$n\lambda = 2d\sin(\theta), \tag{2.2}$$

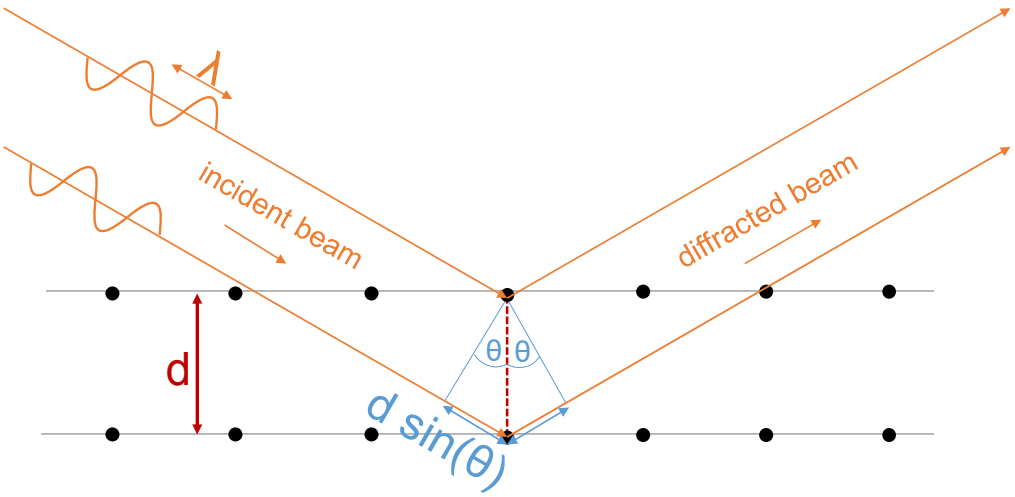


Figure 2.1: Principle of diffraction experiments. The incident beam interacts with atoms in the specimen and is scattered. The phase relationship between different parts of the beam scattered off parallel lattice planes determines the interference behaviour and thus the diffracted signal.

where n is the order of the peak. At the angles θ where Bragg's law is met, the material's diffraction pattern exhibits peaks. At other θ, the intensity vanishes due to destructive interference. From this equation we can distinguish two experimental approaches: varying θ and measuring at a fixed λ, or measuring over a range of λ and measuring at fixed θ.

X-ray powder diffraction (PXRD) is most commonly used as a fixed-λ technique requiring monochromatic X-rays. In lab-scale instruments, these are produced via a X-ray tube. To achieve high intensities and a narrow range of frequencies, typically characteristic atomic emission lines are used. The incident and exit angles are coupled to obey $\theta' = 2\theta$ and are variable. This way, different d-spacings are probed successively.

In neutron powder diffraction (PND), the same monochromatic approach can be taken. In this case, a monochromator lets only neutrons within a narrow wavelength range pass and, analogous to XRD, different incident angles are scanned. Due to the typically broad neutron energy spectrum, this means that only a small fraction of the available intensity is used for the experiment. Polychromatic experiments are an alternative with higher beam utilisation. This method requires a way to distinguish neutrons with different wavelengths. Since, opposed to X-rays, neutrons

of different wavelengths possess a different velocity (see eqn. 2.1), they arrive at the detector at different times. Because of the sufficiently low velocities of thermal and cold neutrons, electronic detector readouts can resolve these differences in the neutrons' time of flight (TOF) and a diffractogram can be constructed. Depending on the used wavelength range, a limited d-range can be measured at a fixed θ. For this reason, TOF beamlines are often equipped with a range of detector banks at different θ to offer maximum flexibility.

In powder diffraction, the assembly of particles in a specimen is considered to consist of a large number of randomly oriented particles. Whenever Bragg's law is met, a substantial number of particles will be in the right orientation to diffract the incident beam, so that each diffraction peak is observed. Due to the random orientation of particles, the diffracted signal is rotation-symmetric and maxima form the so-called Debye-Scherrer rings. Therefore, a one-dimensional scan is sufficient to obtain all scattering information contained in a specified range of incident angles θ.

The resulting diffraction pattern contains a wealth of information in its different aspects. The set of positions of observed diffraction peaks contains information about the crystal symmetry and unit cell geometry. The relative peak intensities contain information about phase fractions, the elemental species of atoms, their occupancy and position in the unit cell, isotropic and anisotropic displacements caused by thermal vibrations, and others. From the peak widths, information about microstrain and particle size can be extracted.[227] In the case of amorphous samples, the diffractogram does not contain sharp diffraction peaks. Using neutron diffraction, additionally to the atomic structure, also magnetic ordering within materials can be probed. Since neutrons possess a non-zero spin, they interact with uncoupled electronic spins in a material.[229] In unpolarised PND, the contribution of magnetic scattering is additive to the atomic diffraction. Magnetic order in materials can therefore be detected from the presence of additional magnetic Bragg peaks and/or differences in relative peak heights.

In order to access this information, the observed diffraction patterns can be fitted to a comprehensive structural model. The method of Rietveld refinement

combines the fitting of structural and magnetic parameters and influences from the instrument and experimental setup.[230, 231] During refinement, the peak positions, intensities and broadening are calculated based on an initial model structure. To obtain an initial model, a structure search can be carried out. For a large number of known compounds, including many PBAs, databases are available from which crystallographic information can be accessed. The parameters of the model are then iteratively changed to minimise the least-squares deviations from the experimental data. The value of R_{wp} is defined as the root-mean-square difference between the computed and measured diffractogram and acts as an indicator for the conformity between sample and model. However, it has been pointed out that a graphical inspection of the fit is crucial to ensure meaningful results.[232] Once a good agreement is reached, quantitative information can be extracted from the refined model.

2.1.1.2 Experimental setup

In this work, laboratory X-ray diffractometers with Cu K_α radiation are used. Air-sensitive samples are measured using a Rigaku Miniflex benchtop diffractometer located in a nitrogen-filled glovebox. For air-stable compounds, a Rigaku Smartlab 3kW diffractometer is used. All samples are measured in reflection geometry, located on flat, low-background or aluminium sample holders. High-vacuum grease is used to fixate the specimen onto the sample holder in the case of measurements using the benchtop instrument due to its rotating sample stage. Rietveld refinements are carried out using GSAS-II software.[233]

PND experiments in this work are carried out on the WISH beamline at the ISIS Neutron and Muon Source at the STFC Rutherford Appleton Laboratory in Oxfordshire, UK. The beamline is a TOF neutron diffractometer offering high resolution and a wide d-range.[234] The sample is placed in a vanadium can and mounted in a cryostat. Diffractograms are taken at variable temperatures from 10 K to 309 K. Multipattern Rietveld refinements are carried out using FullProf software.[235]

2.1.2 Fourier-transform infrared spectroscopy

2.1.2.1 Working principle

Fourier-transform infrared spectroscopy is a type of vibrational spectroscopy utilising the interaction of photons with molecule or lattice vibrations.

Light represents an oscillating electromagnetic field which is able to interact with electric dipoles and excite vibrations thereof. When the frequency of incoming light matches the resonant frequency of an electric dipole, photons are absorbed and the vibration is amplified.[236] A general non-linear molecule made up from N atoms can possess $3N - 6$ vibrational modes, so-called normal modes, which can be classified by their respective displacement as stretching, deformation, scissoring, wagging, rocking, torsion and others.[237] Common functional groups and molecules possess natural vibrational frequencies that coincide with the frequency of light in the infrared (IR) wavelength region. Infrared radiation can therefore be used to probe the excitement of vibrations in materials. The found absorption lines can be used to identify the presence of molecular species and functional groups. Vibrational frequencies are sensitive to the bond-strength between the atoms participating in the activated vibration mode. This makes IR spectroscopy highly relevant for the study of oxidation states in PBAs.[24, 25]

The main parts of the FTIR instrumentation consist of a polychromatic IR light source, an interferometer, guiding optics, the sample stage and a detector. The recorded data is then processed via Fourier transformation using software to get the final spectrum. FTIR spectroscopy is the preferred way of measuring IR spectroscopy because of several advantages over dispersive measurements. Firstly, the accuracy of the measured frequencies is high because of the calibration with a stable and accurately known laser reference. Secondly, the sample is probed by an interferogram of all wavelengths at the same time, which shortens acquisition times. Thirdly, the optics do not require the use of high-loss components such as slits, which increases optical resolution.[238]

The most often used sampling methods in IR spectroscopy are transmission and reflection. In transmission mode, a sample is introduced into the IR beam and

the transmitted intensity is recorded. For powder samples, this method usually needs prior specimen preparation in terms of embedding the studied material in an IR-transparent matrix. A widely-used alternative to the transmission mode are attenuated total reflection (ATR) measurements. In this method, the IR light is guided through a material with high refractive index under an angle small enough to obtain total reflection at its surface. When a sample is pressed onto this surface, the reflected IR beam probes the sample as a so-called evanescent wave, reaching into the studied material with a penetration depth of a few µm.[238, 239] At frequencies matching the normal modes in the sample, the reflected beam is attenuated. This sampling method is particularly convenient since it does not require prior specimen preparation.

2.1.2.2 Experimental setup

In this work, a Thermo-Fischer Nicolet iS50 situated in a nitrogen-filled glovebox, and a Perkin-Elmer Spectrum Two are used. Both ATR and transmission modes are employed. On both instruments, ATR measurements are carried out using a diamond internal reflection element. For transmission-mode measurements, the powder samples are mixed with vacuum-dried KBr or CsI in an agate mortar and pestle and pressed into a transparent pellet using a hand press.

Fig. 2.2 shows the IR source signal (A) and the background signal through the diamond ATR stage (B) used in this work. Because of the absorbtion of the IR signal by the diamond ATR material in the wavelength region around $200\,\mathrm{cm}^{-1}$ which is highly relevant to this work, the dwell time is increased to obtain a high signal-to-noise ratio.

2.1.3 Simultaneous thermal analysis

2.1.3.1 Working principle

Simultaneous thermal analysis is a combination of the techniques thermogravimetric analysis (TGA), differential scanning calorimetry (DSC) and mass spectrometry (MS). It is used to study the temperature-dependent behaviour of specimen. The

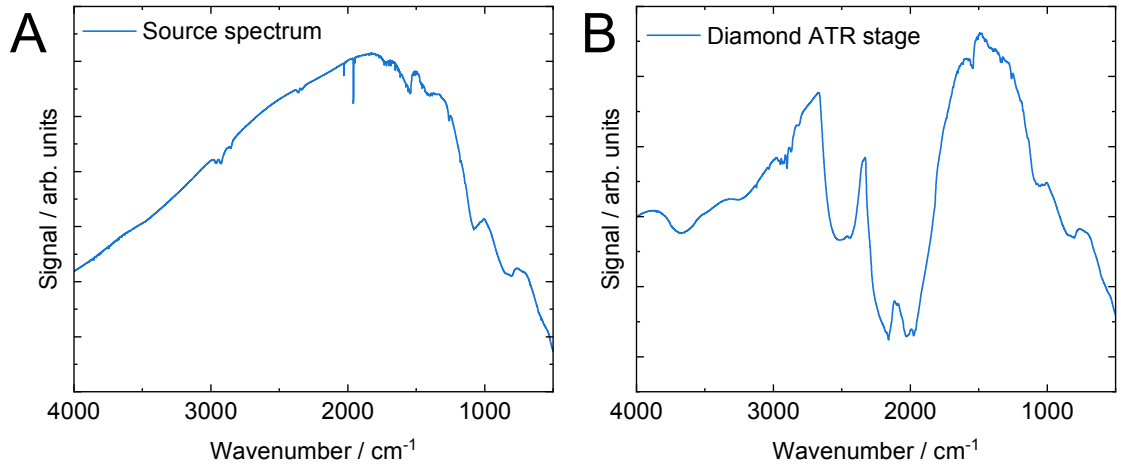


Figure 2.2: FTIR signal of the source (A) and measured with use of a diamond ATR accessory (B).

simultaneous acquisition of these three different techniques gives a more complete picture of basic thermally induced changes in a specimen's state.

For these measurements, a small amount of sample is filled into a high-temperature stable crucible and placed on a sample carrier in the instrument's furnace. Different gases can be introduced into the furnace in order to protect the sample from chemical reactions (inert) or to simulate reactive environments. The sample is then cooled, heated or held at a temperature according to a specified temperature profile. In order to avoid thermal hysteresis,[240] low sample heating and cooling rates are often preferred. During this dynamic change in temperature, various parameters of the sample are measured.

TGA is the measurement of the temperature-dependent differences in specimen mass. As such, it is capable of determining the mass change during decomposition, ad- and desorption, evaporation or drying processes. DSC is the measurement of heat flow between the specimen and an inert reference sample. This techniques is used to determine the energetics of phase changes, decomposition and other processes. This method is capable of detecting processes happening without exchange of mass, and is therefore able to uncover *e.g.* crystallographic phase changes that aren't visible in TGA traces. DSC provides additional quantitative information on heat capacities, enthalpies of processes and whether these are exothermic or endothermic.[241]

Common examples of exo- and endothermic processes are oxidation reactions and evaporation, respectively. Further information can be gained when the evolved gaseous products are measured during the thermal analysis. This can be done by using a mass spectrometer, a sensitive instrument for the determination of chemical species, coupled to the furnace. As such, this technique complements TGA traces by supplying chemical information which help assign processes and interpret data.

2.1.3.2 Experimental setup

Thermal analysis is carried out using a Netzsch STA449 F3 Jupiter coupled with a Netzsch Aeolos QMS 403 D mass spectrometer. The capillary connecting the MS to the furnace is kept at 300 °C. Alumina crucibles are used as both sample container and reference for DSC, where for the latter the crucible is empty. The typical sample size is a few mg of material. The setup does not allow for inert transfer into the machine. To avoid effects arising from interaction with air and moisture as much as possible, the crucibles are dried at 70 °C in a vacuum oven overnight prior to measurements and the furnace is evacuated twice and refilled with argon. All measurements are carried out in inert argon atmosphere. Heating rates of $1\,\mathrm{K\,min^{-1}}$ to $10\,\mathrm{K\,min^{-1}}$ are used.

2.1.4 Inductively coupled plasma elemental analysis

2.1.4.1 Working principle

Inductively coupled plasma combined with mass spectrometry (ICP-MS) or optical emission spectroscopy (ICP-OES) are sensitive techniques to analyse the chemical compositions of specimen. These techniques usually require samples in form of solutions, however, solid samples can be measured using various ablation techniques. In this description, the liquid sample analysis employed in this work is introduced.

The technique is based on a succession of three consecutive steps: sample introduction, ionisation and quantification. As a first step, the solution to be analysed is transferred to the instrument via a peristaltic pump and transported to a nebuliser. Using a fine nozzle and pressurised inert gas, the solution is dispersed

into a fine mist there. A small fraction of this mist is forced into the torch assembly of the instrument. In the torch, the sample mist is guided into an induction coil, at which a high-frequency AC voltage is applied. Here, the carrier gas and the sample are ionised via collision processes mainly with fast electrons at temperatures up to 10 000 K.[242] Following this step is the quantification of analytes in the plasma. While the operating principle has been very similar between ICP-MS and ICP-OES up to the sample ionisation, this is where the techniques differ. In ICP-MS instruments, the ionised sample is guided via ion optics into a mass spectrometer, where it is analysed.[243] ICP-OES instruments, on the other hand, measure the optical emission lines arising from the excitement of ions in the plasma via collision with electrons.[244] The light is guided through axial or radial windows and analysed by an optical spectrometer.[245] The advantages and disadvantages of both techniques are discussed in detail by Olesik.[246] From a practical point of view, ICP-MS is capable or measuring lower analyte concentrations, while ICP-OES is less capital-intensive.[247]

If solid samples are to be analysed with the commonly found ICP instruments with liquid sample introduction, the solids need to be brought in solution prior to measurements. A complete dissolution during this step is crucial for reliable measurements. Since solids cannot be measured, an only partly dissolved specimen or precipitates formed during digestion result in erroneous results. For many sample types, this digestion can be problematic and might require harsh conditions. Method notes are available from manufacturers of digestion equipment describing suitable conditions to dissolve a number of materials. This digestion is usually done in concentrated acids and/or oxidative environments. Elevated temperatures can help digesting difficult samples. This can be done simply on a hotplate or using microwave digestors using high-pressure vessels designed to heat acid mixtures above their boiling point.

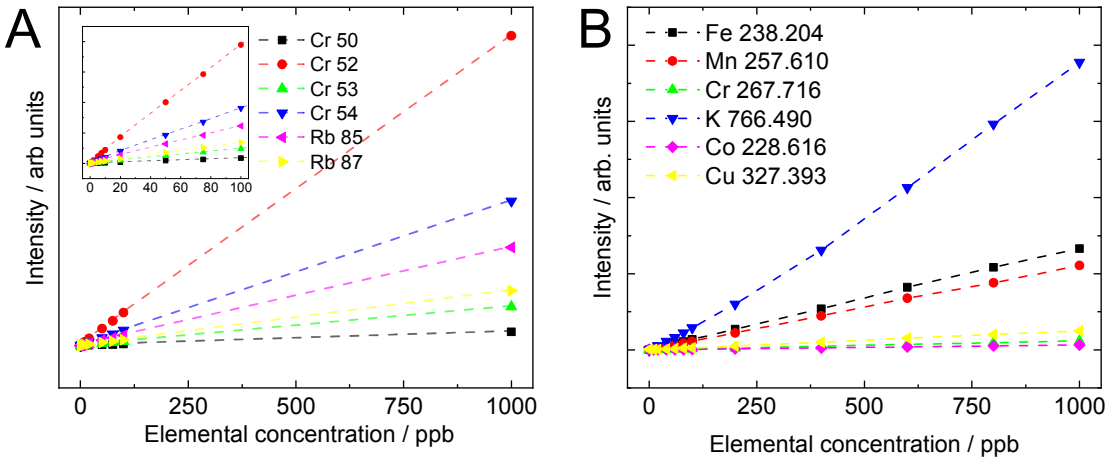


Figure 2.3: ICP-MS (A) and ICP-OES (B) calibration lines for analytes studied in this work. A correlation of > 0.999 is found for every analyte.

2.1.4.2 Experimental setup

In this work, two ICP instruments are used. A Shimadzu ICPMS-2030 ICP-MS instrument is used to analyse chromium hexacyanochromate samples in chapter 3. This instrument is capable of accurately determining the Rb content in the samples, which is problematic using an ICP-OES instrument because of emission line interference between Rb and the used Ar carrier gas.[248] For the digestions of these samples, an Anton Paar Multiwave GO Plus microwave digestor equipped with PTFE vessels is used. A Perkin-Elmer Optima 8000 ICP-OES instrument is used for all other samples in this work.

Although PBAs are known to be unstable in concentrated acids below pH $\lesssim 1$, all samples in this work needed to be heated in concentrated mineral acids to achieve full digestion. The detailed digestion condition varies between samples and are explained in later chapters. Samples are diluted into a matrix of 2% HNO_3 solution in ultrapure water (resistivity 18.2 $M\Omega\,cm$). Different precise dilutions of the multielement standard solution 5 from Sigma-Aldrich are prepared using volumetric flasks and used as standard solutions. Fig. 2.3 shows the calibration lines of ICP-MS (A) and ICP-OES (B) instruments for analytes of interest for this work. The correlations of the used calibration lines of all analytes are > 0.999.

2.1.5 Scanning electron microscopy

2.1.5.1 Working principle

Scanning electron microscopy (SEM) is an imaging technique capable of determining the morphology of samples in the µm and nm range.

The technique is based on the use of a beam of electrons used as a probe. The electrons are accelerated by a high voltage, usually referred to as ultra high tension (UHT), typically in the kV range. Due to the high electron energy, their wavelength becomes small, $< 1\,\mathrm{nm}$, which makes them a suitable probe to resolve features in the sub-µm size range.[249] The electrons are emitted by an electron gun and focused by electron optics to a small point on the sample. Via deflection coils, the focused electron beam is moved and scanned across the region of interest on the sample. The electron beam interacts with the sample, which leads to several processes that can be used to gain information about the sample. A part of the electron beam is backscattered, typically up to $\approx 50\%$.[250] Another part of the beam's energy is transferred to electrons in the material, which become energetic enough to escape the material as detectable secondary electrons. Another source of free electrons stems from the Auger effect. Back scattered electrons (BSE) and secondary electrons (SE) are the two most common imaging modes used in SEM. While the electron beam is scanning the sample, the emitted electrons are quantified for every pixel, which determines their brightness. The contrast of an image is dependent on the imaging mode. SE imaging possesses a pronounced edge effect and high spatial resolution because of the low exit depths, which makes this mode well-suited to image sample topography.[250] BSE imaging exhibits a large compositional contrast and is therefore suitable to distinguish regions made up from materials with different atomic numbers. The spatial resolution is inferior compared to SE imaging due to the large volume within the sample from where BSE are emitted.[249] Modern SEM instruments are equipped with several detectors sensitive to electrons in specific energy ranges and measure the amount of low-energetic ($< 50\,\mathrm{eV}$)[250] SE and high-energetic BSE.

The achievable resolution is mainly determined by the spot size of the electron beam on the sample, which depends on the width of the emitted electron beam at the gun, the quality of the optics, and the electron wavelength, which is determined by the accelerating voltage.

2.1.5.2 Experimental setup

SEM imaging is carried out on a Zeiss Merlin microscope. Typically, images are taken in high-resolution column mode with an accelerating voltage of 10 kV to 30 kV, a probe current of ≈ 100 pA and a working distance of 3 mm to 10 mm. The images shown in this work are recorded using the in-lens SE and transmission-mode STEM detectors.

2.2 Magnetic characterisation

2.2.1 Superconducting quantum interference device magnetometer

2.2.1.1 Working principle

A superconducting quantum interference device (SQUID) magnetometer is a highly sensitive instrument for the measurement of a sample's magnetic moment. It is based on the effect of electromagnetic induction in a superconducting loop.

In a SQUID measurement, the analysed sample with unknown magnetic moment is moved through a gradiometer, an arrangement of superconducting loops. This causes a change in flux through the loops, which according to Faraday's law results in the formation of a current in the superconducting wire. These are dependent on the area enclosed by the loops, the speed at which the sample is moved through the gradiometer and the magnetic dipole moment of the sample. To reliably analyse the sample, the instrument therefore needs to be precisely calibrated and the sample movement accurately controlled. In order to avoid interference with environmental magnetic fields, the gradiometer encompasses loops of opposite winding directions. This way, only magnetic fields from dipoles close to the pick-up coils are detected, while magnetic fields from far away sources that can be viewed as constant are

excluded.[251] The flux picked up in the gradiometer is then transferred to a read-out assembly coupled via a flux transformer, where the signal is measured. In this type of instruments, a SQUID is used for this purpose.[252]

A SQUID consists of a closed loop of superconducting material which is interrupted by (in modern instruments) two Josephson junctions. These are thin barriers of non-superconducting materials with distinct electronic properties. Below a critical current, Josephson junctions behave like superconductors and possess a vanishing resistance. A the transition region around its critical current, the resistance rapidly increases, or in other words, the voltage across the Josephson juction is very sensitive to changes in current. This phenomenon is used to very accurately determine the current induced via the flux transferred from the pick up coil.[251] An external voltage is applied to the SQUID to keep the flux the loop constant. From the required applied voltage, the flux difference caused by the sample moving through the gradiometer can be determined, and with it the unknown magnetic moment of the sample.

Apart from its accuracy, the advantages of SQUID magnetometry are the largely different sample environments that can be set, with a typical temperature range of 1.8 K to 400 K and magnetic fields of up to typically 7 T,[252] as well as a low required amount of sample ($\approx$ few mg).

2.2.1.2 Experimental setup

The magnetic measurements in this work are taken on a Quantum Design MPMS-XL SQUID magnetometer. The instrument is equipped with a 7 T magnet and can probe sample temperatures of 2 K to 400 K. The samples are placed in a closed plastic capsule prepared in an argon-filled glovebox and inserted into the instrument mounted on a brass sample holder.

All magnetic measurements are carried out by my collaborator Dr Ramón Torres-Cavanillas.

2.2.2 Temperature-dependent magnetisation

One of the most important measurement techniques for molecular magnets is the determination of the DC magnetic properties (χ or M) in dependence on temperature. It is the common means from which the magnetic ordering temperatures are extracted.

These measurements are usually carried out in a small applied field which defines a common z direction and aligns the spins. At the same time, the applied field should be small enough as to not perturb the studied system. Two modes are used to determine the temperature-dependent magnetism of a specimen. In zero-field cooled (ZFC) experiments, the specimen is introduced at room temperature and cooled down to the lowest measured temperature under the absence of an external magnetic field (see fig. 2.4A). Then the defined magnetic field is applied, and the magnetic moment is measured while the sample is heated to the highest measured temperature. In field-cooled (FC) experiments, the specified magnetic field is switched on before the sample is cooled down to the minimal temperature (see fig. 2.4B). Analogous to the ZFC case, the magnetic moment is measured while the sample temperature is increased. The difference in the two experimental approaches effectively lies in the initial state of the spins in the measured specimen. In ZFC, the spins are randomly oriented before measurement, while in FC they enter the measurement pre-aligned by the external magnetic field.

The deviation of the two magnetisation curves determined from ZFC and FC modes contains information about the studied system. The two lines often separate when the ZFC exhibits a maximum. This point identifies the blocking temperature T_B for a spin fluctuation effect found in superparamagnetic samples.[253, 254] Below this temperature, the magnetic anisotropy is dominant and, in the timescale of measurement, the spins appear 'frozen' into the arrangement given during cooling down, *i.e.* random for ZFC and aligned along z for FC.[255] As the temperature increases, more fluctuations occur during the measured time interval and the FZC signal increases. At temperatures where the ZFC and FC curves merge, the timescale

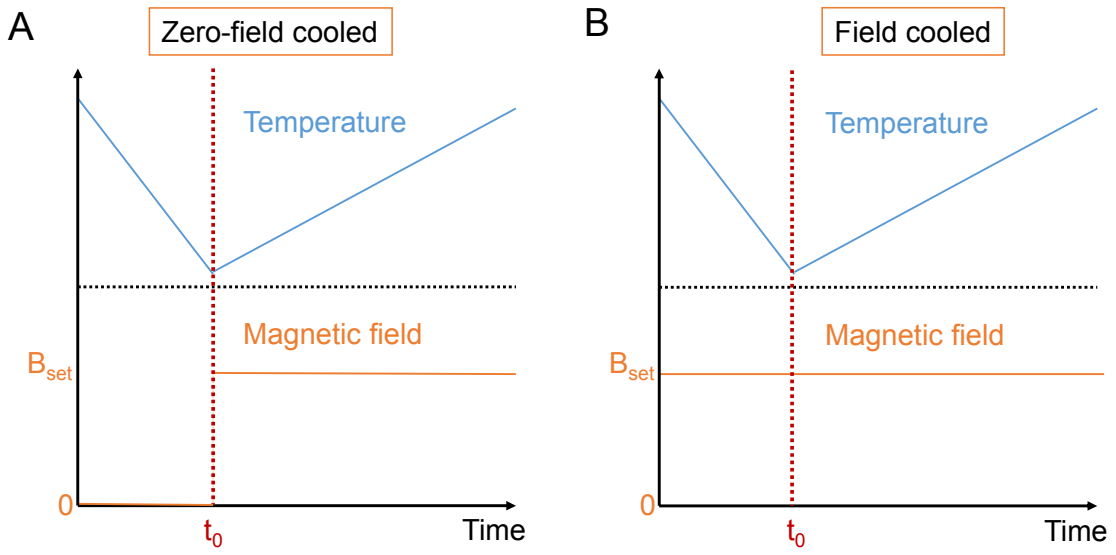


Figure 2.4: Temperature-dependent magnetisation measurements. Temperature and magnetic field profiles for ZFC (A) and FC measurements (B) are shown. t_0 denotes the start of data acquisition, B_{set} is the set applied magnetic field.

for fluctuations is much smaller than the measurement duration and an average of the fluctuating magnetisation is measured.

From the shape of the χ or M *vs* T curve, magnetic ordering phenomena can be identified. The found onset temperatures are commonly interpreted as the ordering temperature of such magnetic phases.

The data can be presented in distinct ways to conveniently extract different information. To fit the data to the Curie-Weiss law (equation 1.7), the data is plotted as χ^{-1}. A simple linear plot in the paramagnetic region is then sufficient to extract both the Curie constant, which contains information about the nature of spin centres, as well as the Weiss constant θ.[256] For ferro- and ferrimagnetic materials, $\theta = T_C$ usually agrees well with the onset temperatures of magnetic phases. In antiferromagnetic materials, $-\theta$ often differs from the found onset temperatures, which is why a graphical readout of T_N in combination with complementary techniques is preferred. Another common way of presenting magnetisation data is as χT *vs* T. This allows the direct distinction of ferro- and ferrimagnetism as well as the extraction of room temperature χT values, which carry information about magnetic interactions between spin centres.

2.2.3 Field-dependent magnetisation

Measurements of the field-dependency of magnetic properties (χ or M) are a widely used characterisation technique for studying magnetism. The observed results complement the insights gained from temperature-dependent measurements.

The measurements are carried out at fixed temperatures, which is why the resulting data is often referred to as isothermal magnetisation. The measurement starts with the specimen in a field-free environment without magnetic dipole alignment. Then, a steadily increasing magnetic field is applied along the z direction. When a set maximum magnetic field is reached, the magnetic field is ramped down until reaching the negative vertex field strength. The applied field is then periodically cycled between the two vertices. The applied temperature and field sequence over time is shown in fig. 2.5A.

Several features of the resulting M *vs* B behaviour contain information about the sample's magnetic properties, as shown in fig. 2.5B. Firstly, the appearance of a hysteresis loop indicates ordering of non-compensated spins, *i.e.* ferro- or ferrimagnetism.[257] M_{rem} of this phase can simply be read off as the intercept of the hysteresis loop with the M-axis. The H_C is equally easily determined as the intercept of the hysteresis loop with the H-axis. M_{sat} is determined from the magnetisation value in the high field limit of the hysteresis loop. Paramagnetic phases or perfect antiferromagnets do not show a magnetic hysteresis. In these cases, the M *vs* T behaviour resembles an approximately diagonal line through $H = 0, M = 0$ and a positive slope, before saturating. The response of diamagnetic materials is a straight line through $H = 0, M = 0$ with a negative slope (not shown in the schematic). Superparamagnets possess a saturating magnetisation curve at high fields similar to ferromagnets, however do not possess magnetic hysteresis. As such, their trace can be regarded as for ferro- or ferrimagnets with zero coercivity and remanence. Often, ordered and non-ordered phases coexist in a sample. Due to the characteristic behaviour, their contributions to the M *vs* T curve can sometimes be deconvoluted.[258]

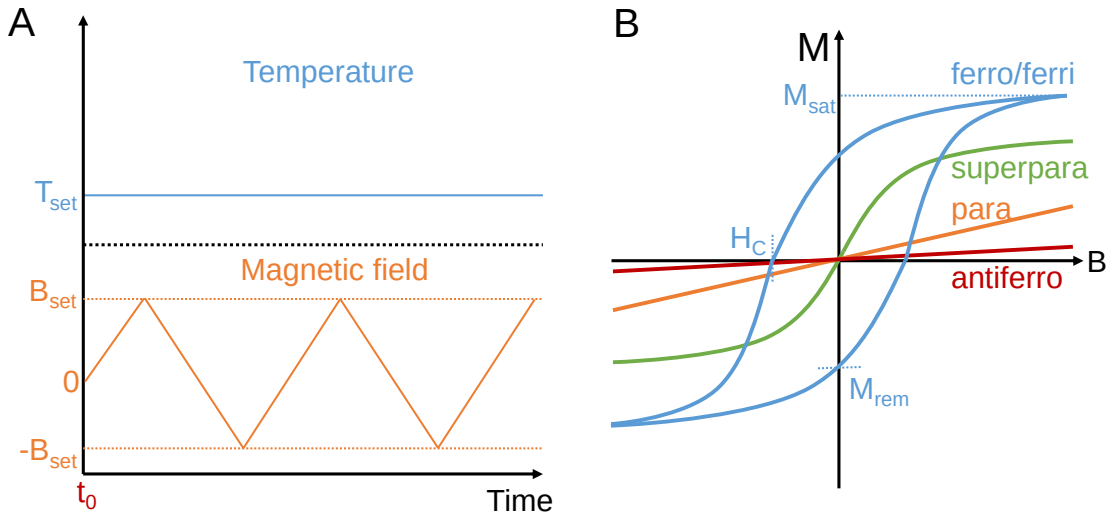


Figure 2.5: Field-dependent magnetisation measurements. Temperature and applied field profiles (A), where T_{set} is the set temperature, $B_s$et is the vortex magnetic field and t_0 indicates the start of data acquisition. Typical hysteresis responses for different magnetic materials (B). From the hysteresis curve, the saturation magnetisation M_{sat}, coercive field H_C and remnant magnetisation M_{rem} of an ordered material can be extracted as shown.

2.3 Electrochemical characterisation

2.3.1 Electrode preparation

2.3.1.1 Main considerations

In order to test the electrochemical properties of compounds, electrodes need to be prepared from them. Depending on the nature of the studied materials, different sample treatments are required. Generally, the main goal stays the same for every electrode: The material needs to be in good ionic contact with the electrolyte, as well as in good electrical contact with the current collector. Ensuring this is the major challenge in electrode preparation.

For the powdered materials dealt with in this work, the electrode needs to realise electrical contact to all particles of the material and mechanical integrity, preventing the electrode constituents from breaking apart. This is usually achieved by mixing the studied active material with additives and casting the composite onto a conductive substrate acting as a current collector.

The two most important additives are a conductive agent, usually nano-sized

carbon materials such as carbon black or nanofibres, and binders, typically polymers. In order to achieve optimal contact and stability, the composite needs to be thoroughly mixed. For the polymer chains to spread out and form a stable network holding the composite together, different strategies can be followed. In wet castings, a solvent is chosen which is capable of dissolving the binder and added to the composite during mixing. The rheology of the formed slurry is controlled via the volume of solvent added. Depending on the system, different binder-solvent combinations are advantageous. This problem is an active, very industrially-relevant field of research.[259] In PBA research, the most widely used chemistry is the combination of polyvinylidene fluoride (PVDF) binder and N-methyl-2-pyrrolidone (NMP) solvent. Another means to achieve a stable binder network is through shear forces during the mixing of a dry composite. This builds the basis of the so-called dry casting process, which will not be discussed further here.

2.3.1.2 Experimental procedure

In this work, electrodes are prepared through a wet casting procedure. Fig. 2.6A shows a schematic of the casting process. The studied material is combined with a conductive agent (Timcal Super P carbon black) and a binder (MTI PVDF binder) in the desired ratio, first by mixing the dry ingredients in an agate mortar and pestle, before forming a wet slurry by dropwise addition of NMP. The viscosity of the slurry is adjusted to be similar to ink via addition of further NMP.

The slurry is then cast onto a current collector. Because of the small mean particle size of the synthesised materials in this work, the slurry is coated onto carbon paper (AvCarb P50). Instead of forming a layer onto a conventionally used flat metal foil current collector, the slurry is soaks into the porous carbon paper, which allows to make use of the fibrous structure of the carbon paper to act as electron conducting channels.

Compared to metal foils, carbon paper possesses a higher surface area. This could potentially cause a large capacity contribution from its double layer, which would distort the measured properties of the studied active material. Additionally, K^+ is

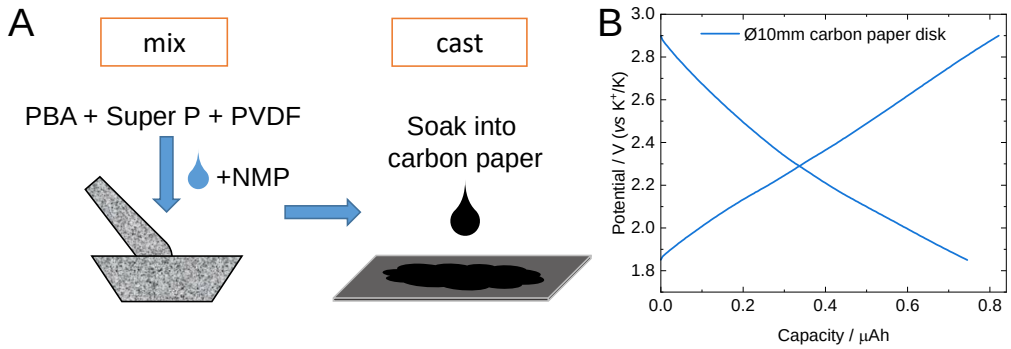


Figure 2.6: Schematic of the mixing and casting steps used to prepare electrodes (A). Determination of the electrochemical capacity of an uncoated, 10 mm-diameter carbon paper disk, as used as current collector in electrochemical tests (B). The carbon paper disk shows a purely capacitive behaviour with a total capacity of $< 1\,\mu A\,h$.

able to undergo intercalation into graphitic carbon, which could add an additional capacity contribution. To quantify the contributions from the two processes, an uncoated carbon paper disk is cycled in the same conditions as used later in this work. The results are shown in fig. 2.6B. The curve is purely capacitive and shows no sign of redox activity in the probed potential range. The empty current collector adds a contribution of $< 1\,\mu A\,h$ to the measured capacity. Taking into account the typical mass loadings and specific capacities of materials used in this work, the current collector contributes to $\ll 1\%$ of the measured values and is therefore neglected.

The electrodes are dried at 80 °C in a vacuum oven (Büchi, Switzerland) overnight, brought into an argon-filled glovebox without exposure to air and stored there before use. Electrode masses are determined using a microbalance (Sartorius Cubis, precision 10^{-4} mg).

2.3.2 Two- and three-electrode cells

2.3.2.1 Working principle

Electrochemical experiments are most commonly carried out in two- or three-electrode cells. In the following, the principles of both are pointed out.

In two-electrode cells, the studied material is placed at the working electrode (WE), while the counter electrode (CE) in the common electrolyte closes the electrochemical circuit. The voltage between the two electrodes is measured and precisely

controlled using a potentiostat, depending on the set experiment, some of which will be explained in the next sections. Therefore, the potential of electrochemical half-reactions at the WE is determined in relation to an electrochemical reaction at the CE. Because the CE acts both as reference point and reaction partner, the measured voltage contains contributions from the CE reaction. A reaction with stable, flat potential profile is therefore used as a counter-reaction to study the properties of the WE with minimum effects stemming from the CE. In order to disturb the reacting species at the CE as little as possible, a large excess in counter-reaction capacity is used. Small overpotentials at the CE must be ensured, which is often achieved by use of fast counter-reactions, high CE surface areas and small distance between the electrodes.

Three-electrode cells eliminate the influence of the CE potential entirely. This is achieved by a cell design and wiring which splits the reference point and reaction partner functions of the CE into two individual electrodes. The reference electrode (RE) forms the reference point against which the WE potential is measured. No discernible current is flowing through this electrode, only the negligibly small currents needed for the determination of the potential difference. The current which closes the electrochemical circuit is delivered by the CE of the three-electrode cell. Through the separation of reaction and reference potential, errors caused by CE or RE overpotentials can be avoided. Thus, WE processes are isolated and can be precisely studied.

Two-electrode cells offer practical advantages such as a simpler and faster assembly. They can offer good accuracy when a suitable stable CE is available. For the precise determination of electrochemical potentials, or in cases where no suitable CE is available or practical, three electrode cells are used. In cases where a suitable RE is lacking, pseudo-reference electrodes offer an alternative. This type of RE is characterised by a lack of Nernstian redox couple, but often still presents a suitably stable, but unknown reference potential. The potential of the pseudo-RE is determined via calibration with a known redox-system often after measurement.[260]

2.3.2.2 Experimental setup

In this work, both two- and three-electrode cell setups are used.

The synthesised materials are characterised in two-electron configuration. Stainless steel CR2032 coin cells are used for this purpose (cell components shown in fig. 2.7A), housing the cast WE, a glass fibre separator (Whatman GF/F) soaked with 100 µL to 150 µL electrolyte and the counter electrode. As CE, Na and K metal is used. Sodium metal (Sigma-Aldrich, 99.9%, stored in mineral oil) is removed from the mineral oil and used as purchased, cut into thin strips, rolled, punched to size, pressed onto a stainless steel spacer disk and brushed to remove any passivating surface layer. Potassium metal (Sigma-Aldrich, 98%) was cleaned by Shobhan Dhir as described in a recent publication[168] and stored in dry hexane. The cleaned K metal is removed from the hexane and pressed onto a stainless steel spacer disk. Sodium metal has been used extensively as a CE in Na-ion batteries, however its reliability is largely dependent on the choice of electrolyte.[261, 262] For the chosen Na-ion test system, Na has been reported to show sufficient stability and is therefore a suitable CE and used in this work.[263, 264] In the case of K metal, it has been demonstrated that a freshly prepared surface can act as a reliable CE for half-cell tests.[265] For the chosen K-ion test system, potassium metal exhibits sufficient stability[168, 266] and is therefore used as CE in this work.

To study the electrochemical stability of the organic solvent used in the non-aqueous synthesis (chapter 3), a three-electrode cell is used. The cell setup is shown in fig. 2.7B. It is comprised of a platinum wire used as CE, a AgCl-coated silver wire (SSC) used as pseudo-RE and a platinum wire WE, immersed in an electrolyte-flooded glass vial. The electrodes are fixated by being pierced through a rubber bung, which at the same time seals the flooded cell at the top. The pseudo-RE was fabricated by electrochemically oxidising a scratched silver wire in an aqueous KCl electrolyte until a visible AgCl layer formed on the wire. The reaction used at the CE is the decomposition of electrolyte at the Pt wire. Since this process possibly introduces decomposition products into the system, these cells are not suitable for long-term cycling tests. However, this setup is acceptable for the

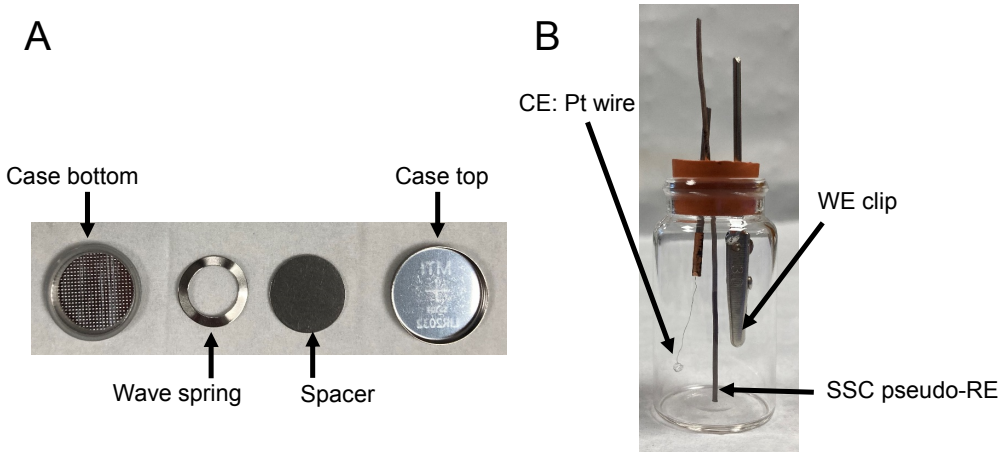


Figure 2.7: Electrochemical cell designs used in this work. Standard stainless steel coin cells components (A) are used as two-electrode cells. A three-electrode cell is made from a glass vial and closed with a rubber bung, through which the three electrodes are contacted (B). The WE is attached to a crocodile clip, the CE is a curled Pt wire and a AgCl-coated silver wire is used as a pseudo-RE.

determination of stability windows using LSV, since the onset of significant current denotes the boundary of stability and thus the end of the experiment in any case.

Coin cells are tested using a Bio-Logic BCS-805 battery cycler. Three-electrode cells are used in conjunction with a Bio-Logic VMP-3 potentiostat and are tested in an argon-filled glovebox.

2.3.3 Voltammetry

Voltammetry is one of the main ways of studying electrochemical systems. It is routinely used to study onset and formal potentials of electrochemical oxidation and reduction reactions.[267] In voltammetric methods, a specified potential profile is applied to the working electrode in relation to a CE or RE, depending on cell design, and the system's current response is measured. Depending on the applied potential sequence, different voltammetric techniques are distinguished. Two widely used methods are cyclic (CV) and linear sweep voltammetry (LSV). Fig. 2.8 shows the measurement protocol for these two techniques. CV is commonly used to study reversible processes. The voltage is cycled with a set rate between two vertex potentials, which are usually chosen to lie below and above a studied redox reaction, respectively. The resulting current *vs* potential curve provides a

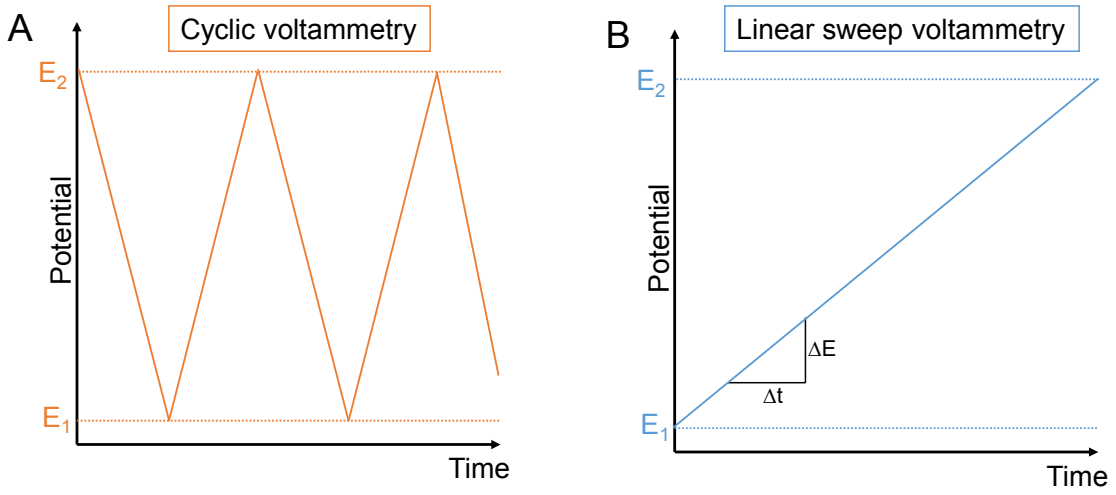


Figure 2.8: Voltammetric measurement protocols. Potential *vs* time profiles used in CV (A) and LSV (B). E_1 and E_2 are the set vertex potentials, the sweep rate is indicated in the LSV potential profile.

simple means to assess the electrochemistry of new systems. Using a quantitative analysis, the reversibility, kinetics and formal potential of redox reactions can be analysed.[268] LSV is a common way to study irreversible processes, for example gas evolution in electrocatalysis or electrolyte decomposition. Using this technique, reaction onset potentials and reaction kinetics can be studied. In order to assess stability windows of electrolytes, two separate LSV measurements, one for electrolyte oxidation and one for reduction, need to be combined in order to avoid effects arising from decomposition products.

The sweep rate, $\frac{dE_{\mathrm{WE}}}{dt}$ is a crucial parameter in CV and LSV, as it has implications on important measured quantities such as onset potentials and peak currents. In order to avoid large overpotentials, small sweep rates of $0.1\,\mathrm{mV\,s^{-1}}$ to $1\,\mathrm{mV\,s^{-1}}$ are used in this work.

2.3.4 Galvanostatic cycling

Galvanostatic cycling (GC) is one of the most important techniques for testing battery systems. Whereas voltammetry forced the WE potential to programmed values, galvanostatic experiments impose a constant current on the WE.[269] The voltage needed to keep the current constant over time is measured and recorded. GC

offers a controlled and reproducible protocol to test battery cells under conditions resembling real operation under constant load. The technique requires the definition of vertex potentials limiting the voltage window. The potential window is chosen to contain the redox potential of the studied reaction and to exclude unwanted parasitic reactions, such as active material or electrolyte decomposition. To improve reproducibility and comparability, currents used in GC are usually normalised by mass or total capacity of the active material used. In battery research, this concept has been formalised in the so-called C-rates, where a rate of $a \cdot C$ corresponds to the current needed to (dis)charge the WE fully within $1/a$ h. The choice of current determines the information gained from the experiment. Because of current-dependent overpotentials, low-current GC experiments are needed to determine the maximum achievable capacity. However, at low currents side reactions can add a significant capacity which can falsely be interpreted as increased active material capacity. Therefore, a compromise between the two factors needs to be made. Typical slow rates used to determine the total capacity are $C/20$ or $C/10$. Through high-current GC measurements the system's rate capability can be assessed.

Typically, the recorded WE potential is plotted *vs* gravimetric charge, which is simply the integral of the current over the time since imposing the current divided by the mass of active material in the electrode. This presentation immediately reveals crucial information about the system, such as a material's specific capacity, charge and discharge potentials and reversibility. The coulombic efficiency can be determined per charge-discharge cycle by dividing the discharge capacity by the charge capacity. Additionally, information about the nature of electrode reactions can be obtained from the number and shape of plateaus found in the GC curve. For this analysis, the differential capacity dQ/dE plot can aid in interpretation and deconvolution of individual plateaus, especially in the case of slopy GC curves.[270]

2.4 Other methods

Other physicochemical and magnetic methods are used in this thesis but are of lesser importance to the findings.

Karl-Fischer (KF) titration is used to determine the water content of solvents for non-aqueous synthesis. This method uses a titration using elemental iodine to determine the water content of liquids.[271] The measurements in this work are taken on an automated Mettler Toledo C30S instrument.

Heat capacity measurements are carried out to study the magnetic disorder-to-order transition. The technique measures the energy needed to increase the temperature of a small amount of sample at variable temperatures. Discontinuities in the found temperature-dependence indicate second-order magnetic phase transitions. In this work, before measurement, the sample is prepared by pressing a pellet from the powder material. This is done using a stainless steel die set and a manual hydraulic press. The used sample mass is (2.82 ± 0.02) mg. The measurements are taken by Dr Dharmalingam Prabhakaran (Department of Physics, University of Oxford) using a Quantum Design PPMS instrument.

NMR spectroscopy is employed to determine the purity of the solvent used for non-aqueous synthesis. Briefly, NMR is based on the precession of nuclear spins in an external magnetic field. The precession frequencies vary between different nuclei and bonding environments due to a shielding effect. The frequencies are read out via a receiving coil in the time domain and processed via Fourier transform to find the resonant frequencies. From these, the chemical shifts can be determined.[272] In this work, an Oxford Instruments X-Pulse benchtop NMR spectrometer located in an argon-filled glovebox is used. Phase correction and peak indexing are carried out using MestReNova and ChemDraw software, respectively.

2.5 Chemicals

Reagent and analysis grade chemicals are used throughout this work. Special attention is paid to the key chemicals and precursors listed below.

For materials synthesis in chapter 3, three different cyanide precursors are used. NaCN is purchased from Acros Organics with a purity of 98%. Main contaminants according to the product specification are sodium hydroxide $(0.3 - 0.8\%)$, sodium carbonate $(0.2 - 0.8\%)$ and sodium formate $(0.1 - 0.5\%)$. KCN is obtained from

Sigma-Aldrich with a purity of 98%. Main anionic impurities according to product specification are SO_4^{2-}, Cl^- and SCN^-.

The used N-methylformamide (NMF) is purchased from Sigma-Aldrich with a purity of 99%. The solvent is dried over 3 Å molecular sieves (Sigma-Aldrich) and stored in an argon-filled glovebox.

Different chromium precursors are used for materials synthesis. $CrCl_2$ (99.99%, anhydrous) is sourced from Sigma-Aldrich. The chemical was removed from the ampule packaging in an argon-filled glovebox without exposing to air at any point. $K_3Cr(CN)_6$ (99.99%) is obtained from Sigma-Aldrich and vacuum-dried before use.

RbCl (99%) and CsCl (99.9%) are purchased from Sigma-Aldrich.

For electrochemical experiments in chapter 4, 1,2-Dimethoxyethane (DME) (anhydrous, Sigma-Aldrich) is used as electrolyte solvent. The solvent is dried over molecular sieves before use. Electrolyte salts sodium bis(fluorosulfonyl)imide (NaFSI) and potassium bis(fluorosulfonyl)imide (KFSI) are purchased from Solvionic.

In chapter 5, materials are synthesised from the precursors precursors $MnCl_2 \cdot 4\,H_2O$, $FeCl_2$ (anhydrous), $CoCl_2 \cdot 6\,H_2O$, $CuCl_2 \cdot 2\,H_2O$ and $K_3Fe(CN)_6$. The hydrated salts and $K_3Fe(CN)_6$ are dehydrated at 100 °C before use. Dry NMF is used again as reaction medium (see above).

3

Optimised synthesis and characterisation of chromium hexacyanochromate

Contents

3.1 Abstract 64
3.2 Motivation 65
3.3 Synthesis of reduced chromium hexacyanochromate . 69
3.4 Chemically oxidised chromium hexacyanochromate . . 77
3.5 Synthesis of mixed-valence chromium hexacyanochromate 84
3.6 The oxidation states of chromium hexacyanochromate 86
3.7 Conclusion 90
3.8 Experimental 90

3.1 Abstract

Chromium hexacyanochromate ($A_xCr[Cr]$) has been a sought-after PBA composition because of its unique magnetic and electrochemical properties. The material combines qualities that make it a promising material for two fields of application: molecular magnetism and batteries. For both of these applications, vacancy-free, crystalline materials with pure oxidation states are required. Achieving this goal has been proven elusive, in large parts due to the synthetic challenges associated with

this material composition, preventing the use of standard approaches developed for PBAs. Earlier work in this group lead to the development of a novel non-aqueous synthesis route, through with vacancy-suppressed chromium hexacyanochromate can be achieved.[273] However, the obtained small particle sizes and yield as well as ambiguity about the materials' oxidation states have hindered the characterisation of the material produced from it.

This chapter presents an optimisation of the non-aqueous synthesis of vacancy-free, highly crystalline chromium hexacyanochromate in both reduced and fully oxidised valence states. The achieved materials allow for a thorough physicochemical characterisation of morphology, crystal structure, composition and electronic state. Additionally, a synthesis strategy for the mixed-valent material is described. The analysis of these three materials allow for the resolution of the prevalent ambiguous and conflicting assignments of oxidation states reported in literature for this material system. The presented results provide important insights about the synthesis of air-sensitive PBAs, expand the understanding of the oxidation states of chromium hexacyanochromate and lay the foundation for the magnetic and electrochemical studies presented in chapter 4.

3.2 Motivation

$Cr^{III}[Cr^{III}]$ has been a material of interest in molecular magnetism because of its similarities in electronic structure to $KV^{II}[Cr^{III}]$, the PBA with the highest reported magnetic ordering temperature.[111] Unlike this material, $Cr^{III}[Cr^{III}]$ exhibits stability against oxidation in air, which could potentially increase its utilisation in real-world applications. In order to exploit the material's maximum magnetic interactions, the material needs to be synthesised with high crystallinity, a pure Cr^{III}/Cr^{III} oxidation state and minimal vacancies. These requirements are a direct consequence of the orbital theories and Néel's mean field theory presented in the introduction.

Chromium hexacyanochromate also shows promise in the realm of battery materials. As showed in the introduction, compositions based on hexacyanochromate

possess some of the lowest redox potentials among PBAs. The redox potentials of these compositions typically lie on the lower boundary of the stability window of aqueous electrolytes, which makes them possible anode materials for rechargeable aqueous Na- and K-ion batteries. With Cr in the P-site, the material has been reported to exhibit two reversible redox reactions per formula unit, which gives the material a high theoretical specific capacity.[221] In order to access the material's full capacity, a vacancy-less Cr[Cr] is needed.

It is apparent that the requirements for a high-T_C molecular magnet and a high-capacity battery anode material coincide. For both realms, a low vacancy concentration, high crystallinity as well as oxidation state purity are key to maximise performance. These are the metrics that need to be achieved via a suitable synthesis route.

The synthesis of many PBA materials with Fe, Mn or Co occupying the carbon-coordinated sublattice is usually simple. Upon mixing aqueous solutions of the chosen transition metal salt and hexacyanometallate complex in the desired oxidation state, the PBA readily precipitates as a crystalline powder. Additives can often be used to steer the synthesis towards forming low-vacancy PBAs. To achieve crystalline, low-vacancy Cr[Cr], however, this simple synthesis is not applicable due to constraints set by the chemistry of precursors and reaction intermediates.

Firstly, solvated Cr^{3+} ions are kinetically inert and thus do not allow for a direct synthesis of the material. It is well documented that the rate of ligand exchange for Cr^{3+} is very low,[274] which makes this ion not labile enough to coordinate to the nitrogen ends of the cyanide ligand. Attempts to modify the Cr^{3+} salt's anion to increase reactivity has led to the formation of an amorphous material.[83] This major impediment prohibits the synthesis of the material in the desired Cr^{III}/Cr^{III} oxidation state. Instead, it motivates the usage of Cr^{2+} species as transition metal source.

Secondly, an aqueous environment, albeit being the most widely used medium for PBA synthesis, poses severe problems. Its narrow electrochemical stability window contains neither the oxidation potentials of Cr^{2+} nor $Cr(CN)_6{}^{4-}$, rendering

aqueous solutions of the chosen precursors metastable in the absence of a catalyst or oxygen.[11, 216, 275, 276] Additionally, in aqueous solutions without excess cyanide, the $Cr(CN)_6^{4-}$ complex readily loses one of its cyanide ligands to form the penta-coordinate $Cr(CN)_5^{3-}$, a process that inhibits PBA formation.[277, 278] Theoretical results show that this ligand dissociation reaction is a result of strong electrostatic repulsion between the negatively charged ligands, which is only partly compensated by the central divalent Cr^{II}.[279] A sufficiently polar solvent can provide enough solvation energy to suppress this effect and stabilise the $Cr(CN)_6^{4-}$ complex. Therefore, if this complex is used, a solvent with high dielectric constant ε is required.

In previous works with chromium hexacyanochromates, mainly two synthesis strategies are followed to navigate through this synthetic challenge. A bulk synthesis is achieved through the usual precipitation from aqueous solutions.[131, 217, 221] As precursors, $Cr(CN)_6^{3-}$ and Cr^{2+} are used. The syntheses are carried out under absence of O_2, thus keeping the Cr^{2+} stable over the duration of the synthesis. The synthesis yields a crystalline, but highly vacant PBA with a composition of $Cr[Cr(CN)_6]_{2/3}$. The observation of vacancies dominating the charge neutrality is consistent with other mixed-valence PBAs and has been ascribed to an intrinsic thermodynamic effect.[273] The second synthesis route is via electrodeposition. This strategy uses an electrode surface immersed in a solution of $K_3Cr(CN)_6$ and a Cr^{3+} salt. Because of the inability of Cr^{3+} to be directly incorporated into the PBA structure, no precipitation ocurs initially. Only when the electrode is driven to sufficiently low potentials, are the Cr^{3+} species reduced to the labile Cr^{2+}, which immediately react and deposit a thin precipitate film onto the electrode surface. Depending on the reduction potential, materials with different vacancy concentration and crystallinity are achieved, however vacancies could not be fully suppressed.[67, 134, 280–282]

All of these established synthesis protocols lack a systematic strategy to form vacancy-free materials. For the bulk synthesis of mixed-valence chromium hexacyanochromate, the addition of an excess of large cations did not lead to a significant vacancy reduction.[131] Other common strategies to suppress vacancy

formation, such as the use of chelating agents, are not effective for mixed-valence PBAs.[59] In the case of electrochemical deposition, the parameters driving vacancy concentration and crystallinity are not well understood and appear very sensitive to small changes, which complicates finding the optimal synthesis conditions. This sensitivity was showcased by Buschmann *et al.*, who found that the roughness of the electrode surface can change the structure of the deposited material from crystalline to amorphous.[67]

Studies of chromium hexacyanochromate are additionally impeded by the limited use of standard characterisation techniques. For instance, ICP cannot be used to determine the vacancy content in the structure because of the occupation of both the P and R sites with the same species. Also X-ray photoelectron spectroscopy, which is widely used to determine oxidation states and chemical environments, has been reported to be unable to resolve the differences between chromium hexacyanochromates in different oxidation states.[67] It has been shown that FTIR spectroscopy can be well suited to distinguish the oxidation states of the material. However, due to the materials' air-sensitivity in the non-oxidised state and the non-ideality of the materials achieved so far, there is ambiguity over the interpretation and assignment of the found peaks.

To tackle the issues at hand, previous work by Wheeler in this group has led to the development of a synthetic procedure capable of producing crystalline Cr[Cr] nanoparticles with suppressed vacancies.[273] The synthesis comprises of a precipitation reaction of reduced chromium hexacyanochromate from non-aqueous solutions and a subsequent chemical oxidation. NMF was identified as the optimal synthesis medium since it combines three crucial properties: its dielectric constant is high enough to stabilise the intermediate $Cr(CN)_6{}^{4-}$ complex, it solvates the needed precursors and due to its large molecular size it is unable of entering the structure and stabilising vacancies. A chemical oxidation of the reduced material in acidified water succeeded the synthesis and yields the desired $Cr^{III}[Cr^{III}]$. The low yield and small particle sizes of $\approx 10\,\mathrm{nm}$ found in this work complicate the characterisation, especially since the composition is not accessible using ICP but might be obtained

from structural refinement.[273] So far, a complete and quantitative analysis of the material synthesised via the novel approach is therefore missing.

This chapter describes an optimised synthesis procedure for vacancy-less Cr[Cr] in different oxidation states. The formed materials are characterised via quantitative physicochemical techniques. The work in this chapter lays the foundation for the study of the magnetic and electrochemical properties of Cr[Cr] presented in chapter 4.

3.3 Synthesis of reduced chromium hexacyanochromate

The reduced chromium hexacyanochromate is the intermediate stage for the formation of the desired oxidised Cr[Cr]. It is, however, an interesting material in its own right and important for the understanding of this materials system in general. Therefore, this composition is synthesised, isolated and studied without further oxidation.

Generally, the material is synthesised via precipitation reaction from non-aqueous solutions under inert atmosphere. The first solution contains a simple cyanide (NaCN or KCN) and an alkali metal chloride salt (RbCl or CsCl) dissolved in anhydrous NMF. The second solution contains anhydrous $CrCl_2$ dissolved in anhydrous NMF. The $CrCl_2$ solution is added dropwise into the cyanide-containing solution under vigorous stirring on a hotplate at a set temperature. A black precipitate immediately forms upon mixing, according to the formula

$$2\,Cr^{2+} + 6\,CN^- + 2\,A^+ \longrightarrow A_2Cr[Cr(CN)_6], \tag{3.1}$$

where A=Rb, Cs. Na^+, K^+ and Cl^- are not involved in the reaction and stay in solution. The precursor ratios are chosen to be stoichiometric between Cr^{2+} and CN^-, and to obtain twofold excess of Rb^+ or Cs^+. This is to ensure the reaction is not limited by the availability of inserting ions.

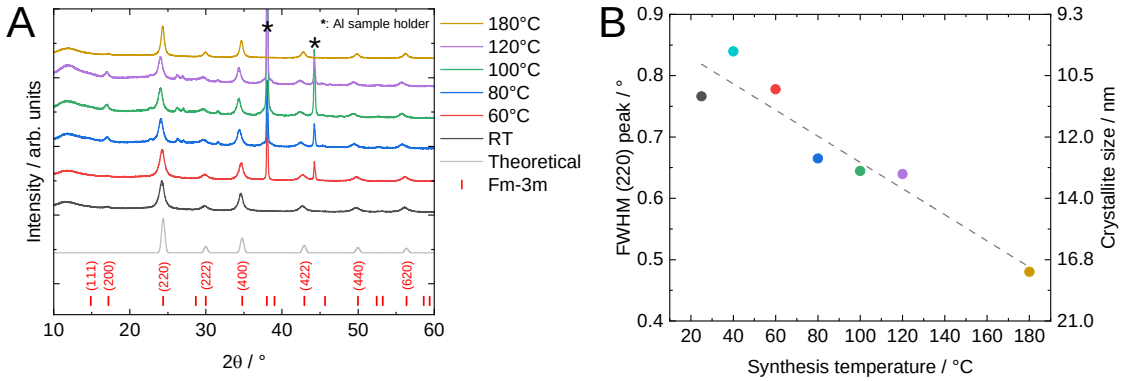


Figure 3.1: Effect of temperature during synthesis of reduced chromium hexacyanochromate. XRD of materials synthesised at temperatures of RT to 180 °C (A). All materials can be indexed in the $Fm\bar{3}m$ space group. A theoretical diffractogram for the ideal $Rb_2Cr[Cr]$ is shown in light grey for reference. Sharp peaks indicated by an asterisk stem from the aluminium sample holder. Variation of peak broadening with synthesis temperature (B). The FWHM of the most intense (220) peak can be read off the left axis. Crystallite sizes are estimated using the Scherrer equation 3.2 and are given on the right axis. The peak broadening decreases with increasing synthesis temperature, corresponding to an increase in crystallite size. The dashed line is a guide to the eye.

Because of the limited choice in solvent and precursor species, the main optimisation factors for the synthesis are the synthesis temperature and precursor concentrations.

In order to achieve the goal of high yield and larger particle sizes, firstly the concentration of precursor solutions are increased. The solubility of all used precursors is tested and the used concentrations are chosen close to their solubility limit. The synthesis is carried out using a 240 mM NaCN or KCN and 160 mM RbCl or CsCl solution, and a 200 mM $CrCl_2$ solution with respective volumes to match the ratios given above (see Experimental for details).

The effect of different temperatures during synthesis is studied via separate syntheses using NaCN and RbCl precursors. Upon mixing, the material precipitates immediately at all tested temperatures. The diffractogram of the materials formed can all be indexed in the prototypical $Fm\bar{3}m$ space group, which confirms the formation of PBA materials, as shown in fig. 3.1A. The found peaks show considerable broadening, indicating small particle sizes. In fig. 3.1B, the FWHM of the highest-intensity Bragg peak (220) for each material is plotted *vs* synthesis temperature. It

is apparent that increasing the temperature decreases peak broadening. The mean particle sizes d are estimated using the Scherrer formula[283]

$$d \approx \frac{0.93\lambda}{b \cdot cos(\Theta)}, \tag{3.2}$$

where λ is the X-ray wavelength and b and Θ are the FWHM and Bragg angle of the diffraction peak. This analysis shows that the mean particle size could be increased from $\approx 10\,\text{nm}$ to about 17.5 nm by increasing the synthesis temperature to 180 °C. Since this is the boiling point of NMF, a further increase in temperature is not possible. The increase in particle size upon heating can be understood via the reaction's crystallisation kinetics and thermodynamics. Due to the low solubility of PBAs, supersaturation is reached already at low concentrations. Hence, the crystallisation is strongly dominated by particle nucleation. Due to surface and volumetric energy contributions, only nuclei larger than the critical size are thermodynamically stable and can persist. Since this critical size increases with temperature,[284] in nucleation-dominated reactions a larger particle size can be achieved at increased temperatures. Even at 180 °C, the particle size is still small compared to typical PBAs prepared from aqueous media. This is likely due to a ligandisation of the particles' surface by the NMF solvent, as has been proposed in chemically similar media.[285] This could lower the particles' surface tension and thus the energy barrier for nucleation, resulting in a decreased critical nuclei size.

As can be seen in the XRD patterns, the materials exhibit a large difference in the intensity of their (200) Bragg peak, located around 17°. This is due to an unwanted, partial materials oxidation process. The theoretical pattern for an ideal $Rb_2Cr[Cr]$ material is shown alongside the measured data in fig. 3.1A. In this simulated pattern, the intensity of the (200) peak relative to the most intense (220) peak amounts to 0.5%. This small intensity is a result of out-of-phase scattering of the Rb^+ planes and the Cr planes (with contribution of the respective cyanide ligands) which scatter almost equally in intensity. When material oxidation takes place, Rb^+ is extracted from the interstices, leading to a decreased compensation of scattered signal and therefore to the observation of increased (200) intensities. In

the shown XRD patterns, this is especially obvious in the materials synthesised at 80 °C, 100 °C and 120 °C. It bears mentioning that this oxidation is however not attributable to certain synthesis temperatures, but is purely caused by different amounts of exposure to oxidants such as air or moisture and is therefore variable from synthesised batch to batch.

This indicator for oxidation is supported by the material's FTIR spectrum exhibiting two peaks in the ν(CN) region at $(2051 \pm 9)\,\mathrm{cm}^{-1}$ and $(1983 \pm 13)\,\mathrm{cm}^{-1}$ (see fig. 3.2, grey line), while only one is expected for this composition in its pure, fully reduced oxidation state.[220] To investigate the origin of this unwanted oxidation, both reagents and procedures are scrutinised. The purity of the NMF solvent was checked via NMR (see fig. 3.3A) and FTIR spectroscopy, which indicated no significant impurities. The water content of the solvent measured by KF titration amounts to 0.7 ppm to 3.3 ppm for different batches, the solvent is therefore considered anhydrous. The water content of the dried RbCl precursor is measured to be negligibly small. The water content of the cyanide precursor cannot be determined using the KF titration equipment because of safety regulations. The NaCN and KCN precursors are therefore vacuum-dried at 300 °C instead to ensure complete dehydration. In the case of $CrCl_2$, the compound's low oxidation potential prevents the use of KF titration as it interferes with the titration reaction. It is purchased anhydrous in a sealed ampule and is never exposed to moisture and is therefore considered free of water as well. The synthesis liquid's electrochemical stability window is tested as close as possible to synthesis conditions via LSV of a 160 mM RbCl solution in NMF. This test is done to rule out solvent reduction as the parasitic reaction leading to material oxidation. As shown in the resulting voltammogram in fig. 3.3B, both the oxidation potentials of Cr^{2+} and $Cr(CN)_6{}^{4-}$ lie well within the synthesis liquid's stability window, which confirms that the solutions are electrochemically stable.

As no problems with reagents are identified, several synthesis parameters have been investigated systematically. This includes changing precursors and the successive washing and drying steps. Fig. 3.2A shows the FTIR spectra for

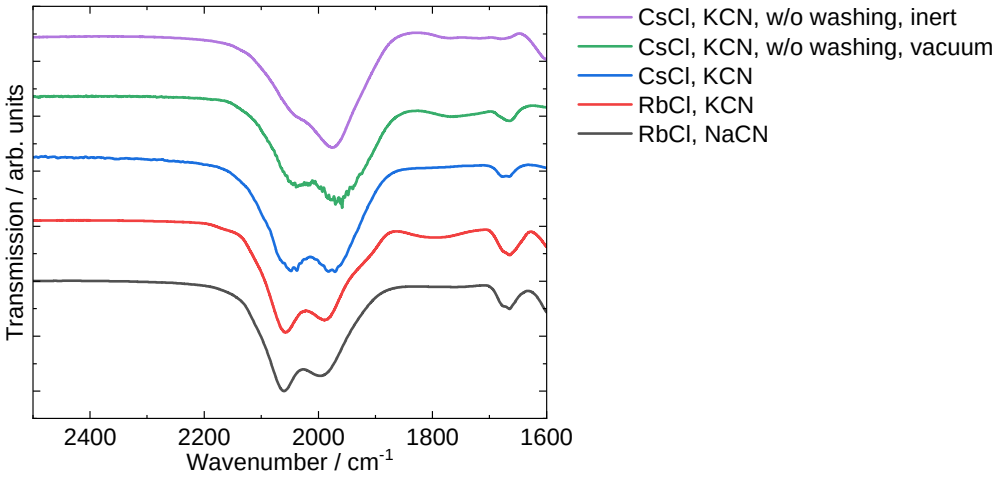


Figure 3.2: νCN region of the IR spectrum of reduced chromium hexacyanochromate materials synthesised under different conditions. Materials are formed using RbCl and NaCN, RbCl and KCN or CsCl and KCN, respectively, washed and dried in a vacuum oven (grey, red and blue lines, respectively). Additional materials are made using CsCl and KCN, are not washed, then dried in a vacuum oven (green line) or inside an argon-filled glovebox (purple line). In the IR spectra of all materials, two absorption lines are found at $(2051 \pm 9)\,\mathrm{cm}^{-1}$ and $(1983 \pm 13)\,\mathrm{cm}^{-1}$ with different peak ratios, indicating different extents of oxidation.

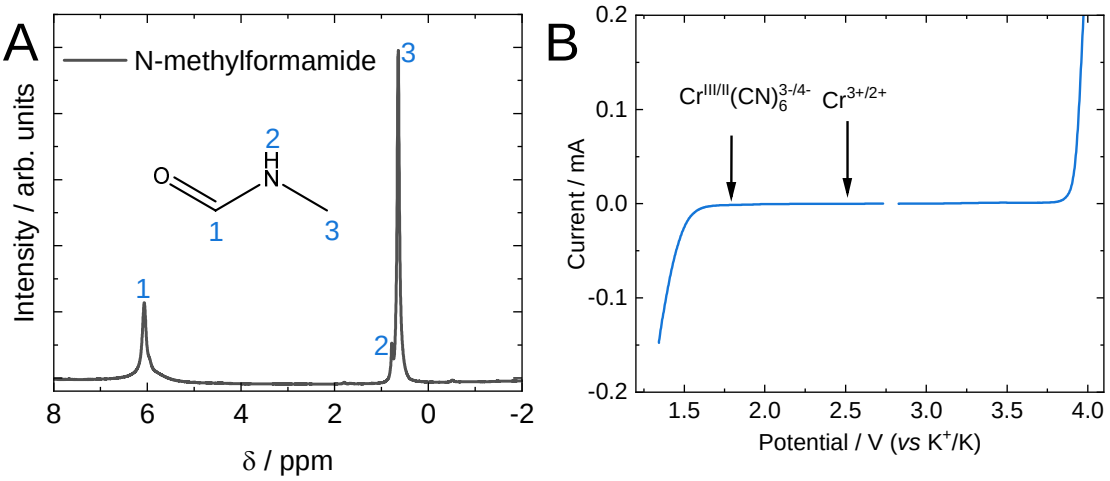


Figure 3.3: Purity and stability of NMF. ^{1}H-NMR spectrum of NMF used for synthesis (A). No additional peaks are found, which confirms the absence of considerable amounts of impurities. Electrochemical stability window of a 160 mM solution of RbCl in NMF (B). Both the oxidation potentials of both Cr^{2+} and $Cr(CN)_6{}^{4-}$ lie within the electrochemically stable region, ruling out the solvent as possible oxidiser.

materials synthesised in different conditions. The rationale behind the changes follow different strategies. The NaCN precursor is identified as potentially problematic because if its hydroxide impurities (see Methods), which is known to attack and substitute with cyanide ligands in the PBA. The precursor is swapped for KCN, whose specifications do not list potentially detrimental impurities (red line). As a next step, RbCl is exchanged for CsCl in the synthesis (blue line). The large Cs^+ is known to be difficult to remove from PBA interstices, especially when vacancy-based diffusion channels are absent.[190, 286] Its inability to exit the structure could hinder oxidation processes which requires ions to be released. Both these changes affect the relative intensities of the peaks found in the FTIR spectrum in favour of the lower-wavenumber peak, which corresponds to the fully reduced material. Next, two materials are measured before washing. This avoids the introduction of additional solvent and centrifugation. Since the centrifugation is carried out outside the glovebox, which, albeit using an additionally sealed air-tight vial, poses a potentially critical step for contamination with oxygen and moisture. Additionally, the influence of drying conditions are tested by drying the two identical materials in an air-tight vacuum oven outside the glovebox (green line) and on a hotplate inside an argon-filled glovebox (purple line), respectively. The FTIR analysis shows that all the considerations above can decrease oxidation to some degree but not fully, as is obvious from the presence of the second, higher-wavenumber peak in all spectra. Taken together, the results suggest that the oxidation is likely to occur from several different sources, which underlines the extreme air-sensitivity of the reduced $Rb_2Cr[Cr]$ and $Cs_2Cr[Cr]$.

Even though the obtained chromium hexacyanochromate is slightly oxidised, the described synthesis allows for a quantitative physicochemical analysis and the clear separation of the individual oxidation states' FTIR signals, which was not possible in previous work.[273] Since the material needs to be chemically oxidised for later studies, the cesiated compound is not suitable because of the earlier mentioned difficulties in removing Cs^+ from the material. Therefore, $Rb_{2-x}Cr[Cr]$ is the composition which will be analysed in detail. The following discussion is solely

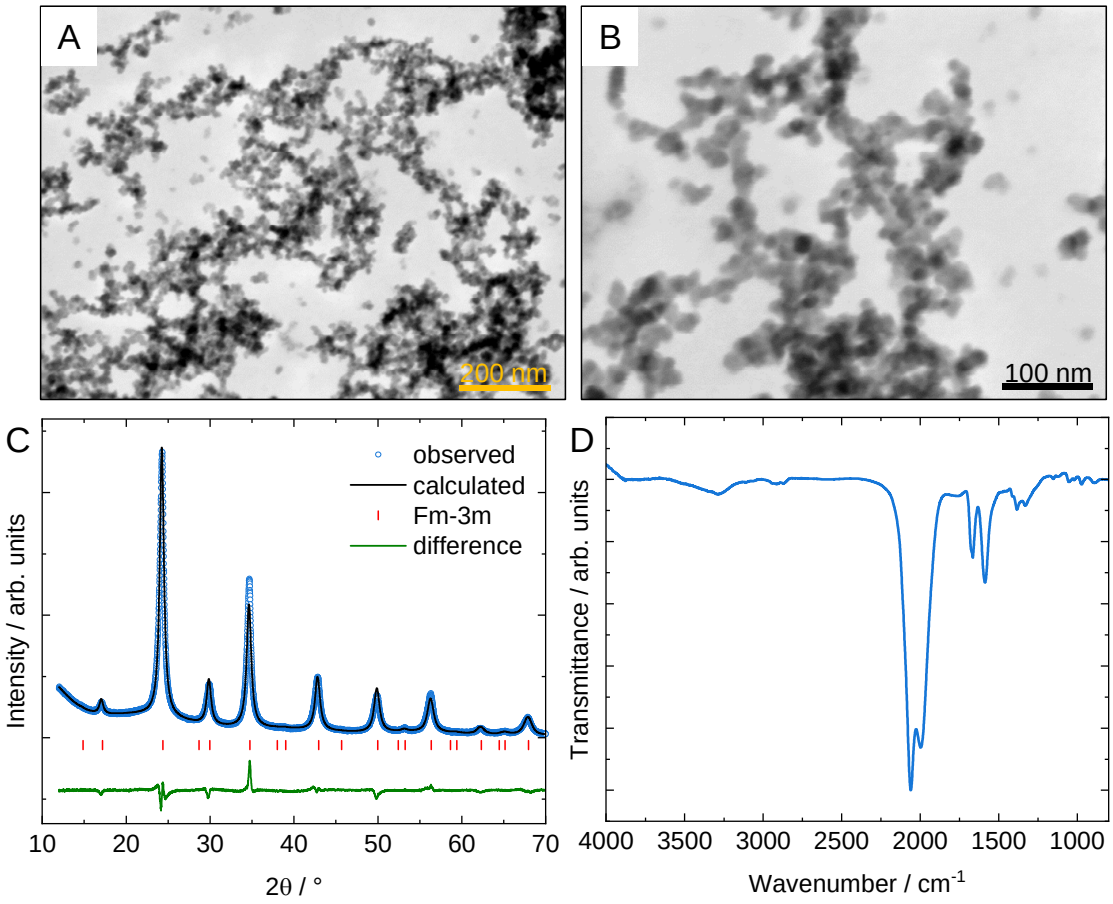


Figure 3.4: Characterisation of $Rb_{2-x}Cr[Cr]$. Transmission-mode SEM micrographs of the synthesised particles at different magnifications (A, B). The material comprises of nanoparticles with diameters of $\approx 20\,\text{nm}$. XRD pattern (C) and FTIR spectrum (D) of the material. The found crystal structure is in the cubic space group $Fm\bar{3}m$. The IR spectrum shows the aforementioned two ν(CN) peaks as well as characteristic peaks from residual NMF solvent below $1700\,\text{cm}^{-1}$.

concerned with the reduced $Rb_{2-x}Cr[Cr]$ material obtained from the optimised high-concentration, high-temperature synthesis using KCN as precursor.

Fig. 3.4A and B show results form transmission-mode SEM imaging. The obtained particle sizes are in the range of about 15 nm to 30 nm. This matches well with the estimations from the synthesis optimisation discussed above. The material's crystal structure is studied using Rietveld analysis of XRD data. Fig. 3.4C shows the measured and refined XRD patterns and their difference. The peak positions indicate a cubic crystal symmetry and all peaks can be fitted in the $Fm\bar{3}m$ space group, which is the prototypical PBA structure. The lattice parameter is determined as 10.31 Å. The refined particle size is 17 nm, which is in excellent

Atom	Multiplicity	Occupancy	x	y	z	U_{iso} / Å^2
Cr(1)	4	0.997(19)	0	0	0	0.021(2)
Cr(2)	4	1	0.5	0	0	0.021(2)
C	24	0.997(19)	0.200(2)	0	0	0.024(3)
N	24	0.997(19)	0.301(2)	0	0	0.024(3)
Rb	8	0.839(13)	0.25	0.25	0.25	0.079(2)
Global Fit	crystallite size: 17 nm, lattice parameter: (10.3142 ± 0.0005) Å $R = 2.99\%$, $wR = 4.29\%$					

Table 3.1: Structural parameters from Rietveld refinement for the reduced chromium hexacyanochromate. U_{iso} values of C and N as well as Cr(1) and Cr(2) are constrained pairwise to be the same, in order to reduce the number of independent variables in the refined model.

agreement with microscopic imaging. The disappearance of the (111) peak indicates an almost equal scattering from the P and R sublattices, which implies a near-zero vacancy content.[273] This qualitative argument can be made because of the negligible difference in scattering from the C and N in the structure. From Rietveld refinement, the hexacyanochromate occupancy is quantified as (99.7 ± 1.9) %, which is within error of the ideal stoichiometry of a vacancy-less material. The amount of Rb in the structure is determined as (1.678 ± 0.026) per formula unit. The full composition determined from refinement is therefore $Rb_{1.678}Cr[Cr(CN)_6]_{0.997}$. The whole set of refined structural parameters is summarised in table 3.1.

The Rb content is checked additionally via ICP-MS, which indicates a Rb : Cr ratio of $(0.738 \pm 0.013) : 1$. Using the vacancy content obtained from refinement, since it cannot be determined using ICP, this corresponds to a composition of $Rb_{1.474}Cr[Cr(CN)_6]_{0.997}$. The Rb : Cr ratio from both structural refinement and elemental analysis is below the expected parity for an ideal reduced material. This deviation in Rb content from the ideal stoichiometry is caused by the partial oxidation of the material discussed above. The different Rb amounts determined via the two methods could indicate a further oxidation in between measurements. From FTIR spectroscopy, we can gain insights into the individual oxidation states. The material's FTIR spectrum is shown in fig. 3.4D. In the ν(CN) region, the aforementioned peaks at 2060 cm^{-1} and 1997 cm^{-1} are visible. A comparison to the material modelled by DFT[220] reveals that the lower-wavenumber peak

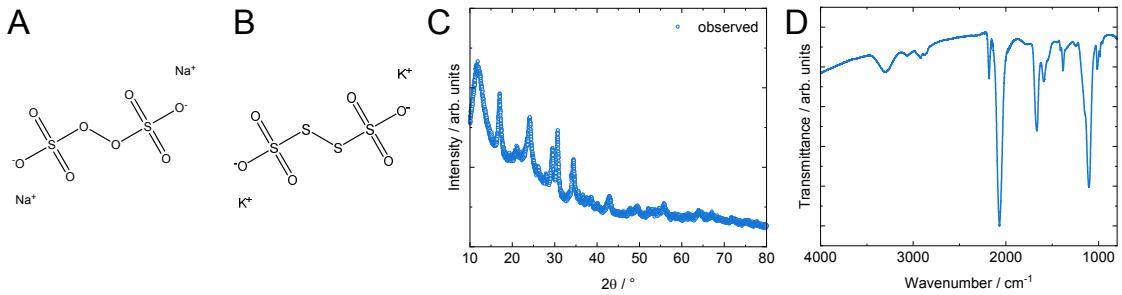


Figure 3.5: Attempted non-aqueous chemical oxidation using sulfur oxyanions. Chemical structures of sodium persulfate (A) and potassium tetrathionate (B) tested as oxidisers. XRD pattern of chromium hexacyanochromate sample after attempted oxidation with tetrathionate in NMF (C). Numerous additional peaks are obtainable, likely coming from decomposition products of the material. FTIR spectrum of the same sample (D). The shift in absorption band intensities as well as the occurrence of a higher-wavenumber peak at 2182 cm^{-1} shows partial oxidation has occurred, however not to completion.

corresponds to the stretch of $Cr^{I}-C\equiv N-Cr^{III}$ and the higher-wavenumber peak to $Cr^{II}-C\equiv N-Cr^{III}$. It is clear that the oxidation therefore happens at the Cr_C site, which is partly in Cr^{I} and Cr^{II} state. Below 1700 cm^{-1}, several intense absorption lines can be found, corresponding to vibrations of the amide group and C–H bonds, evidencing the presence of residual NMF solvent. This is confirmed by small, sharp bands between 2800 cm^{-1} and 3000 cm^{-1} stemming from CH and CH_3 stretching modes of NMF.[287]

3.4 Chemically oxidised chromium hexacyanochromate

Because of its absence of vacancies and the ability of Rb to be removed from the structure, the synthesised $Rb_{2-x}Cr[Cr]$ is an ideal intermediate to achieve the desired Cr[Cr]. Therefore, to synthesise the oxidised material, the reduced material is synthesised and, instead of dried, processed further. Since the material is being oxidised as a next step, the non-pure oxidation state of the reduced material is of no concern for the synthesis of Cr[Cr].

To achieve bulk oxidised Cr[Cr] particles, a controlled chemical oxidation route is needed. The chosen process should ideally fulfil several requirements, which narrow the choice of suitable oxidisers. First, the oxidiser must keep the PBA

structure intact. Second, the oxidiser is ideally soluble in the non-aqueous reaction medium to facilitate the overall process. Third, the oxidiser should not precipitate after reduction as to not contaminate the material. Fifth, the oxidiser should not contain transition metal species. This is to ensure that no oxidiser is incorporated into the PBA lattice through a change of bonding, to which hexacyanochromates are susceptible.[288] These considerations severely constrain the choice of possible oxidising agents. As viable candidates, two sulfur oxyanions are identified, as seen in fig. 3.5A and B. One is the strong oxidiser peroxodisulfate $S_2O_8{}^{2-}$, which reduces to sulfate anions at 2.01 V *vs* SHE.[289, 290] The second compound is tetrathionate $S_4O_6{}^{2-}$, which reduces to thiosulfate at 198 mV *vs* SHE.[291] The nature of cations plays no significant role in the oxidation process and is chosen based on the commercial availability of salts. Due to the insolubility of $Na_2S_2O_8$ in NMF, only $K_2S_4O_6$ is tested. After oxidation with a solution of $K_2S_4O_6$ in NMF at 100 °C, very little amount of material is recovered. Fig. 3.5C shows the XRD of the sample after oxidation. It is apparent that numerous new peaks appear, which in light of the low yield likely stem from decomposition products, indicating material breakdown. The corresponding FTIR spectrum, shown in fig. 3.5C, indicates that oxidation has occurred, however not to completion. This is evident from the increased intensity of the band corresponding to $Cr^{II}-C{\equiv}N-Cr^{III}$ and the appearance of a small new, higher-wavenumber band at 2182 cm^{-1}, corresponding to the fully oxidised material. Overall, both of the tested sulfur oxyanion compounds are unsuitable as oxidiser for the chosen PBA.

These setbacks in finding a suitable oxidiser in non-aqueous media cause the decision to revert to using aqueous media for oxidation. Apart from adding complexity to the synthesis procedure, using water has the disadvantage of the oxidation reaction being a parasitic hydrogen evolution reaction according to the idealised pathway

$$Rb_2Cr[Cr(CN)_6] + 2\,H_3O^+ \longrightarrow Cr[Cr(CN)_6] + 2\,Rb^+ + H_2 + 2\,H_2O. \qquad (3.3)$$

This approach has two main drawbacks. Firstly, the oxidation happens in an uncontrolled manner. As such, it does not allow for the study of intermediate oxidation states, since both reduction potentials of the material lie below the reduction potential of water and water is present in vast excess. In this case, the desired outcome is a fully oxidised material, so this downside is passable. Secondly, the reaction consumes protons, which elevates the dispersion's pH value. Since PBAs are unstable in basic media, this must be counteracted by using a sufficiently acidic solution to provide excess H_3O^+.

On the upside, acidic solutions have been shown to maintain the PBA structure while oxidising the material to completion in earlier work.[273] It is assumed that the oxidation reaction is limited by the ionic transport of the large Rb^+ through the vacancy-less PBA structure. Therefore, the larger particle sizes potentially cause the reaction to be more sluggish. Here, aqueous media can play an additional beneficial role: water enables fast interfacial ion transfer into the solvated state and is suspected to aid ionic transport within the PBA structure.[186]

Several experiments are carried out to find the optimal aqueous oxidation conditions. FTIR spectroscopy is used to assess the oxidation states of the individual materials. Full oxidation is achieved by dispersing the synthesised reduced material in excess 0.1 M HNO_3 solution in ultrapure water, and letting the reaction progress over a > 10 h period at 95 °C under magnetic stirring. The dispersion must be stirred constantly to ensure homogeneous mixing at all times. This is because the settling of material during reaction causes local increases in pH and thus material decomposition in the basic environment. During the oxidation, the dispersion's overall pH value rises and the colour of dispersed material changes from black to a light brown. After oxidation, the material is collected via centrifugation, during which an almost colourless, clear supernatant is found. This indicates a non-destructive oxidation process with high material recovery.

Figs. 3.6 show results from transmission electron microscopy of the fully oxidised material at different magnification. Particle sizes are in a similar range found for the reduced material, as visible in low-magnification micrographs (fig. 3.6A).

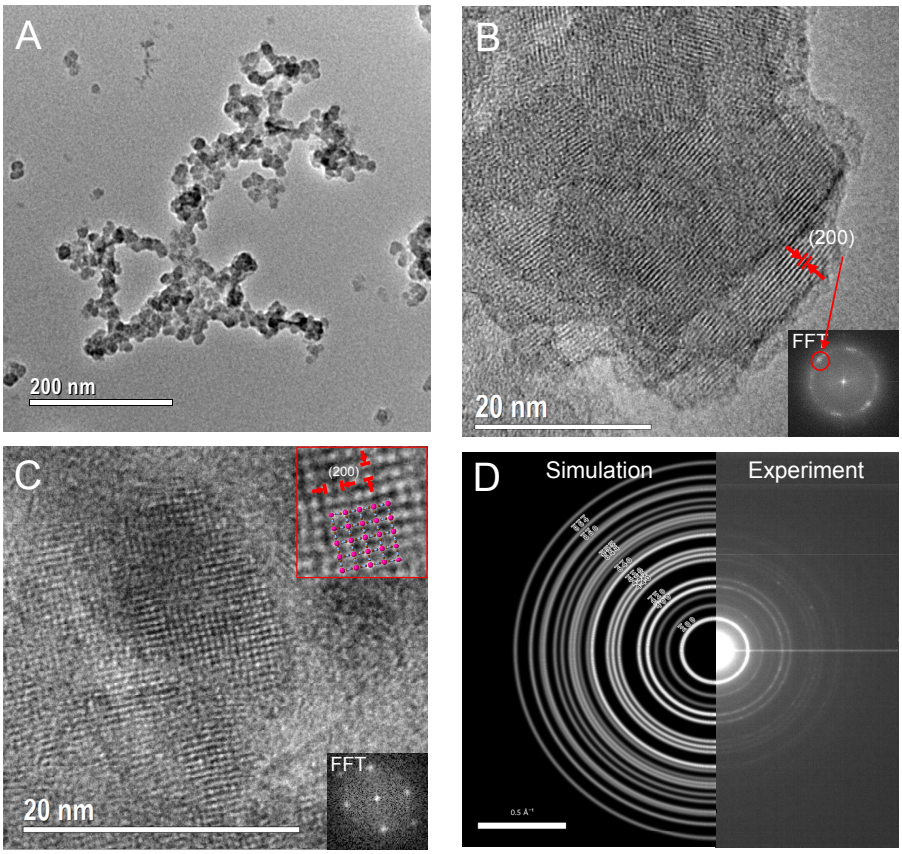


Figure 3.6: Transmission electron micrographs of fully oxidised chromium hexacyanochromate. Low-magnification imaging (A) shows particle sizes in the range of about 10 nm to 20 nm. Coherent lattice fringes are visible in individual particles over about 30 nm (B). The material's cubic crystal structure is directly probed by [100] zone axis imaging (C) and the corresponding FFT (C, inset) as well as the pSAED pattern (D), which matches the simulated pattern. Data acquired by Ruomu Zhang, Oxford Materials.

This underlines the non-destructiveness of the chosen oxidation protocol. At high magnification, the images show that individual larger particles exhibit a coherent orientation of lattice fringes over about 30 nm (see fig. 3.6B), evidencing that the particles are individual single crystallites. The high crystallinity and cubic crystal arrangement is directly visible from the [100] zone axis image (fig. 3.6C). The material's powder selected-area electron diffraction (pSAED) pattern, shown in fig. 3.6D, matches with the simulated theoretical pattern for the ideal Cr[Cr] in the cubic $Fm\bar{3}m$ space group.

XRD data (fig. 3.7A) give more detailed insights into the structural properties of the bulk material. The material has a face-centred cubic crystal structure, again in the space group $Fm\bar{3}m$. The lattice parameter is determined as 10.42 Å. In

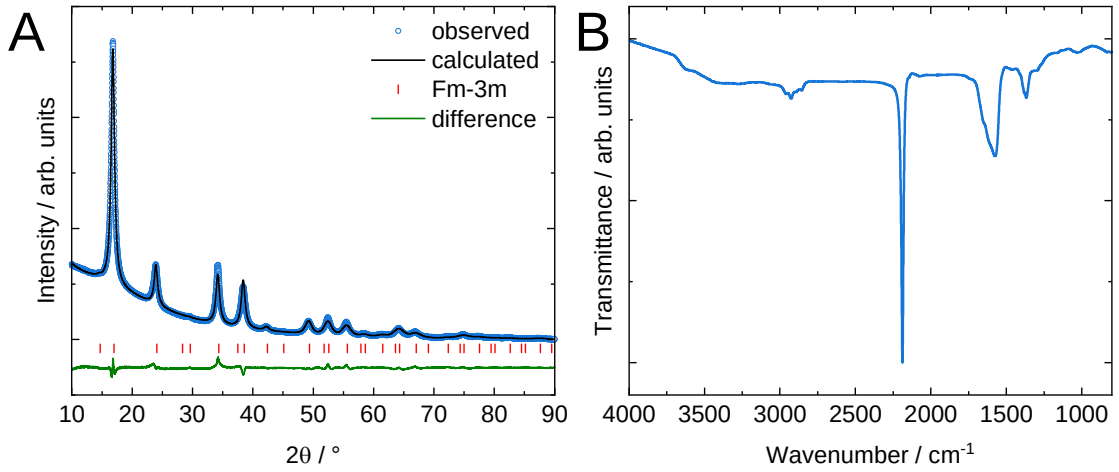


Figure 3.7: Characterisation of fully oxidised chromium hexacyanochromate. The XRD pattern (A) is refined in the cubic $Fm\bar{3}m$ crystal structure. In the FTIR spectrum (B), a single, intense absorption band is obtained at 2186 cm^{-1}, proving a pure and fully oxidised state. The remaining peaks indicate the presence of residual NMF and water.

comparison to the reduced material, the lattice expands upon oxidation. While at first glance counter-intuitive, since Rb^+ ions are removed from the interstitial sites, this behaviour is well-documented for PBAs. The reason for this phenomenon are the increased electrostatic interactions between the more negatively charged hexacyanometallate and P- and A-site anions as well as differences in Cr−C bonding due to the added electron density causing lattice contraction in the reduced state.[292, 293]

The material's composition is determined by combined elemental analysis using ICP-MS and Rietveld refinement of XRD data. During sample digestion for ICP analysis, a remarkable stability of the material in extremely acidic conditions is observed. The material remained visibly intact after treatment with heated concentrated nitric and hydrochloric acids. Full digestion is only achieved via a treatment with a mixture of four parts of concentrated nitric acid and one part of concentrated sulfuric acid acting as a high-temperature oxidiser, in a pressurised microwave digestor vessel heated to 180 °C. This high stability is likely related to the inertness of octahedrally coordinated Cr^{3+} towards ligand exchange. ICP-MS does not find residual Rb in the structure, which shows that the Rb in the interstitial sites is entirely extracted, as is expected for a fully oxidised material. Based on this

Atom	Multiplicity	Occupancy	x	y	z	U_{iso} / Å^2
Cr(1)	4	0.996(7)	0	0	0	0.0111(4)
Cr(2)	4	1	0.5	0	0	0.0111(4)
C	24	0.996(7)	0.175(1)	0	0	-0.00001(117)
N	24	0.996(7)	0.2931(7)	0	0	-0.00001(117)
Global Fit	crystallite size: 13 nm, lattice parameter: (10.4354 ± 0.0007) Å $R = 2.17\%$, $wR = 3.05\%$					

Table 3.2: Structural parameters from Rietveld refinement for the oxidised chromium hexacyanochromate. U_{iso} values of C and N as well as Cr(1) and Cr(2) are constrained pairwise to be the same, in order to reduce the number of independent variables in the refined model. Meaningful values for the isotropic displacement parameters of C and N could not be obtained from the refinement.

observation, Rb is omitted from the model used for structural refinement. Rietveld analysis quantifies a composition of $Cr[Cr(CN)_6]_{0.996\pm0.007}$, a virtually defect-free $Cr^{III}[Cr^{III}]$. The hexacyanochromate occupancy agree well with that found in the reduced material, which indicates that no vacancies are introduced upon oxidation. All refined structural parameters are summarised in table 3.2

The infrared absorption spectrum (fig. 3.7B) shows absorption lines in three regions. In the ν(CN) wavenumber region, a single, intense peak is observed at 2186 cm^{-1}. The absence of other peaks or shoulders in this region and the shift towards higher wavenumbers indicates that the material is in the pure, oxidised state. Again, several low-wavenumber (< 1700 cm^{-1}) peaks and peaks between 2800 cm^{-1} and 3000 cm^{-1} show the presence of residual NMF. The presence of residual NMF even after several washing cycles with H_2O followed by aggressive drying under vacuum is another indicator of strong coordination of the highly polar molecules to the PBA. A broad peak at around 3620 cm^{-1} can be assigned to ν(OH) and shows the presence of residual water, whose sharp δ(HOH) band expected around 1600 cm^{-1} overlaps with the amide absorption band of NMF.

The amount of residual solvent is determined via thermogravimetric analysis (fig. 3.8). The material's mass loss curve upon heating to 180 °C shows a reduction of 1.1%. This mass loss can be ascribed to the evaporation of the residual molecules of NMF and water. However, the quantities of removed solvents are too small to be distinguished by the used analysis of evolved gases. The small mass loss is

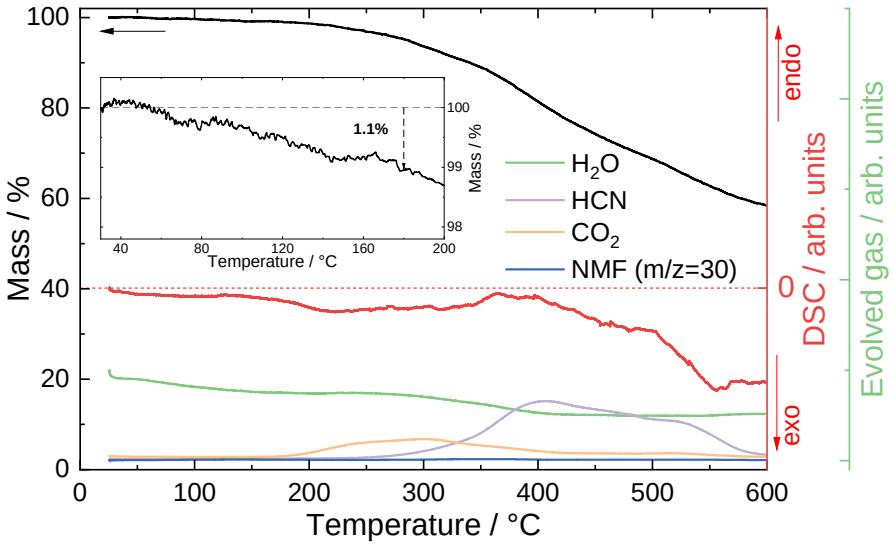


Figure 3.8: TGA-MS analysis of Cr[Cr]. The material loses 1.1% of its mass likely due to solvent evaporation before a temperature of 180 °C. At this temperature, the DSC signal displays the onset of a exothermic process. The coupled gas analysis registers the evolution of CO_2 at this temperature, which indicates material decomposition. Beyond 300 °C, the decomposition becomes more severe, with rapid decay of sample mass and the typical evolution of HCN from the material. Throughout the measurement, the water signal remained roughly constant at background levels.

consistent with the absence of solvent-filled vacancies. Above 180 °C, the material's decomposition starts, marked by the exothermic DSC signal. The onset of material decomposition is accompanied by the evolution CO_2 and, shortly after, HCN. It is noteworthy that this decomposition temperature coincides with the boiling point of NMF (183 °C). The mass loss is however unambiguously caused by decomposition, as evidenced by the typical exothermic behaviour and decomposition products.[18] Only trace amounts of NMF are found in the evolved gas analysis, which further justifies the assignment.[294] The found water level stayed around background level over the whole temperature range tested.

Taken together, the physicochemical characterisation confirms the synthesis of highly ordered, nanocrystalline and practically vacancy-less Cr[Cr] with a very low amount of residual solvent.

3.5 Synthesis of mixed-valence chromium hexacyanochromate

The absence of vacancies in the synthesised Cr[Cr] is likely not due to the presence of excess counter-ions during material formation, but rather demonstrates the used solvent's inability to stabilise vacancies in the PBA structure, as was reasoned in earlier work.[273] If this is true, the solvent's effect counteracts the thermodynamic advantage for vacancies in mixed-valence ($i + j = 5$) PBAs. If it outweighs the driving force for vacancies, this could allow for the formation of vacancy-free mixed-valence PBAs. This hypothesis is tested using chromium hexacyanochromate as model system.

The reaction is carried out using the commercially available $CrCl_2$ and $K_3Cr(CN)_6$ precursors dissolved in anhydrous NMF. The amounts of precursors are chosen to fulfil a stoichiometric ratio between Cr^{2+} and $Cr(CN)_6{}^{3-}$ and therefore contain K^+ in excess. The synthesis and all processing steps are carried out without exposure to air in an argon-filled glovebox or, wherever necessary, in an additionally sealed air-tight vial. To increase the particle size, a synthesis temperature of 180 °C is used again. When the $CrCl_2$ solution is added dropwise to the $K_3Cr(CN)_6$ solution, a dark brown precipitate forms immediately.

The material is analysed after washing with NMF and vacuum-drying. Fig. 3.9A shows the material's XRD pattern. All peaks can be indexed using the cubic $Fm\bar{3}m$ space group, which confirms the formation of a PBA material. The determined lattice parameter is 10.52 Å. This constitutes a larger unit cell volume than both the reduced and fully oxidised chromium hexacanochromates shown above. This is unexpected, since the volume predicted by DFT lies between the higher and lower oxidation state.[220] The observation is reproducible across several different syntheses of the same compound.

Due to high correlations between potassium occupancy and vacancy fraction in the Rietveld refinement and the absence of ICP data for this compound, a quantification of the composition is not robust. However, when the amount of K is fixed to the expected amount of one atom per formula unit, a Cr_C : Cr_N

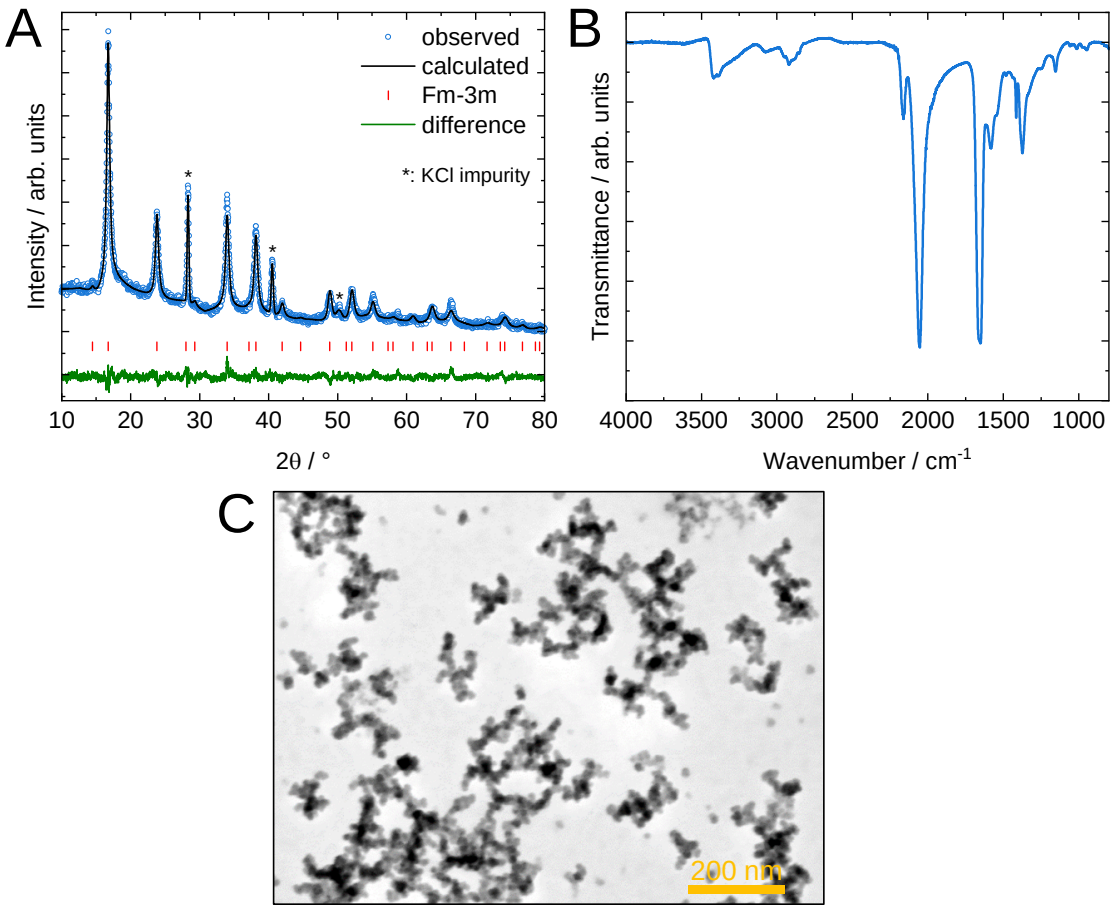


Figure 3.9: Characterisation of $K_{1-x}Cr[Cr]$. The XRD pattern (A) is refined in the $Fm\bar{3}m$ space group. Sharp peaks marked with asterisks are from remaining KCl from synthesis and are fitted with background peak functions. The material's FTIR spectrum (B) shows an intense absorption band at 2053 cm^{-1} and a weak band at 2161 cm^{-1}, indicating a small extent of oxidation. Transmission-mode SEM image (C) of synthesised powder material, showing particle sizes of around 20 nm.

ratio of $1.013 \pm 0.021 : 1$ is found (fit $R_w = 4.91\%$), which is close to the ideal parity for a vacancy-less material. The calculated pattern and its difference to the measured data for fixed K content is shown in fig. 3.9A. Qualitatively, a low vacancy concentration this is directly visible from the small intensity on the (111) peak in the XRD spectrum. The peak broadening indicates a mean particle size of 19 nm, which is in excellent agreement with SEM characterisation (fig. 3.9C) and comparable to the sizes found for the reduced and oxidised materials above.

The material's IR absorption spectrum is shown in fig. 3.9B. In the ν(CN) region, two peaks are found. The small higher-wavenumber peak at 2161 cm^{-1} is close to

the peak found for the fully oxidised Cr[Cr]. The most intense peak of the material is found at 2053 cm^{-1}. Its position agrees well with the higher-wavenumber peak found for the reduced material. The presence and positions of the two peaks show that while most of the material is in the intermediate oxidation state, some Cr_C centres are oxidised to Cr^{III}. This again highlights the extreme air-sensitivity of the material caused by its low oxidation potential. Due to the partial oxidation, charge neutrality dictates that a corresponding amount of K^+ is extracted from the interstices. Therefore, the assumption of stoichiometric K content used above is subject to error and the composition is better described by $K_{1-x}Cr[Cr(CN)_6]$. Again, additional peaks in the wavenumber regions $< 1700\,cm^{-1}$ and between $2800\,cm^{-1}$ and $3500\,cm^{-1}$ indicate the presence of residual NMF solvent.

The results show that it is possible to produce a nanocrystalline, mixed-valence $K_{1-x}Cr[Cr]$ with suppressed vacancies via non-aqueous synthesis in NMF. This compound is a potential alternative to the reduced $Rb_{2-x}Cr[Cr]$ as intermediate in the synthesis of Cr[Cr]. One obvious advantage of the synthesis of the mixed-valence material is the avoidance of the highly toxic simple cyanide by replacement with the widely available $K_3Cr(CN)_6$ complex, which is classified as non-hazardous.

3.6 The oxidation states of chromium hexacyanochromate

There is severe ambiguity concerning the oxidation states of chromium hexacyanochromate materials presented in literature. This encompasses materials synthesised both in the bulk and in electrodeposited thin films. As example, Mallah *et al.* reported that a change in inserting ion species during synthesis of a mixed-valence material lead to the occurrence of a second ν(CN) peak, which was assigned to linkage isomerism.[131] In a different work on thin films by Buschmann *et al.* it is observable that even when electrochemically reduced, the material's IR spectrum consists of two overlapping peaks which was, however, assigned as a single band with large broadening.[67] Such issues regarding the positions and number of peak positions in the IR spectra have caused doubts about the correct interpretation.[295]

A variety of factors lead to the difficulties in establishing a correct assignment of the oxidation states of chromium hexacyanochromate materials from the features in their IR spectrum. First, as mentioned above, the standard technique for the determination of oxidation states, X-ray photoelectron spectroscopy, is not usable for this composition.[67] Second, the material is extremely sensitive to oxidation by air or water in all oxidation states except fully oxidised. As seen in the sections above, even when working in inert atmosphere, partial oxidation caused by small amounts of oxygen or moisture is not to be ruled out. Third, nearly all chromium hexacyanochromate materials have been synthesised in aqueous media. Even though the Cr^{2+} precursor is metastable in the absence of a catalyst, oxidation cannot be dismissed after integration into the PBA material. For these reasons, a set of reference materials with well-defined oxidation states are so far missing.

As one of the most important properties for the understanding of the magnetic and electrochemical behaviour, an in-depth knowledge about the material's oxidation states is crucial. The syntheses presented above can provide these insights. Due to the synthesis of chromium hexacyanochromate in its three oxidation states, its fingerprints can be tested and analysed. Albeit some amount of oxidation is detectable in the reduced and mixed-valence states, the FTIR peaks related to the individual oxidation states are clearly observable. By comparing with computational results on vacancy-free chromium hexacyanochromate by Hurlbutt, the experimental insights are matched with the underlying electronic structure.[220] To compare and explain the results from literature, an additional chromium hexacyanochromate material is synthesised via an aqueous precipitation, following the description by Mallah *et al.*[131]

A photograph of the four materials' appearance is shown in fig. 3.10A. In the case of the vacancy-free materials, the colour changes gradually from black to different shades of brown in higher oxidation states. The material synthesised in aqueous media is light grey, matching the description in literature.[131] Fig. 3.10B shows the FTIR spectra of the materials, zoomed in on the relevant ν(CN) region. Three distinct peak regions are clearly distinguishable in the spectra. The reduced

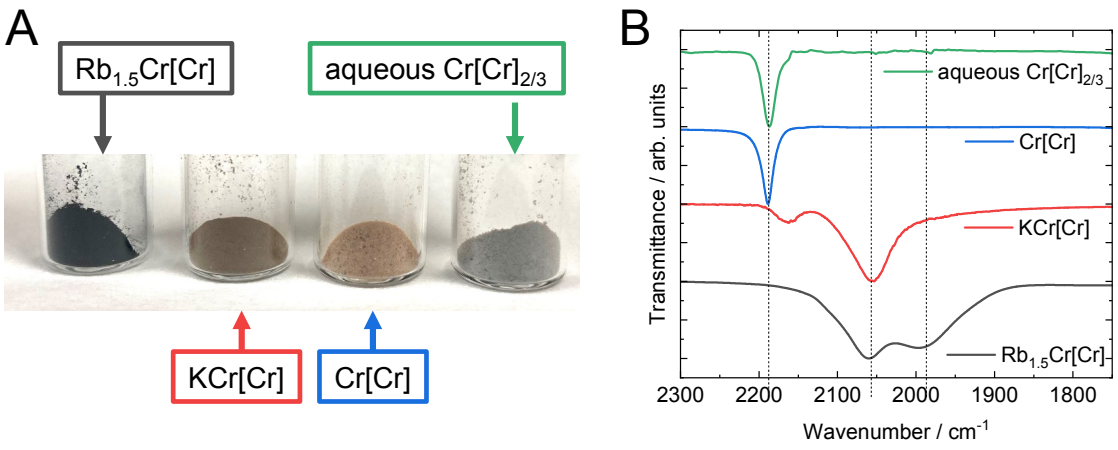


Figure 3.10: Oxidation states of chromium hexacyanochromate. Photographs of the materials synthesised in NMF in three oxidation states as well as the previously reported material synthesised in aqueous media (A). Comparison of the ν(CN) region of the material's IR spectra (B). The appearing peaks can be assigned to the three oxidation states described in the text.

material $Rb_{2-x}Cr[Cr]$ possesses peaks at 1997 cm^{-1} and 2060 cm^{-1}. These positions are in good agreement with the predicted peaks of $Cr^{I}-C\equiv N-Cr^{III}$ stretch of the fully reduced $Rb_2Cr[Cr]$ (1977 cm^{-1}) and $Cr^{II}-C\equiv N-Cr^{III}$ stretch of the mixed-valence RbCr[Cr] material (2065 cm^{-1}).[220] Clearly, the material is in a partly fully reduced, partly intermediate oxidation state. Since the material is synthesised from Cr^{2+}, an electron transfer from Cr_N to Cr_C must have occurred upon formation. The intermediate $K_{1-x}Cr[Cr]$ exhibits two peaks located at 2161 cm^{-1} and 2053 cm^{-1}. Its intense lower-wavenumber peak lines up with the higher-wavenumber peak of the reduced material and therefore indicates the presence of $Cr^{II}-C\equiv N-Cr^{III}$ bonding, as expected for the mixed-valent material. Also in this compound, one electron must have transferred from each Cr_N to Cr_C during formation. The fully oxidised Cr[Cr] possesses only one sharp peak, located at 2186 cm^{-1}. This peak agrees well with the computationally predicted position of 2176 cm^{-1} for $Cr^{III}-C\equiv N-Cr^{III}$ stretching for a fully oxidised material.[220] The position is close to the higher-wavenumber peak of $K_{1-x}Cr[Cr]$. This indicates that the Cr_C in the mixed-valent material are partly oxidised to the Cr^{III} state. Using the three materials, the IR absorption bands of the individual oxidation states can be unambiguously assigned.

The material synthesised from aqueous media exhibits a single peak at 2187 cm^{-1}, which is in agreement with literature.[67, 131, 134, 147, 281, 296, 297] In various works, this peak has been assigned to the $Cr^{II}-C\equiv N-Cr^{III}$ or $Cr^{III}-C\equiv N-Cr^{II}$ stretch frequency of a mixed-valence chromium hexacyanochromate. The comparison to the results of this work clearly show that this assignment is incorrect. As both the peak position and shape matches the IR spectrum of the fully oxidised Cr[Cr], materials reported in literature are fully oxidised. Likely, this is due to a reaction of the material with the aqueous media or oxygen in air. Interestingly, these insights explain the seemingly conflicting magnetic behaviour found in an influential work by Mallah *et al.*[131] The authors reported the synthesis of two mixed-valence chromium hexacyanochromate materials, one high-vacancy material (1) and one cesiated material with a lower-vacancy content (2). The magnetic ordering temperatures found for (2) lies below that for its high-vacancy counterpart (1), which would contradict eqn. 1.10. However, (2) exhibited two peaks in its IR spectrum at 2187 cm^{-1} and 2069 cm^{-1}, whereas (1) only showed one peak at 2194 cm^{-1}. Using the insights gained in the present work, one can conclude that while (1) was fully oxidised, (2) was partly fully oxidised and partly in the intermediate oxidation state, likely due to the inability of Cs^{+} to leave the structure, thus "pinning down" the oxidation state. The stronger magnetic interactions between Cr^{III} species compared to Cr^{II} can explain the higher ordering temperature of (1), despite the higher number of nearest neighbours in (2).

This leaves one question behind: How can a PBA with non-zero vacancy content be fully oxidised? A fully oxidised material with a vacancy content of y possesses $3y$ excessive positive charge per formula unit and is therefore forbidden by the principle of charge neutrality. Anion insertion is one possible mechanism to retain charge-neutrality. However, while the possibility of this mechanism has been speculated,[160, 298–300] no compelling evidence has been presented to date.

3.7 Conclusion

In conclusion, this chapter presents strategies to optimise the synthesis of vacancy-free chromium hexacyanochromate materials in both reduced and fully oxidised valence states. Through an increase in precursor concentrations and synthesis temperature, the absolute yield and particle size are increased considerably, thus allowing for the first time a detailed structural study and quantitative compositional analysis. It is shown that the produced nanoparticular material consists of individual, highly ordered crystallites, which is an important insight for the later study of the oxidised material's magnetism. The analysis confirms the qualitative indications of the materials possessing near-zero vacancy concentrations, which validates the effectiveness of the non-aqueous synthesis in NMF. For the first time, also a non-aqueous synthesis method for the mixed-valence K_{1-x}Cr[Cr] is reported. This offers an alternative synthesis route for Cr[Cr], avoiding the use of the highly toxic simple cyanides.

The presented syntheses of chromium hexacyanochromate materials in three different oxidation states allows for the so far lacking understanding of the IR absorption lines obtained for this materials system. Due to their formation and handling in inert environments, the presented materials act as reference materials offering an unambiguous assignment of spectral lines. Using these insights, literature results can be interpreted, checked and validated. In fact, the results uncover the misconception of the formation of mixed-valence PBA from aqueous media, which was reported in a highly influential publication.[131]

The synthesis of vacancy-less, fully oxidised Cr[Cr] shown in this chapter lays the foundation for a detailed study of its magnetic and electrochemical properties, which is the topic of chapter 4.

3.8 Experimental

KCN and RbCl are weighed out outside the glovebox and dried at 300 °C in vacuum, then transferred into an argon-filled glovebox for synthesis. Anhydrous $CrCl_2$ is

dissolved in 12 mL anhydrous NMF to form a 200 mM solution. KCN and RbCl are dissolved together in 30 mL NMF to form a 240 mM and 160 mM solution, respectively. The two solutions are heated up to 180 °C on a hotplate and kept at this temperature during the reaction. Under vigorous stirring of the KCN and RbCl solution, the $CrCl_2$ solution is added dropwise to the KCN and RbCl solution. After mixing, the reaction liquid is slowly cooled down to room temperature with continued stirring. The reaction liquid is sealed air-tight and centrifuged to collect the precipitate. The precipitate is washed two times with NMF. For the analysis of the reduced material, it is then dried at 75 °C in a vacuum oven. Care is taken not to expose the precursors and synthesised material to air at any stage of the synthesis. To form the oxidised material, it is further processed directly after washing with NMF without drying.

For the chemical oxidation, a 0.1 M solution of HNO_3 in ultrapure water is prepared. The synthesised material is opened to air, right before 60 ml of the dilute nitric acid solution is added to it. The dispersion is heated to 95 °C and stirred at this temperature for at least 10 h. Afterwards, the material is collected by centrifugation, washed two times with ultrapure water and dried at 140 °C in vacuum. The material is not allowed to rehydrate and is handled in the glovebox.

For the synthesis of KCr[Cr] in an argon-filled glovebox, $K_3Cr(CN)_6$ is vacuum-dried at 300 °C and dissolved in 5 mL anhydrous NMF to form a 80 mM solution. Separately, anhydrous $CrCl_2$ is dissolved in 2 mL anhydrous NMF to form a 200 mM solution. The $K_3Cr(CN)_6$ solution is heated to 180 °C, at which temperature the $CrCl_2$ solution is added dropwise. After mixing, the synthesis liquid is left to cool in the glovebox, then sealed and centrifuged outside the glovebox. It is washed twice with anhydrous NMF in the glovebox, then dried in vacuum without air-exposure.

Another material was synthesised from aqueous solutions outside the glovebox, according to Mallah *et al.*[131] A 20 mM solution of $K_3Cr(CN)_6$ in 20 mL argon-saturated H_2O was prepared under argon protection. Also, a 20 mM solution of $CrCl_2$ in 20 mL argon-saturated H_2O was prepared under argon protection. The $CrCl_2$ solution was added dropwise to the $K_3Cr(CN)_6$ solution at 80 °C

under argon protection. The grey precipitate was collected by centrifugation and washed repeatedly with ultrapure water, then dried and stored in a closed vial in ambient atmosphere.

4

Magnetic and electrochemical properties of chromium hexacyanochromate

Contents

4.1 Abstract 93
4.2 Motivation 94
4.3 Magnetic properties 97
4.4 Electrochemical properties 106
4.4.1 K-ion cells 107
4.4.2 Na-ion cells 113
4.5 Conclusion 116
4.6 Experimental 117

4.1 Abstract

Chromium hexacyanochromate has shown great promise as both molecular magnet and anode material in aqueous Na-ion batteries, reaching ordering temperatures up to 270 K,[280] the second highest in PBAs behind vanadium hexacyanochromate,[111] as well as a high ion storage capacity at low potentials.[221] These reported results have all been achieved with vacancy-rich materials. The synthesis and characterisation of vacancy-free Cr[Cr] described in chapter 3 allows for the investigation of the impact of vacancies on the material's magnetic and electro-

chemical properties. The absence of vacancies and coordinated water is expected to improve both the magnetic properties as well as the electrochemical capacity, making the material a candidate air-stable, high-temperature magnet and anode material with a high theoretical ion storage capacity of $206\,\mathrm{mA\,h\,g^{-1}}$.

In this chapter, a thorough study of the Cr[Cr] material's magnetic and electrochemical properties is presented. Results from PND and magnetometry show that while the synthesised material possesses a large and negative Weiss constant, a comparatively low magnetic ordering temperature is found. A particle size effect is identified as likely cause for this finding. Electrochemical studies show that both K^+ and Na^+ ions reversibly insert into the structure. Two low-potential redox processes deliver high capacity of up to $145\,\mathrm{mA\,h\,g^{-1}}$ in the Na^+ electrolyte. The findings presented in this chapter show that through a decrease in vacancy concentration, both the magnetic interactions and ion storage capacity of Cr[Cr] can be increased. Furthermore, the results demonstrate that particle size effects crucially impact the found magnetic ordering temperature, an aspect which has been overlooked in magnetic PBA research so far.

4.2 Motivation

Hexacyanochromate(III)-based PBAs have been studied extensively in the context of molecular magnetic materials. As explained in more detail in the introduction, this is because the Cr^{3+} centre possesses the maximum number of unpaired d-electrons and spin possible for the carbon-coordinated site. This enables strong magnetic exchange interactions to the neighbouring P sites, which lead to the discovery of high magnetic ordering temperatures in these materials. In fact, Cr^{3+} forms the R site of the material with the highest reported ordering temperature of any PBA, $KV^{II}[Cr^{III}]$ with a T_C of 376 K.[111] Because of the incorporated V^{II}, this composition is highly sensitive to oxidation in air. $Cr^{III}[Cr^{III}]$ possesses the isoelectric d^3-d^3 configuration and is air-stable due to the sole presence of oxidised Cr^{3+} species. From the above presented orbital theories, similarly strong exchange interactions are expected. However, some lowering in $|J|$ is predicted because of the less diffuse d-orbitals and

the resulting smaller overlap integral. The achievable ordering temperature of a crystalline and defect-free $Cr^{III}[Cr^{III}]$ is therefore a highly relevant question that has lead to a number of attempts and prominently published works.[131, 280, 282]

The studies published so far are all based on materials with non-zero vacancy concentrations, as can be seen directly from the reported compositions or, where it is not available, from the large saturation magnetisations. In a zero-vacancy $Cr^{III}[Cr^{III}]$, the saturation magnetisation vanishes because of the exact spin compensation. Mallah *et al.* found a T_C of 230 K in a high-vacancy material with composition $Cr[Cr]_{2/3}$.[131] The material's Weiss temperature Θ was -306 K, indicating strong antiferromagnetic interactions, as predicted by orbital theories. Although reported to be in a $Cr^{II}[Cr^{III}]$ oxidation state, the results in the present work show that the material was in fact fully oxidised (see chapter 3). Sato *et al.* achieved a material with similar composition by means of electrodeposition on a tin dioxide substrate.[280] The material exhibited a T_C of 240 K and a Θ of -320 K, both of which are in excellent agreement with the bulk-synthesised material. By changing the electrode potential during electrodeposition, the composition could be changed toward lower vacancy concentrations. By using a slightly higher potential, a composition of $Cr[Cr]_{0.89}$ was achieved. This compound reached a higher magnetic ordering temperature of 270 K and $\Theta = -416$ K.[280] These results are consistent with the theory and highlight the importance of vacancy reduction in achieving high T_Cs. Results by Buschmann *et al.* support these findings, with a $T_C = 260$ K found for a similarly electrodeposited material.[67, 282] It is worth noting that these electrodeposited films exhibit large crystallite sizes in the µm range.[67, 134] Chromium hexacyanochromate possesses one of the highest magnetic ordering temperatures found for PBAs, second only to the room-temperature magnets based on vanadium hexacyanochromate. However, the vacancy-rich materials reported so far cannot answer the question whether Cr[Cr] can in principle be a room-temperature molecular magnet.

Chromium hexacyanochromate also shows great promise for electrochemical energy storage. The high rate capabilities and cycle life found for hexacyanoferrate-

based, high-potential PBAs have fuelled the desire to employ an anode material with matching metrics, which could enable high-rate batteries. Candidate PBA materials can be identified via their respective redox potentials. A study by Scholz and Dostal showed that the formal potentials of hexacyanochromate-based compositions are among the lowest found for PBAs, with potential differences of $\approx -2\,\mathrm{V}$ to the high-potential hexacyanoferrates.[217] Their potentials lie on the lower end of the stability window of aqueous electrolytes and are similar to the lowest plateau found for manganese hexacyanomanganate, which has been studied as possible anode material for aqueous and hybrid electrolytes.[57, 218] Wheeler *et al.* studied the structural and electrochemical properties of $\mathrm{Mn[Cr]_{2/3}}$ as possible anode material for aqueous $\mathrm{Na^+}$ ion batteries. The results confirm a low redox potential, measured at $-0.86\,\mathrm{V}$ *vs* SHE. However, because of the high vacancy content of the electrochemically active $\mathrm{Cr(CN)_6}^{3-}$ and only one redox reaction per formula unit, the material's specific capacity is limited to $62\,\mathrm{mA\,h\,g^{-1}}$.

Substituting the P-site with another electrochemically active species as well as reducing the vacancy content are obvious strategies to achieve higher capacities. However, the choice is limited. Hexacyanochromates of $\mathrm{P{=}Mn^{2+}}$, $\mathrm{Fe^{2+}}$ and $\mathrm{Co^{2+}}$ are unstable because of linkage isomerisation, resulting in chromium hexacyanometallates.[288, 301–303] Due to the same species occupying the P and R sites, chromium hexacyanochromate is a logical candidate as a high-capacity, low-potential PBA. The material undergoes two reversible redox reactions, and the small potential difference between the plateaus makes both practically usable.[220, 221] In early studies, only one redox reaction was observed, likely because of the high vacancy content of the tested materials[217, 304] Only in a later study by Chen *et al.* were two redox reactions found.[221] The individual reactions were assigned to one redox process happening at every Cr site. However, recent DFT results that only $\mathrm{Cr_C}$ undergoes reversible change of oxidation states between $\mathrm{Cr^{I}}$ and $\mathrm{Cr^{III}}$.[220] Even though the reported material was highly vacant, the specific capacity of $108.2\,\mathrm{mA\,h\,g^{-1}}$ is the highest usable low-potential capacity of any reported PBA while retaining the

crystal structure. Higher capacities reported for some PBA compositions stem from a loss of structure at low potentials and are excluded from this discussion.[224]

In both of the discussed applications, vacancy-free, fully oxidised Cr[Cr] is a promising material. As a molecular magnet, the maximisation of the number of nearest neighbours as well as the ideal d^3-d^3 electronic state is expected to result in strong superexchange interactions and high ordering temperatures. Because of the predicted exact spin compensation, the material is expected to be antiferromagnetic. For battery applications, the absence of vacancies as well as the two redox reactions possibly enable a high specific capacity, while at the same time avoiding detrimental side reactions caused by the presence of coordinated solvent molecules.

This chapter presents the magnetic and electrochemical characterisation of the vacancy-free Cr[Cr] synthesised in chapter 3. The material's magnetic properties are studied using a combination of DC magnetometry and neutron diffraction. Electrochemical studies are carried out in non-aqueous K^+ and Na^+ electrolytes, which provide a stable system to assess and qualify the material's properties and its usability for future aqeous battery systems.

4.3 Magnetic properties

The magnetic properties of materials are usually studied via measurements of the magnetisation in dependence on different external stimuli. However, due to their low signals in susceptibility measurements and the similarity of their field-dependent magnetisation curve to paramagnets, interpreting magnetic data for antiferromagnetic systems is prone to misinterpretation.[256, 305] This is especially true for antiferromagnetic nanoparticles, for which size effects lead to additional magnetic phenomena. Early on, Néel predicted that antiferromagnetic particles in the range of few nm can exhibit superparamagnetic behaviour or low ferromagnetism due to the non-compensation of spin centres at the surface, which could overshadow the antiferromagnetic signal in magnitude.[306] In fact, this behaviour was shown experimentally in antiferromagnetic metal oxide nanoparticles and was confirmed to originate from surface effects.[307, 308] To ensure correct interpretation, these

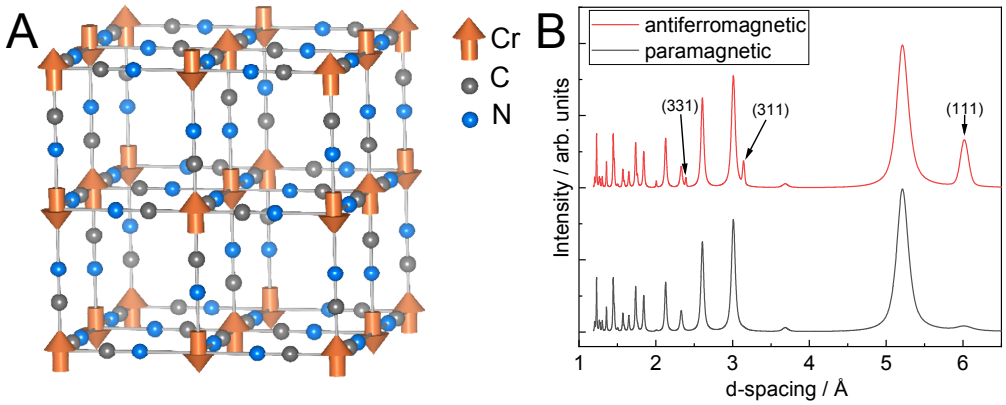


Figure 4.1: Predicted magnetic order in Cr[Cr]. The spin alignment is shown schematically in A, with alternating antiparallel spin orientation between neighbouring spin centres in three dimensions. Predicted neutron diffractograms (B) for the antiferromagnetically ordered case and paramagnetic case. Across the magnetic order-to-disorder transition, the intensities of (111), (311) and (331) peaks is expected to decrease because of the absence of magnetic contributions.

measurements need to be complemented by additional techniques. Neutron diffraction experiments are very well suited to achieve this. The technique directly probes not only the presence of magnetic order, but allows for the determination of spin arrangement and the magnitude of individual magnetic moments through magnetic Rietveld refinement.[230] It is therefore chosen for this work.

The expected spin arrangement in Cr[Cr], based on previous measurements of ferrimagnetic PBAs and structual considerations, is shown in fig. 4.1A. Neighbouring spins arrange in an antiparallel manner, while their orientation within the respective Cr_C and Cr_N sublattices is parallel. The neutrons therefore scatter differently off the two Cr sites, which leads to a change in the diffraction pattern between the ordered and paramagnetic states. Since the sublattices are already structurally distinct due to their respective C and N coordination, no additional magnetic peaks are expected. However, the intensities of the (111), (311) and (331) reflections (among others) are expected to increase significantly in the ordered state, as shown in the predicted neutron diffractograms in fig. 4.1B. From this change, the presence of magnetic order can be determined.

The predictions are tested in PND experiments at variable temperature from 10 K to room temperature. Fig. 4.2 shows the results of these experiments. The

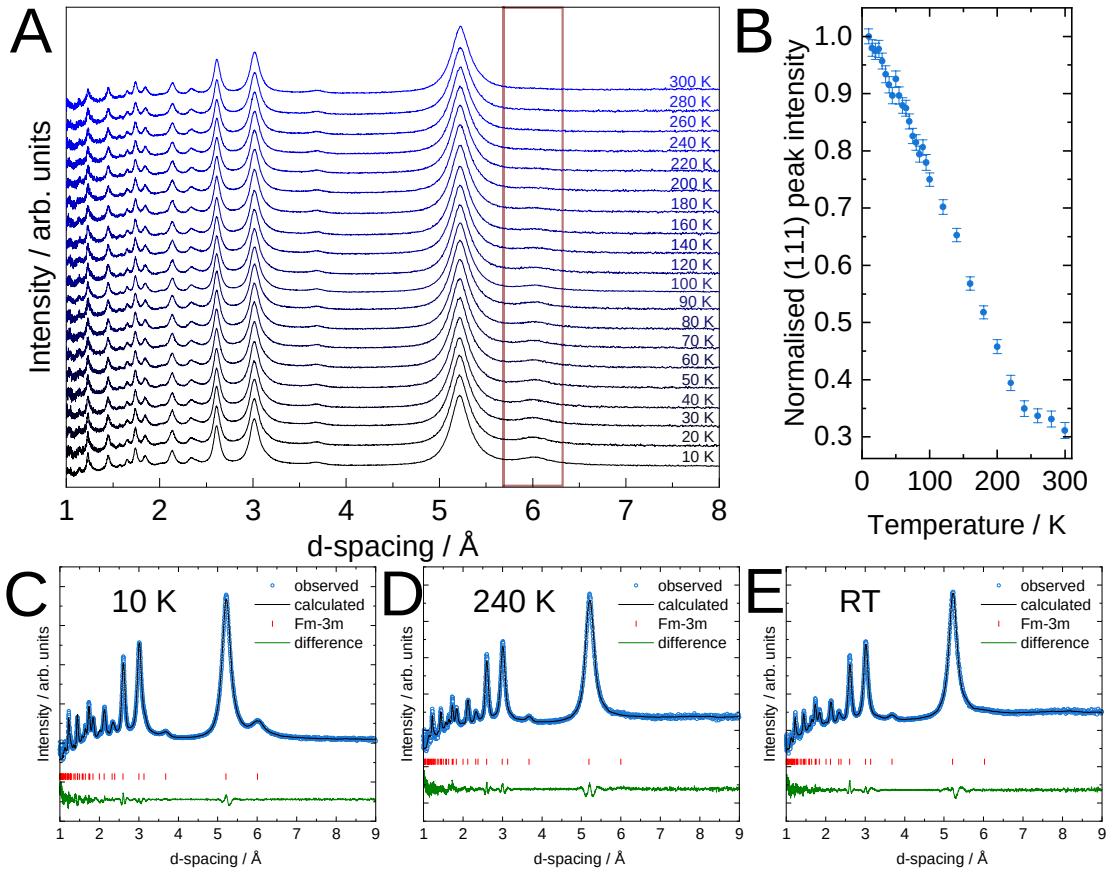


Figure 4.2: Neutron diffraction of Cr[Cr]. Diffraction patterns are measured at temperatures from 10 K to RT. Individual diffractograms (A), showing the temperature-dependence of peak intensities and positions. The red box indicates the position of the (111) peak. The (111) peak intensity is extracted and shown in B. It is clearly observable that the magnetic contribution to the peak vanishes at (240 ± 10) K, indicating the loss of magnetic order. Rietveld-refined diffractograms at 10 K, 240 K and RT are shown in C, D and E, respectively. Data acquired by Dr Pascal Manuel and Dr Dmitry Khalyavin, WISH beamline, ISIS Neutron and Muon Source and analysed by myself.

variations in peak position and intensity with temperature can be seen in fig. 4.2A. The diffractograms show broad diffraction peaks, as is expected for the nanocrystalline material. The most important observation is the change in the intensity of the (111) reflection at a *d*-spacing of 6.01 Å, highlighted by the red box. The peak is well pronounced at low temperatures and decreases with increasing temperature. This change is better visible in fig. 4.2B, which shows the extracted (111) peak height in detail. It is clearly observable that the magnetic contribution to the (111) peak intensity vanishes at (240 ± 10) K. As discussed above, the presence of this contribution indicates magnetic order in the predicted arrangement. The

point of the contribution's disappearance therefore marks the magnetic ordering temperature of the material. The (111) peak is the only peak with a considerable contribution from magnetic diffraction. The absence of other, lower-d magnetic peaks is caused by the typical rapid decay of the magnetic form factor toward lower d, which causes a drastic decay of intensities at smaller interplanar distances. Individual PND diffractograms and their Rietveld fits are shown in fig. 4.2C-E, measured at temperatures of 10 K, 240 K and 36 °C, respectively. At 10 K, a magnetic moment of $(2.78 \pm 0.22)\,\mu_\mathrm{B}$ per Cr centre is refined, which is in excellent agreement with Cr^{III} spin centres in d^3 configuration. The structural parameters obtained from the PND Rietveld refinements agree well with the results obtained from PXRD shown in chapter 3. Summarising the neutron diffraction results, the measurements clearly show that the magnetic order is lost at (240 ± 10) K. It finds an antiferromagnetic spin arrangement with antiparallel alignment between the two Cr^{III} sublattices.

On the basis of the gained insights, the material's magnetism is studied via SQUID magnetometry. The magnetic characterisation is carried out directly on the powder sample located in a plastic capsule which is prepared in an argon-filled glovebox. Before sample introduction into the SQUID magnetometer, the sample is exposed to air for the minimum amount of time needed for loading. Although the material is air-stable, this is to ensure that the material cannot hydrate via uptake of environmental moisture, which could lead to errors in the sample mass. Fig. 4.3A shows the results of DC measurements of the temperature-dependent susceptibility χ under FC and ZFC conditions. Additionally, the FC data is presented in different ways for easier interpretation, both as χT *vs* T (fig. 4.3B) and χ^{-1} *vs* T (fig. 4.3C).

As observed in the χ *vs* T plot shown in fig. 4.3A, the material exhibits a low susceptibility at temperatures > 250 K. Below this temperature, χ increases gradually in both FC and ZFC measurements toward lower temperatures. This increase is indicative of magnetic ordering of uncompensated spins with an ordering temperature of $T_C \approx 250$ K. This value is in good agreement with the magnetic ordering temperature observed in the neutron diffraction measurements and can therefore be assigned to bulk ordering. Although the extent of magnetisation

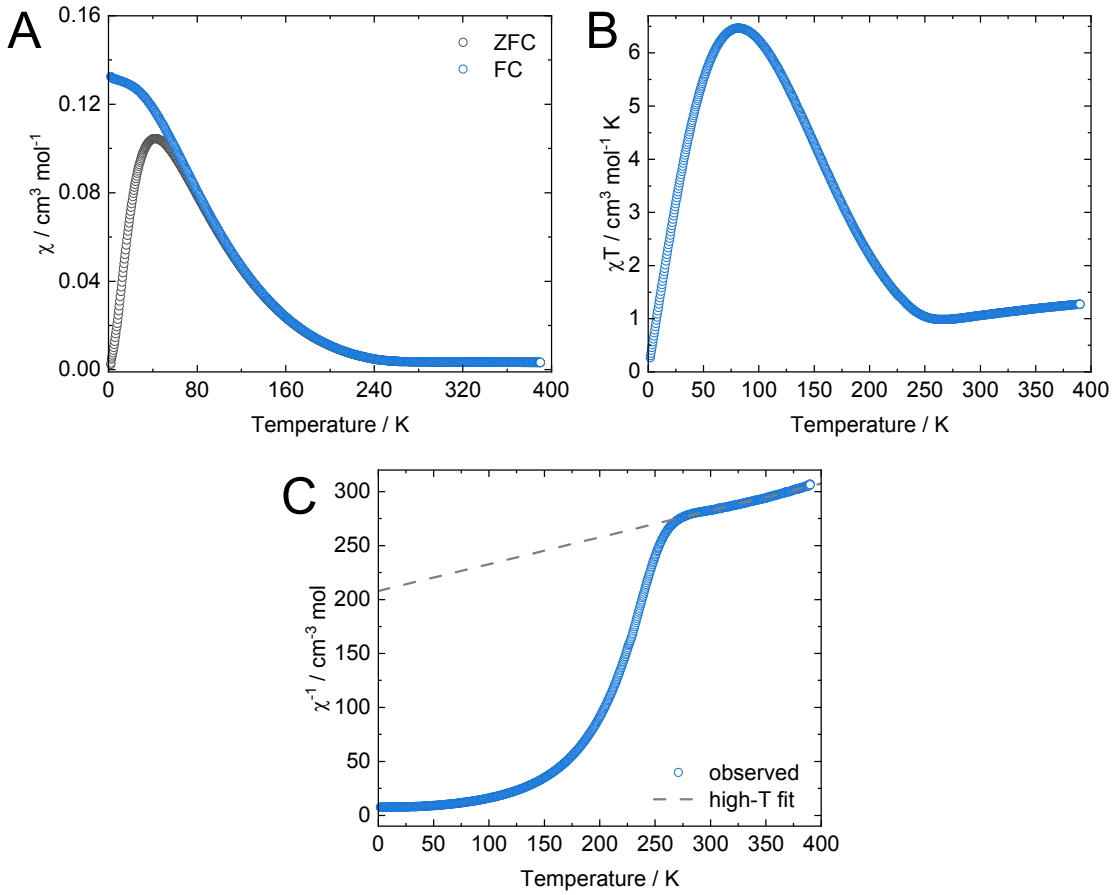


Figure 4.3: Temperature-dependent magnetic susceptibility of Cr[Cr]. The data is represented as χ *vs* T including results form ZFC and FC experiments (A), χT *vs* T (B) and χ^{-1} *vs* T (C). The increase of χ at 240 K towards lower temperatures is indicative of the onset of magnetic ordering with non-compensation. In the χT *vs* T curve, a minimum is found at 265 K, revealing that the ordering is of antiferromagnetic type. In the high-temperature region above 270 K, the data is well described by the Curie-Weiss law, as shown in the χ^{-1} *vs* T curve. Data acquired by Dr Ramón Torres-Cavanillas, Oxford Materials.

found even at low temperatures is orders of magnitude smaller then in reports with vacancy-rich materials, the finding of non-compensated magnetic spin ordering is unexpected for zero-vacancy Cr[Cr]. Susceptibility curves are not ideal to quantify this effect, thus the extent of non-compensation will be analysed later.

In the ordered state, the material's magnetism is heavily influenced by its small particle size. In the temperature-dependent susceptibility plots, a divergence of the ZFC and FC lines at about 70 K is observed, which marks the material's blocking temperature T_B. The divergence indicates that the particles are sufficiently small

to act as individual magnetically ordered domains, giving rise to superparamagnetic behaviour below T_B. The separation appears at a considerably higher temperature than the maximum found in the ZFC susceptibility curve at 42 K, which indicates a broad particle size distribution in the sample.[309] Both of these insights are backed by the characterisation shown in chapter 3, which quantifies a mean crystallite size of 13 nm from XRD data refinement and found individual particles as large as 30 nm via microscopy. Literature studies show that in PBAs of composition CsNi[Cr], the single magnetic domain critical size is up to 22 nm.[310, 311] If the critical size is similar for the present composition, a considerable fraction of particles is indeed expected to behave superparamagnetic.

The material's antiferromagnetic spin alignment is apparent from various characteristics of the measured data. The χT *vs* T curve (fig. 4.3B) exhibits a minimum just above the ordered region, with a value of $\chi T = 0.98\,\mathrm{cm^3\,mol^{-1}\,K}$ found at 265 K. The presence of this minimum is the fingerprint of ferrimagnetic order, that is, antiferromagnetic coupling of uncompensated spins, which is again consistent with above results. Antiferromagnetic interactions are also evident from the high-temperature χT value of $1.3\,\mathrm{cm^3\,mol^{-1}\,K}$ at 390 K, which is significantly smaller than $3.75\,\mathrm{cm^3\,mol^{-1}\,K}$ which would be expected for non-interacting Cr^{III}. The large difference between the two values is a sign of strong antiferromagnetic coupling between neighbouring Cr centres.

To quantify the interaction strength, the susceptibility above 270 K is fitted to the Curie-Weiss law (eqn. 1.7). The fitted line is shown in the χ^{-1} *vs* T plot, fig. 4.3C. The good agreement in the high-temperature region indicates that the data is well described by this level of theory. The fit quantifies a Curie constant C of $(4.02 \pm 0.02)\,\mathrm{cm^3\,mol^{-1}\,K}$ and a Weiss constant Θ of $(-836 \pm 6)\,\mathrm{K}$. The measured C is close to the theoretical spin-only value for two Cr^{3+} centres, $3.75\,\mathrm{cm^3\,mol^{-1}\,K}$,[79] further proving that the nature and oxidation state of spin centres is in fact $Cr_C^{III}-Cr_N^{III}$. The absolute value of the obtained Weiss constant is very large and negative, which reveals remarkably strong antiferromagnetic interactions within the material. The obtained Θ is more negative than for any reported PBA material

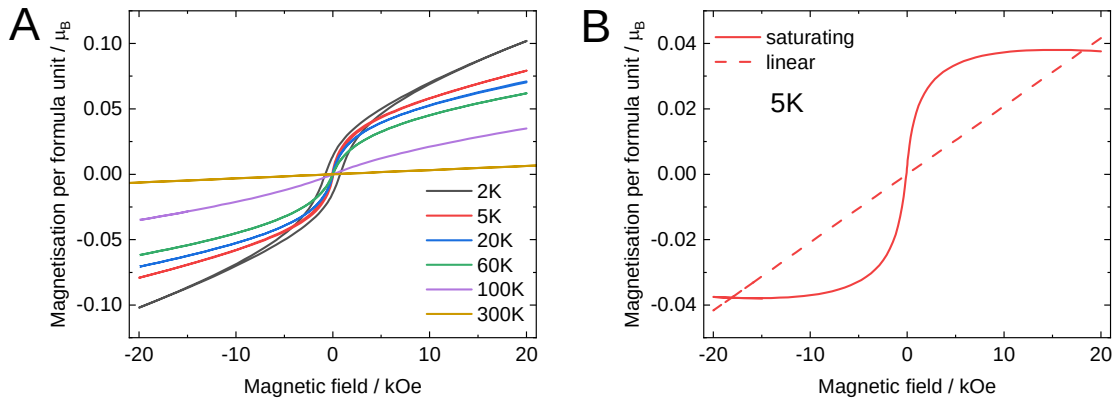


Figure 4.4: Field-dependent magnetisation of Cr[Cr]. Magnetisation curves at different temperatures (A). At 2 K, a hysteresis with $H_C = 772$ Oe and $M_{\mathrm{rem}} = 0.014\,\mu_{\mathrm{B}}$ is observed. At 5 K and above, the hysteresis vanishes. Saturating magnetisation curves are observed until 100 K. At 300 K, the curve resembles a diagonal line. The magnetisation curve at 5 K is deconstructed into its linear and saturating part (B), from which a non-compensation of $0.038\,\mu_{\mathrm{B}}$ per formula unit is determined. Data acquired by Dr Ramón Torres-Cavanillas, Oxford Materials and analysed by myself.

so far, which is consistent with the increased number of nearest neighbours and the pure $d^3 - d^3$ configuration in the present material. For previously reported crystalline chromium hexacyanochromate samples, Weiss constants of −306 K and −416 K were found, which translated into ordering temperatures of 240 K and 270 K.[131, 280] When compared to these compounds, it is surprising that the found ordering temperature is lower, given that higher Weiss temperatures usually indicate higher magnetic ordering temperatures. The reason for this observation is discussed in more detail later in the section.

In order to quantify the amount of non-compensated spins found in the bulk magnetic ordering below 250 K, measurements of the field-dependent magnetisation are carried out at different temperatures. The results are shown in fig. 4.4A. In the temperature range < 250 K, the magnetisation curves show the characteristic S-shape found for the ordering of uncompensated spins. At 2 K, the data reveals a hysteresis loop with a coercive field of 772 Oe and a remnant magnetisation of $0.014\,\mu_{\mathrm{B}}$ per formula unit. The presence of magnetic hysteresis constitutes a collective ordering phenomenon, which likely stems from exchange interactions between adjacent particles. Such behaviour can appear in non-isolated nanoparticles

and is especially pronounced in small particles with a high surface-to-volume ratio.[312] The weak coupling in this collective behaviour is demonstrated by the closure of the hysteresis loop at 5 K. From this temperature on, the magnetisation curve resembles the typical, Langevin-shaped response of superparamagnetic particles.[257] This is consistent with results from temperature-dependent susceptibility measurements. However, the curve does not saturate, as would be expected for an ideal superparamagnet. In order to extract the saturation magnetisation, the curve can be split into two contributions, a linear part and a saturating part. Fig. 4.4B shows the constituents of the deconstructed curve at 5 K. The linear part is the typical response of antiferromagnetic or paramagnetic materials. Since previous results have demonstrated magnetic order at this temperature, the response is ascribed to the antiferromagnetic part of the bulk material. This contribution stems from the fraction of the material in which spins are exactly compensated. The saturating part is attributable to the non-compensated spins. Its saturation magnetisation amounts to $0.038\,\mu_\mathrm{B}$ per formula unit. Possible explanations for this non-compensation are 1.3% $\mathrm{Cr(CN)_6}^{3-}$ vacancies, 3.8% of partly reduced $\mathrm{Cr^{II}}$, surface effects as described by Néel[306] or a mixture of them. Using the techniques employed in this work, the exact origin can, however, not be determined. The small extent of non-ideality further attests to the low vacancy concentration in the material. At higher temperatures, the magnetisation curves flatten before eventually becoming a straight line, as seen at 300 K. This behaviour shows that the material is paramagnetic at this temperature, which is consistent with the obtained magnetic ordering temperature.

The magnetic characterisation confirms the physicochemical characterisation, especially the Cr[Cr] material's oxidation state and suppressed vacancies. Additionally, the measurements validate the expected antiferromagnetic interactions and spin arrangement and reveal very strong exchange interactions. These attributes lead to a highly negative Weiss constant of $(-836 \pm 6)\,\mathrm{K}$, exceeding previously reported values for any PBA composition, to the best of my knowledge. All these favourable metrics point in the direction of a high magnetic ordering temperature.

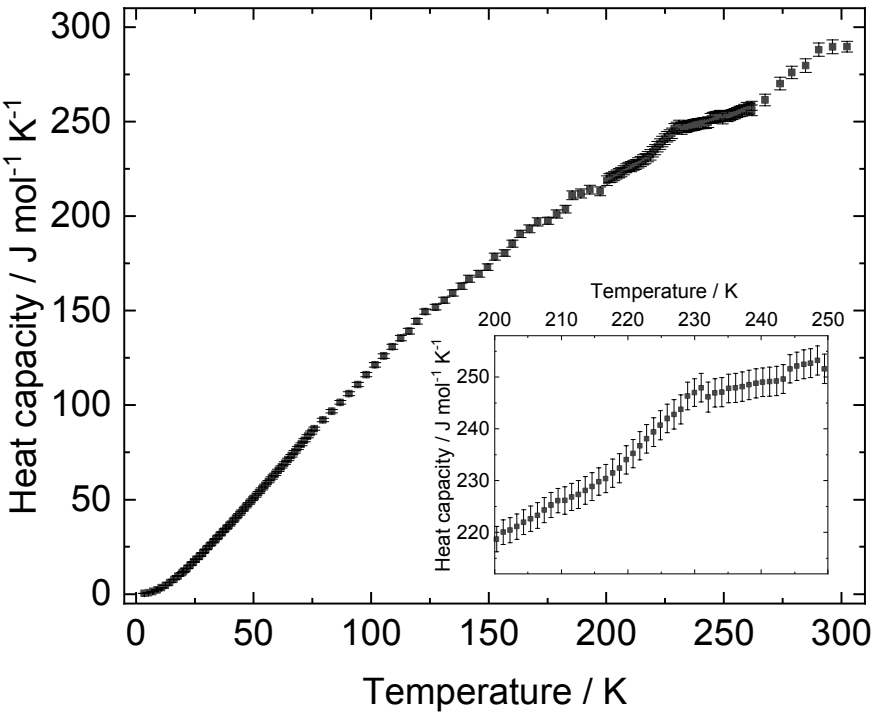


Figure 4.5: Heat capacity of Cr[Cr]. Ill-defined features are visible around 230 K to 250 K (inset), potentially stemming from the onset of magnetic order. Data acquired by Dr Dharmalingam Prabhakaran, Oxford Physics.

However, it is observed that the material's magnetic order is lost at (240 ± 10) K, which is lower than the best attempts reported for this composition and comparable to the value found for a highly vacant material.[131, 280] This raises the question about the cause of the comparatively low T_C.

A closer look at the shape of the magnetic disorder-to-order transition sheds light on the possible explanation. As explained in detail above, the transition is directly visible from changes in the (111) peak intensity in the measured neutron diffractograms (fig. 4.2A and B) and the temperature-dependent susceptibility (fig. 4.3A). In both cases, the transition is not indicated by a sudden jump, but instead increases gradually. A similar behaviour is observed in the material's temperature-dependent heat capacity, shown in fig. 4.5. Between 230 K to 250 K small, ill-defined features are found (see inset). These observations are in stark contrast to the discontinuity expected in the susceptibility and heat capacity for a typical second-order magnetic phase transition.[313] This behaviour hints at different onset temperatures for magnetic ordering in individual Cr[Cr] particles. Such a

phenomenon could explain why the transition is "smeared out" in the observed way. An effect of structural disorder, as observed in other PBA compositions to cause similar behaviour, is unlikely since the particles are well-ordered.[314] However, the wide distribution of particle sizes could lead to the observed soft transitions. This in turn would require a size-dependency of ordering temperatures. In fact, a dramatic lowering in T_C has been observed in other systems when the particle size was lowered to few nm.[315] Considering the small mean particle sizes of the present material and the evidence collected in the presented magnetic characterisation, a size effect is the likely cause for the comparatively low ordering temperature.

4.4 Electrochemical properties

PBAs lend themselves to be used in battery chemistries based on K^+ and Na^+ as insertion species, as elaborated in detail in the introduction. The electrochemical properties are therefore tested in these two systems. Although the comparatively high redox potentials of the material is favourable for the use in future aqueous batteries rather than organic environments, organic electrolytes are chosen to study and assess the material's electrochemical properties. This is done to avoid any electrolyte decomposition reactions which could interfere with measurements at the used potentials. Several experimental aspects need to be decided on before electrochemical measurements.

The first of them is the preparation of electrodes. For this work, the electrode preparation is optimised through testing several different methods and slurry composites. Because of the small particle size, ensuring electrical contact of the entire active material with the current collector is one crucial aspect of the optimisation. Compared to standard, doctor-bladed electrodes on metal foil current collectors, electrodes prepared by dip-casting the composite slurry onto carbon paper current collectors have shown superior performance. This is ascribed to the network of carbon fibres in the paper providing additional channels for electron conduction. Top-view micrographs of the electrode surface are shown in fig. 4.6. The images reveal that the electrode composite coats the individual fibres of the carbon paper.

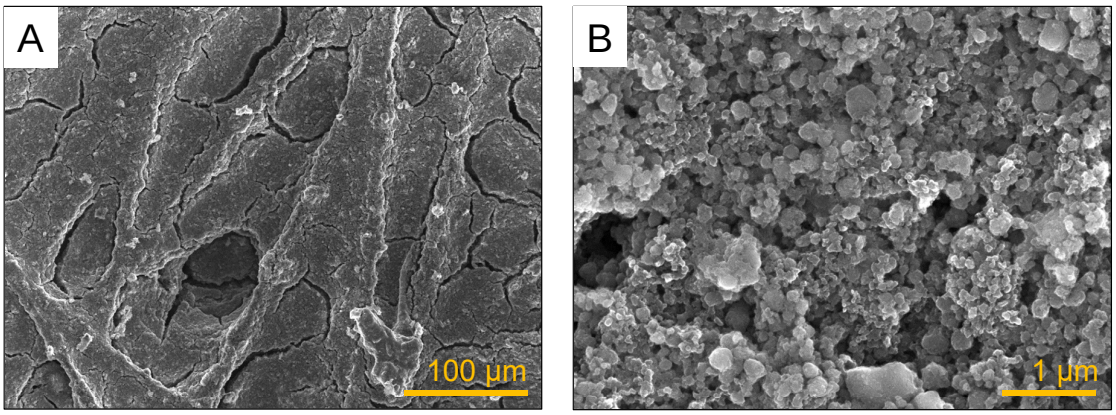


Figure 4.6: Morphology of Cr[Cr] casting on carbon paper. Low-magnification (A) and high-magnification (B) SEM micrographs of the electrode surface. The images show that the electrode composite coats the fibres of the carbon paper current collector. The prepared electrode is highly porous.

Within larger gaps between these fibres, the electrode is highly porous. In the used supported cell, this distribution allows for good electronic contact and electrolyte penetration, which explains the electrodes' favourable performance. The mass loading of active material is $\approx 2\,\mathrm{mg\,cm^{-2}}$. Electrodes prepared in this fashion are used throughout this section. Experimental details are explained in the Methods chapter. Other cell components are standard coin cell components and a glass fibre separator (more details in Methods).

Another choice to be made concerns the used electrolyte. This is dependent on the investigated system and is discussed separately for K^+ and Na^+ cells below.

4.4.1 K-ion cells

For K^+ insertion tests, several standard electrolytes with different chemistries are tested, among them 2.5 M potassium bis(fluorosulfonyl)imide (KFSI) in triethyl phosphate, the ionic liquid-based 1 M KFSI in $Pyr_{1,3}FSI$ as well as the ether-based $2\,\mathrm{mol\,kg^{-1}}$ KFSI in dimethyl ether (DME), all of which have been used successfully in electrochemical PBA research.[58, 61, 316] Out of the tested electrolytes, $2\,\mathrm{mol\,kg^{-1}}$ KFSI DME showed most promise, due to the observation of good wettability, low overpotentials, high capacities and good cycling stability. This is consistent with reports of favourable electrolyte transport properties and stability against potassium

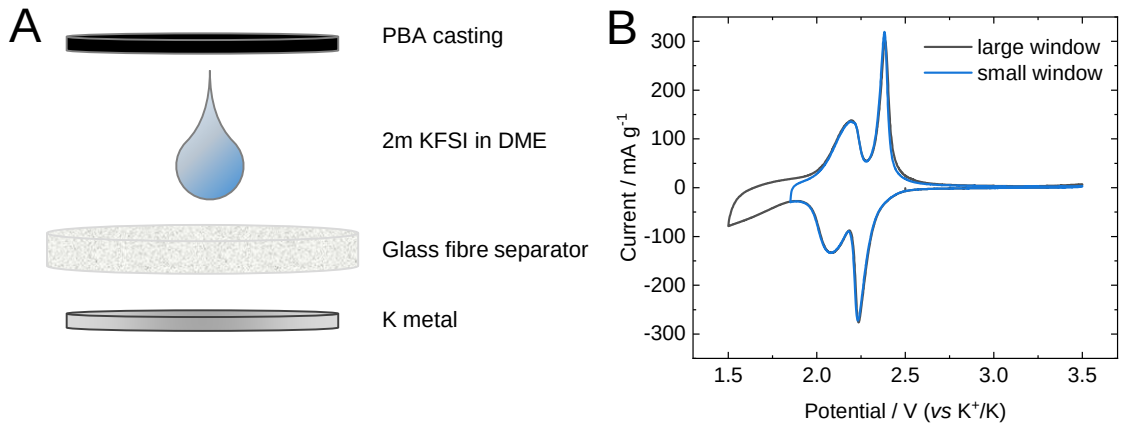


Figure 4.7: Electrochemistry of Cr[Cr] in K^+ electrolyte. Schematic of cell components (A); cyclic voltammogram in extended (grey line) and optimised (blue line) potential window. Below 1.85 V, an irreversible faradaic process is observable.

metal at the CE.[168, 266] Therefore, the performance of the investigated Cr[Cr] in K-ion batteries is tested using this electrolyte. All electrochemical tests are carried out in two-electrode coin cell configuration with excess metallic potassium as CE. The cell components are summarised in fig. 4.7A. Potentials in this section are reported *vs* K^+/K (-2.93 V *vs* SHE).

Fig. 4.7B shows the material's cyclic voltammogram, measured at a scan speed of 0.1 mV s^{-1}. When the potential window is confined between 1.85 V to 2.90 V, two well-resolved reversible redox reactions are observed. The higher-potential process (K-I) has anodic and cathodic peaks at 2.38 V and 2.23 V, respectively and has therefore a $E_{1/2}$ of 2.31 V. the lower-potential reaction (K-II) has anodic and cathodic peaks at 2.19 V and 2.08 V, respectively and its $E_{1/2}$ is 2.14 V. The two reactions can be assigned to the reactions

$$\begin{aligned} \text{(K-I)}\quad & Cr^{III}[Cr^{III}(CN)_6] + K^+ + e^- \longleftrightarrow KCr^{III}[Cr^{II}(CN)_6] \\ \text{(K-II)}\quad & KCr^{III}[Cr^{II}(CN)_6] + K^+ + e^- \longleftrightarrow K_2Cr^{III}[Cr^{I}(CN)_6] \end{aligned} \tag{4.1}$$

based on DFT results.[220] The found potentials are higher than predicted by DFT, which is a well-known shortcoming of the modelling technique and is usually attributable to the neglect of solvation in computational models.[184] As expected, the potentials of the two reversible reactions are among the lowest found for any PBA and are separated by only 170 mV, which makes both reactions utilisable as

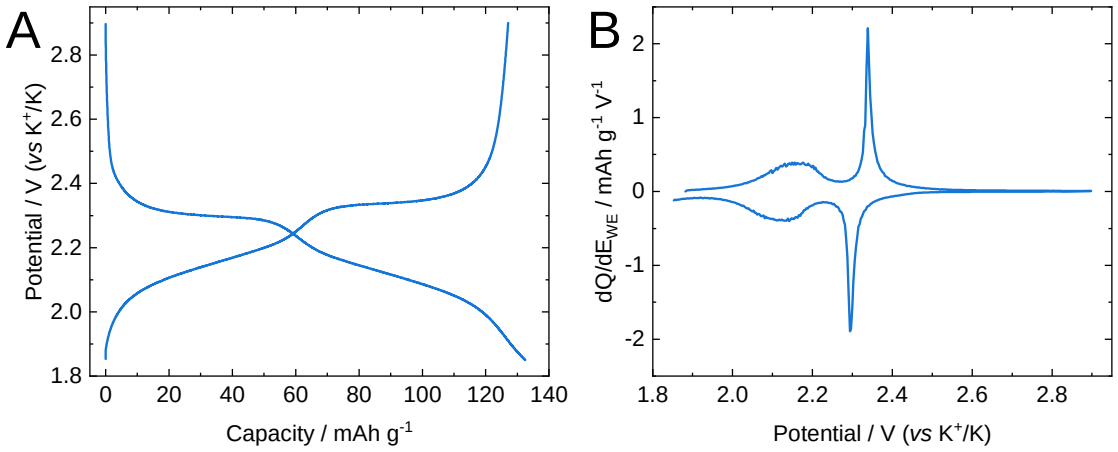


Figure 4.8: Galvanostatic cycling of Cr[Cr] in K^+ electrolyte. Charge and discharge profile (A) and corresponding differential capacity plot (B), measured at a rate of $C/20$. The material delivers a reversible oxidation capacity of $(127 \pm 4)\,\mathrm{mA\,h\,g^{-1}}$. Two redox reactions are distinguishable, centred around 2.15 V and 2.32 V.

anode reactions. These results are encouraging for finding a possible high-capacity electrode material at low potentials.

At potentials below the two reversible reactions, irreversible reactions are visible, as can be seen in the grey line in fig. 4.7B. These irreversible, low-potential processes are consistent with previous reports of reductive loss of PBA structure at low potentials.[60] To stay within the stability window of the PBA structure, 1.85 V is used as lower boundary for electrochemical characterisation. At higher potentials, no additional faradaic processes are found up to 2.90 V. Because no further reversible oxidation reaction is expected above this potential and the stability window of the electrolyte is limited, this potential is chosen as the upper boundary for experiments.

Having established the usable voltage range, the charge and discharge behaviour of Cr[Cr] is studied using galvanostatic cycling. Because of the low potential of the material, it is viewed as possible anode material in aqueous cells. Therefore, it should be noted that the definition of one cycle is the succession of reduction followed by oxidation. This nomenclature is more meaningful, especially in the discussion of coulombic efficiencies. Fig. 4.8 shows the results of cycling experiments at a slow rate of $C/20$. As seen in fig. 4.8A, the material reaches a reversible capacity of $(127 \pm 4)\,\mathrm{mA\,h\,g^{-1}}$ upon reduction and subsequent oxidation. This

value marks the highest reversible oxidation capacity of any low-potential PBA electrode material to date. The capacity stems from the two reversible insertion processes discussed above, which are distinguishable by their two distinct plateaus in the potential *vs* capacity plot.

To investigate the two processes in more detail, the differential capacity dQ/dE_{WE} *vs* potential is shown in fig. 4.8B. From this representation it is observed that the plateaus are centred at 2.15 V and 2.32 V, respectively. Both processes possess a low potential hysteresis of around 40 mV, quantified from the differences in anodic and cathodic peak potentials in the differential capacity plot. The small hysteresis indicates low overpotentials and therefore a high energy efficiency of the cell. High energy efficiencies are characteristic for the low-strain insertion of ions into PBAs.[192, 193]

The different broadening of the found peaks in the differential capacity plot possibly hint at distinct mechanisms of the two reactions. Reaction (K-I) possesses a sharp peak, corresponding to a flat plateau in the potential *vs* capacity plot. Such a behaviour is typical of two-phase reactions. Reaction (K-II), on the other hand, exhibits a slopy potential plateau, resulting in a broad peak in the differential capacity. This behaviour is typical for a single-phase, solid solution-type reaction. If these assignments are true, such behaviour is unexpected. DFT calculations predict that the more severe structural distortions occur in the lower-potential reaction (K-II), whereas in reaction (K-I) the structure remains cubic. These predictions are in accordance with experimental evidence found for low-vacancy PBAs.[27] Accordingly, the expected behaviour should be inverse: a solid-solution type reaction (K-I) and a biphasic reaction (K-II). A structural investigation of the cycled material in different state of charge (SOC) is necessary to find the cause of this discrepancy.

The structural evolution upon cycling is examined by ex-situ XRD at three SOC. Fig. 4.9 shows the diffraction patterns of electrodes stopped at two characteristic points during their fourth reduction and an electrode in pristine, uncycled state. The two potentials are chosen based on their positions on the reduction curve, as shown in fig. 4.9A. The points of interest are located at 2.25 V *vs* K^+/K, where

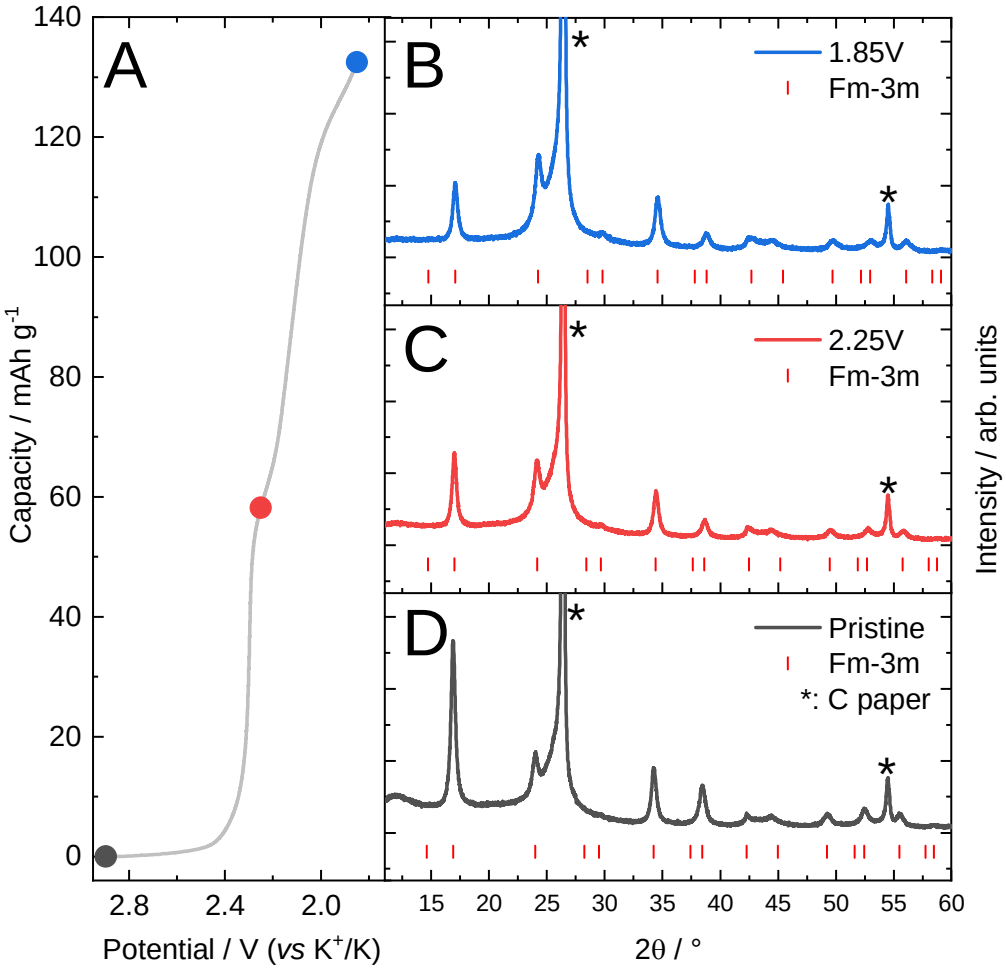


Figure 4.9: Structural analysis of Cr[Cr] upon cycling in K^+ electrolyte. Discharge profile (A), including markers which potentials electrodes are studied ex-situ. XRD patterns of electrodes stopped at1.85 V (B) and 2.25 V (C) and a pristine, uncycled electrode (D). All patterns can be indexed with a cubic $Fm\bar{3}m$ crystal structure. Strong peaks marked with asterisks are signal from the carbon paper current collector.

the electrode has undergone reduction of process (K-I) and is therefore expected to have a composition of $KCr[Cr(CN)_6]$ ($\approx$ 50% SOC), as well as at 1.85 V *vs* K^+/K, after reduction of both (K-I) and (K-II) processes, with an idealised composition of $K_2Cr[Cr(CN)_6]$ ($\approx$ 100% SOC). The corresponding individual XRD patterns are shown in fig. 4.9B-D. Intense Bragg peaks at 26.4° and 54.5° stem from the carbon paper substrate. The results clearly show that the PBA structure remains intact when cycled in the chosen voltage range. Remarkably, the PBA's crystal structure remains cubic and all occurring Bragg peaks of the material can be indexed in the

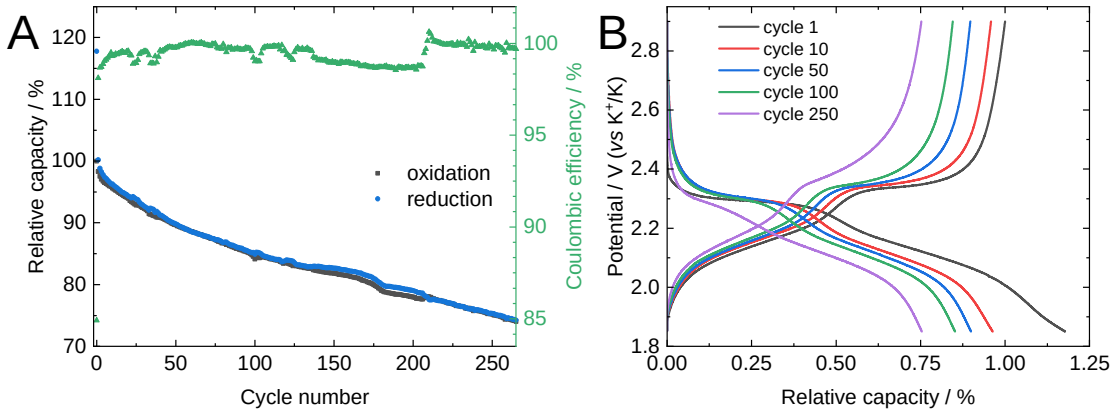


Figure 4.10: Long-term cycling of Cr[Cr] in K^+ electrolyte. Capacity retention and coulombic efficiency *vs* cycle (A) and corresponding (dis)charge profiles (B).

$Fm\bar{3}m$ space group in all oxidation states. Upon reduction, the lattice parameter decreases from 10.45 Å in the pristine state, to 10.41 Å at 2.25 V and 10.36 Å at 1.85 V (uncertainties < 0.01 Å). This decrease in unit cell volume is expected for this material and is discussed in further detail in chapter 3. The observed small structural variation is unlikely to result in phase transition upon cycling, however this needs to be checked with in-situ XRD experiments during cycling in future work.

The cycling stability of Cr[Cr] is assessed in further long-term galvanostatic tests. Fig. 4.10A shows the capacity retention and CE of a cell cycled at $C/20$ for 265 cycles. The material delivers 90% of its initial capacity after 50 cycles, 84% after 100 cycles and 75% after 250 cycles. This metric is remarkable given that the high surface-to-volume ratio of the nanoparticulate material amplifies side-reactions with the electrolyte and thus accelerates material degradation and dissolution. A CE of 85% on the first cycle indicates side reactions upon first reduction of the electrode. In later cycles, these side reactions fade out and higher CEs are found. The corresponding charge and discharge curves are depicted in fig. 4.10B. It is obtainable that the overall redox behaviour remains unchanged throughout the experiment. This is consistent with the structural persistence demonstrated in ex-situ experiments above.

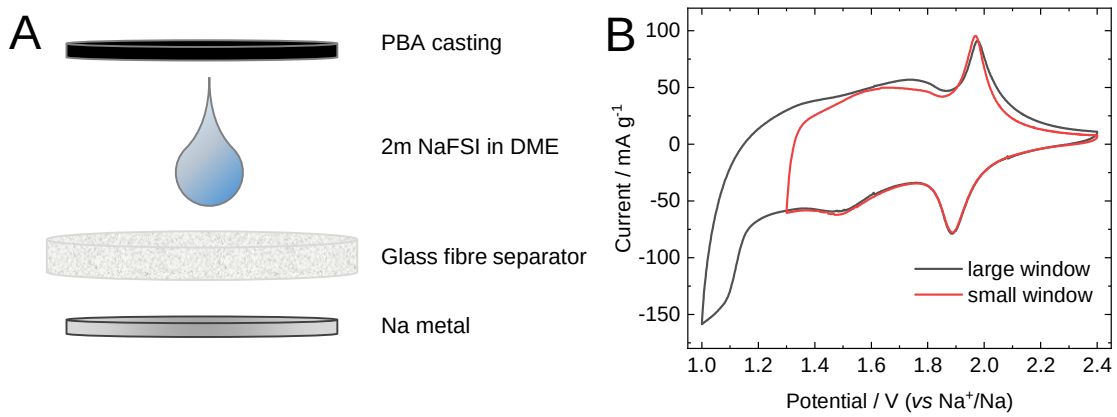


Figure 4.11: Electrochemistry of Cr[Cr] in Na^+ electrolyte. Schematic of cell components (A); cyclic voltammogram in extended (grey line) and optimised (red line) potential window. Below 1.3 V, an irreversible faradaic process is observable. The material's low-potential redox behaviour is poorly separated from the onset of the irreversible reduction process.

4.4.2 Na-ion cells

Based on the successful use of the chosen K^+ electrolyte chemistry, a chemically similar Na^+ electrolyte is an obvious choice for Na-ion battery tests. Therefore, a solution of $2\,\mathrm{mol\,kg^{-1}}$ NaFSI in DME is used, keeping the concentration, salt anion and solvent the same. Analogous to K-ion tests, the experiments described in this section are carried out in two-electrode coin cells with excess Na metal as CE. The cell components are schematically shown in fig. 4.11A. All potentials in this section are reported *vs* the Na^+/Na redox couple (-2.71 V *vs* SHE) unless stated otherwise.

The material's cyclic voltammogram is shown in fig. 4.11B. In the potential window from 1.3 V to 2.4 V, two redox processes are found. The anodic and cathodic current peaks of the higher-potential redox couple are located at 1.97 V and 1.89 V, respectively, leading to a $E_{1/2}$ of 1.93 V. For the lower-potential redox reaction, these are found at 1.64 V and 1.48 V, resulting in $E_{1/2} = 1.56$ V. The two reversible reactions are, analogous to the K^+ case, described by

$$\begin{aligned} \text{(Na-I)}\quad & \mathrm{Cr^{III}[Cr^{III}(CN)_6] + Na^+ + e^- \longleftrightarrow NaCr^{III}[Cr^{II}(CN)_6]} \\ \text{(Na-II)}\quad & \mathrm{NaCr^{III}[Cr^{II}(CN)_6] + Na^+ + e^- \longleftrightarrow Na_2Cr^{III}[Cr^{I}(CN)_6].} \end{aligned} \tag{4.2}$$

The found potentials are close to the oxidation potential found for monovalent manganese in Mn[Mn], currently the lowest-potential reversible redox process in any PBA.[18, 57] A comparison with the potentials found above for K^+ insertion shows

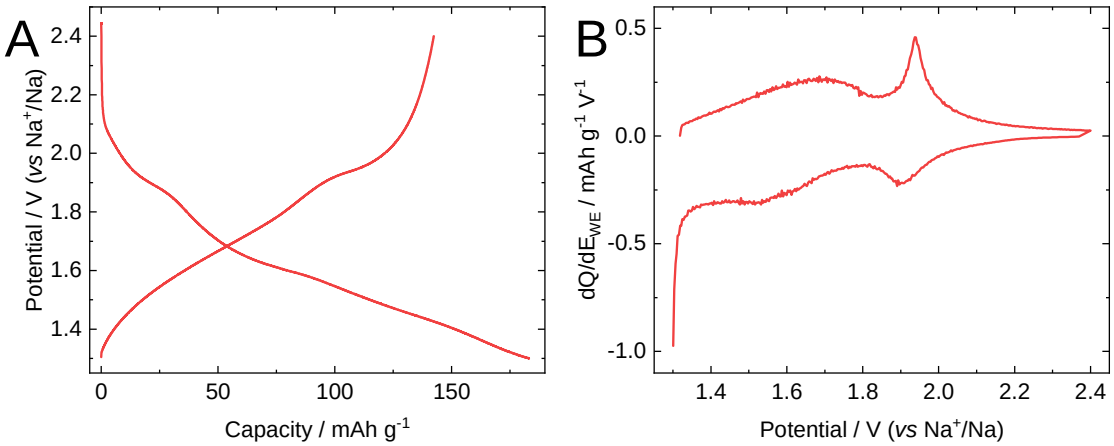


Figure 4.12: Galvanostatic cycling of Cr[Cr] in Na^+ electrolyte. Charge and discharge profile (A) and corresponding differential capacity plot (B), measured at a rate of $C/20$. The material achieves a reversible capacity of $(145 \pm 2)\,\mathrm{mA\,h\,g^{-1}}$. Two redox reactions are distinguishable, centred around 1.6 V and 1.9 V. In the differential capacity plot, the onset of non-reversible reactions below 1.35 V is observable.

that the reactions (Na-I) and (Na-II) are about 160 mV and 360 mV lower than their K-ion counterparts, respectively (accounting for the different reference potentials). This behaviour is well-known for PBA materials and has been explained with the higher energy required to desolvate smaller ions, leading to potentials following the order $Cs^+ > Rb^+ > K^+ > Na^+ > Li^+$ in PBAs.[17, 186, 187, 317]

At lower potentials, the onset of a non-reversible reaction marks the lower end of Cr[Cr]'s electrochemical stability window. An increase in cathodic current is clearly visible around 1.3 V. This onset potential is in good agreement with results found for $Mn[Cr]_{2/3}$, which loses its structural integrity below about 1.4 V.[60] Therefore, the structure loss is likely caused by the instability of the hexacyanochromate complex at these potentials. Due to the reduced redox potentials in the Na^+ insertion reactions, there is no clear separation between the tail of the (Na-II) reduction reaction and the reductive material decomposition reaction. To strike a compromise between high capacity and structural stability, a lower boundary of 1.3 V is chosen for the following experiments.

Fig. 4.12 shows the results from galvanostatic cycling of Cr[Cr] in the non-aqueous Na^+ electrolyte at a rate of $C/20$. The two redox processes are distinguishable via their plateaus in the discharge and charge curve shown in fig. 4.12A and the

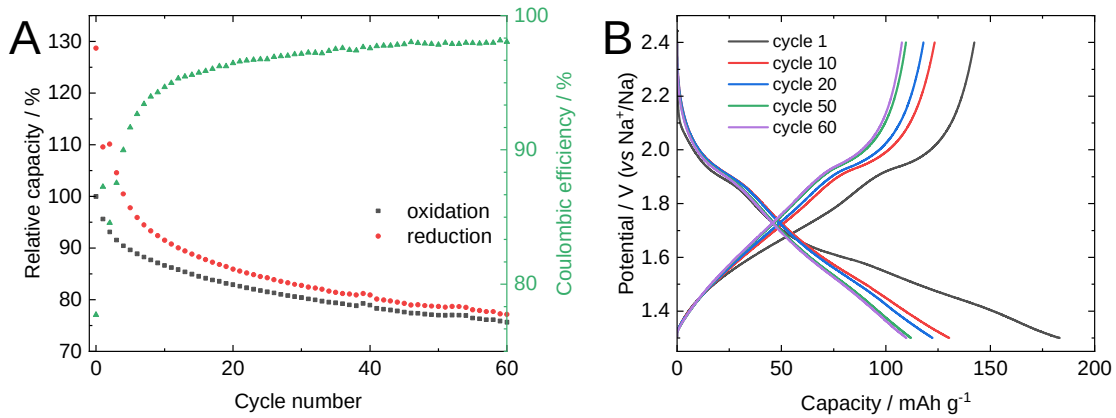


Figure 4.13: Long-term cycling of Cr[Cr] in Na^+ electrolyte. Capacity retention and coulombic efficiency *vs* cycle (A) and corresponding (dis)charge profiles (B).

corresponding differential capacity plot depicted in fig. 4.12B. The material exhibits a high reversible capacity of $(145 \pm 2)\,\mathrm{mA\,h\,g^{-1}}$ for Na-ion storage, similar to the capacity found for K-ions. The two voltage plateaus are centred around 1.6 V and 1.9 V. Again, a low anodic and cathodic peak separation indicates a low voltage hysteresis also for Na^+ ions. Also the peak shapes in the differential capacity behave analogously to the findings for K^+ insertion. The results therefore suggest that the insertion mechanisms are similar. In the differential capacity plot, the onset of material decomposition is leads to a sharp increase in cathodic current below 1.35 V. This process is more pronounced in the galvanostatic experiments since the decomposition reaction contributes additional charge, thus extending the time before the lower cutoff is reached, while in CV experiments, all potentials are scanned at a constant rate.

Fig. 4.13A shows the results of long-term cycling of Cr[Cr] in the Na^+ electrolyte at a rate of $C/20$. The material retains 77% of its initial charge capacity after 50 cycles. Compared to its performance in the tested K^+ electrolyte, the material's capacity fades considerably faster. In the initial cycle, a CE of 78% indicates severe side reactions upon electrode reduction. In contrast to the results for K^+ insertion, these side reactions stabilise slower, which leads to CEs $< 95\%$ in the first 11 cycles and $< 99\%$ throughout all available 60 cycles. These results reflect the lower redox potentials of (Na-I) and (Na-II) compared to their K-counterparts,

which cause instability of the Cr[Cr] material. Corresponding cycling curves are shown in 4.13B. The overall redox characteristics of the material are preserved throughout the experiment. No clear separation between the (Na-II) reduction reaction and material decomposition is observed.

4.5 Conclusion

This chapter investigates the magnetic and electrochemical properties of the vacancy-free Cr[Cr] material synthesised in chapter 3. Using a thorough magnetic characterisation using neutron scattering, magnetometry and heat capacity measurements, the nature of the material's magnetic behaviour is unravelled. The results show that the material is antiferromagnetically ordered below a magnetic ordering temperature of $(240 \pm 10)\,\mathrm{K}$. The arrangement of neighbouring spins follows an antiparallel pattern, consistent with reports on other PBAs. A slight non-compensation of $0.038\,\mu_\mathrm{B}$ per formula is detected, leading to ferrimagnetic particles below the ordering temperature. Because of the small size and single-crystallite nature of the nanoparticles, the material behaves superparamagnetic. The analysis proves the presence of very strong antiferromagnetic interactions, with a Weiss constant exceeding any other reported PBA. The finding of a comparatively low ordering temperature despite the strong interactions is likely caused by a particle size effect.

The electrochemical characterisation shows that Cr[Cr] is a high-capacity electrode material for K^+ and Na^+ ion batteries with one of the lowest potentials found in PBAs. Its reversible capacity in K^+ and Na^+ electrolytes is $127\,\mathrm{mA\,h\,g^{-1}}$ and $145\,\mathrm{mA\,h\,g^{-1}}$, respectively. Since both of the redox potentials are in close vicinity, the material offers the highest usable capacity at low potentials of any PBA material reported to date. Despite the small particle size, the material is able to cycle stably, delivering 75% of its initial capacity after 250 cycles in K-ion cells. Compared to leading anodes for high-energy density cells with organic electrolytes, the found redox potentials are too high to be practically used in these systems. Instead, the redox potentials are close to the lower boundary of the stability window of

highly concentrated aqueous electrolytes, making the material a possible anode material in aqueous NIBs and KIBs.

The results presented in this chapter suggest that future work should be dedicated to a further increase in particle size, for example via slow interdiffusion synthesis or microfluidic mixing to stay below the supersaturation point and thus allow for a growth-dominated crystallisation.[318, 319] In the realm of molecular magnetism, this could unlock the study of true bulk magnetic ordering of Cr[Cr] and enable finding the material's ordering temperature unrestrained by surface effects. For the study of the electrochemical properties, this would allow for better electrical contact and avoid disconnected active material particles, which are the likely cause for achieving only 70% of the material's theoretical capacity in this work. The results show that Cr[Cr] could be a promising anode material for aqueous NIBs and KIBs, which should be further investigated through electrochemical tests in water-in-salt electrolytes.

4.6 Experimental

To achieve the large sample size needed for neutron diffraction experiments, the synthesis described in chapter 3 is upscaled to a total reaction volume of 140 mL at constant precursor concentrations. The oxidising solution is scaled accordingly.

For electrochemical tests, 35 mg of the synthesised PBA is mixed with 10 mg of carbon black and 5 mg PVDF binder in NMP to form a slurry with 7:2:1 ratio. The slurry is dip-cast onto pre-weighed carbon paper disks and allowed to dry in air to evaporate the NMP. Afterwards, the electrodes are dehydrated by drying in vacuum at 80 °C and transferred without air-exposure for storage into an argon-filled glovebox before use. The used electrolytes are prepared in an argon-filled glovebox. The used anhydrous DME (Sigma-Aldrich) is further dried over 3 Å molecular sieves. Before use, the solvent is filtered using dried 0.2 µm pore-size PTFE syringe filters to remove any solid residue from the molecular sieves. The KFSI and NaFSI electrolyte salts are purchased from Solvionic and dried at 100 °C before use.

5

Non-aqueous synthesis of transition metal hexacyanoferrates

Contents

5.1 Abstract 118
5.2 Motivation 119
5.3 Reduced-state materials 121
5.4 Mixed-valence materials 122
5.5 Conclusion 130
5.6 Experimental 131

5.1 Abstract

Chapter 3 demonstrates that a non-aqueous synthesis route is capable of forming vacancy- and water-free PBA materials. These two attributes are highly advantageous, particularly for materials used in electrochemical energy storage applications, as they allow for maximum storage capacity and the avoidance of detrimental side reactions. This approach, if it could be extended to the synthesis of other PBA compositions, could be used to achieve a range of materials that share these advantageous properties. In this context, transition metal hexacyanoferrates are especially relevant, since these materials represent some of the most promising

cathode materials in Na- and K-ion batteries. Although the synthesis of these materials has been the subject of numerous studies, some compositions are still elusive or even unobtainable to date. This includes the fully reduced Prussian White, $K_2Fe[Fe]$, which is prone to oxidation, and vacancy-free mixed-valence materials. In this chapter, the universality of the non-aqueous synthesis method presented in chapter 3 is assessed, using transition metal hexacyanoferrates as a test system. While the strategy is not suitable for the formation of reduced-state transition metal hexacyanoferrates, a range of mixed-valence materials are successfully synthesised in their vacancy-free state. Furthermore, the range of analysed materials allows for a closer study of the solvent-mediated vacancy suppression effect and its dependence on unit cell dimension. The gained insights support that the origin of this effect is steric hindrance of solvent molecules in the PBA structure. The presented results widen the understanding of how reaction media influence the structure of synthesised materials and provide a viable way to obtain vacancy-free mixed-valence PBAs.

5.2 Motivation

The vast majority of PBA research has been dedicated to hexacyanoferrate-based compositions, $A_xR[Fe]$ with different transition metals R. This can be attributed not only to the abundance and availability of precursors, as well as the ease of synthesis, but also in large parts due to their relevance as battery materials. Exhibiting high capacities and potentials, hexacyanoferrates are among the leading candidates for cathode active materials in Na- and K-ion batteries. This is especially true for the well-studied materials $A_2Mn[Fe]$ and the commercialised $A_2Fe[Fe]$.[72, 164, 320] The presence of vacancies and associated water molecules in the PBA structure are the two major impediments for their application in batteries. The detrimental impact of these structural and chemical features causes a lower achievable capacity and side reactions due to the limited electrochemical stability of water. This leads to a loss of performance and increased degradation.[214]

There have been many attempts to address this long-standing, fundamental allenge for PBAs by identifying approaches that reduce vacancies. Syntheses from

chelated transition metal ions, *e.g.* using the citrate anion, work well for many compositions in the fully reduced R^{II}/Fe^{II} oxidation state. For PBAs in the mixed-valence oxidation state, however, these strategies have proven unsuccessful.[59, 321] Instead, the use of larger inserting ions such as Rb^+ and Cs^+ has shown to reduce vacancies.[322] In battery applications, however, the nature of inserting ions is not variable but defined by the used charge carrier. In the case of Na^+ and K^+ as inserting species, no viable way to control vacancies is presently available. Thus, fundamental studies of vacancy-free, mixed-valent PBAs are currently hindered.

Another challenge in the synthesis of hexacyanoferrates concerns particularly the formation of Prussian White, $A_2Fe[Fe]$, one of the most promising PBA cathode materials. The material oxidises in aqueous environments,[201] which is accompanied by the loss of inserted cations. Since the fully inserted state is desirable for battery applications, this detrimental process must be avoided. Mitigating strategies proposed thus far involve the use of reducing agents during or after precipitation[204, 323, 324] or single-iron source syntheses[70, 201] which create highly toxic free cyanide.

The non-aqueous synthesis described in chapter 3 demonstrates promise for solving these problems intrinsically by forming vacancy- and water-free PBA materials, as demonstrated for different oxidation states of Cr[Cr]. The universality of the synthetic approach must, however, still be assessed by extension to other PBA compositions. As suggested in earlier work by Wheeler, the success of the non-aqueous synthesis in suppressing vacancies relies on the inability of solvent molecules to enter the PBA structure.[273] Therefore, it is unclear if the same effect can be achieved in materials with different unit cell sizes, especially those exhibiting larger unit cells.

This chapter explores the universality of the non-aqueous synthesis used in chapter 3 for other PBA compositions. The study is carried out using fully reduced and mixed-valence hexacyanoferrate-based PBAs as test system. These materials are well known (synthesised from aqueous media) and highly relevant for battery applications, making them a suitable choice. Additionally, they exhibit a large

variety of unit cell parameters, which allows for a fundamental study of the vacancy-suppressing effect of the chosen solvent.

5.3 Reduced-state materials

As a first step, the solubility of precursor salts must be tested. For this study, the relevant compounds are chlorides of the first-row transition metals, as well as $Fe(CN)_6^{4-}$ and $Fe(CN)_6^{3-}$ salts. Apart from $FeCl_2$ and the oxidation-sensitive VCl_2 and $CrCl_2$, which are purchased anhydrous, the tested salts are purchased with various degrees of hydration. For the work in this chapter, the salts are dehydrated in vacuum at 100 °C and subsequently stored in an argon-filled glovebox. For each salt, a small amount is added to NMF and the solubility is qualitatively assessed by eye (see table 5.1). Of the hexacyanoferrate salts, none of the available reduced $Na_4Fe(CN)_6$ and $K_4Fe(CN)_6$ salts dissolve in NMF in practical quantities. In contrast, $K_3Fe(CN)_6$ is soluble and forms a clear, yellow solution.

Salt	VCl_2	$CrCl_2$	$MnCl_2$	$FeCl_2$	$CoCl_2$	$NiCl_2$	$CuCl_2$
Solubility	No	Yes	Yes	Yes	Yes	Yes	Yes

Table 5.1: Solubility of transition metal salts in NMF.

The insolubility of ferrocyanide salts obviously impedes the synthesis of reduced-state PBA materials. There is, however, the possibility to form the hexacyanoferrate complex as an intermediate in a synthesis from simple cyanide, as demonstrated in chapter 3 for $Rb_{2-x}Cr[Cr]$. The proposed reaction could follow the idealised formula

$$2\,Fe^{2+} + 6\,CN^- + 2\,A^+ \longrightarrow A_2Fe[Fe(CN)_6]. \tag{5.1}$$

If the intermediate $Fe(CN)_6^{4-}$ complex stays in solution long enough to be polymerised, PBA formation could be possible. Due to the ability of Fe^{2+} to occupy both the P and R sites in the PBA structure, the insertion of this species cannot be restricted to only one of the sites. Therefore, this synthesis attempt is only practical for Prussian White, $A_2Fe[Fe]$.

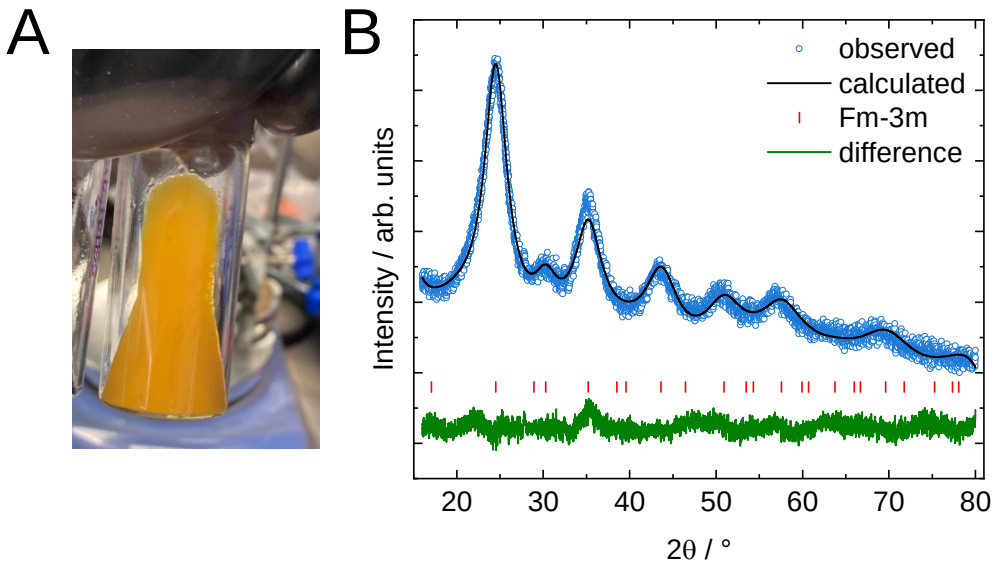


Figure 5.1: Attempted synthesis of $Rb_2Fe[Fe]$. Colour of precipitate after collection (A); XRD pattern with refinement in the $Fm\bar{3}m$ space group (B). Severe peak broadening is observed, indicating low crystallinity.

Experimentally, the test is carried out with stoichiometric amounts of Fe^{2+} and CN^-, in the presence of excessive Rb^+ to provide favourable inserting ions. Upon dropwise addition of the Fe^{2+} solution to the CN^- and Rb^+ solution, an orange precipitate forms (fig. 5.1A). The stark difference in colour to the expected white material indicates that the synthesis fails to form the desired product. The precipitate is analysed using XRD, shown in fig. 5.1B. While the observed peaks can be indexed with the $Fm\bar{3}m$ space group ($a = 10.04$ Å, $R_w = 1.72\%$), the precipitate exhibits very broad peaks, indicating a low crystallinity. These results suggest that the intermediate $Fe(CN)_6{}^{4-}$ complex does not stay in solution long enough to form an extended crystal lattice. NMF is therefore not a suitable medium for the formation of reduced state hexacyanoferrate-based PBAs.

While the $Fe(CN)_6{}^{4-}$ anion is insoluble, the solubility of the ferricyanide salt shows promise for the formation of mixed-valence materials.

5.4 Mixed-valence materials

Syntheses are attempted using the combination of the soluble $K_3Fe(CN)_6$ with the individual soluble transition metal salts shown in table 5.1. Table 5.2 indicates if

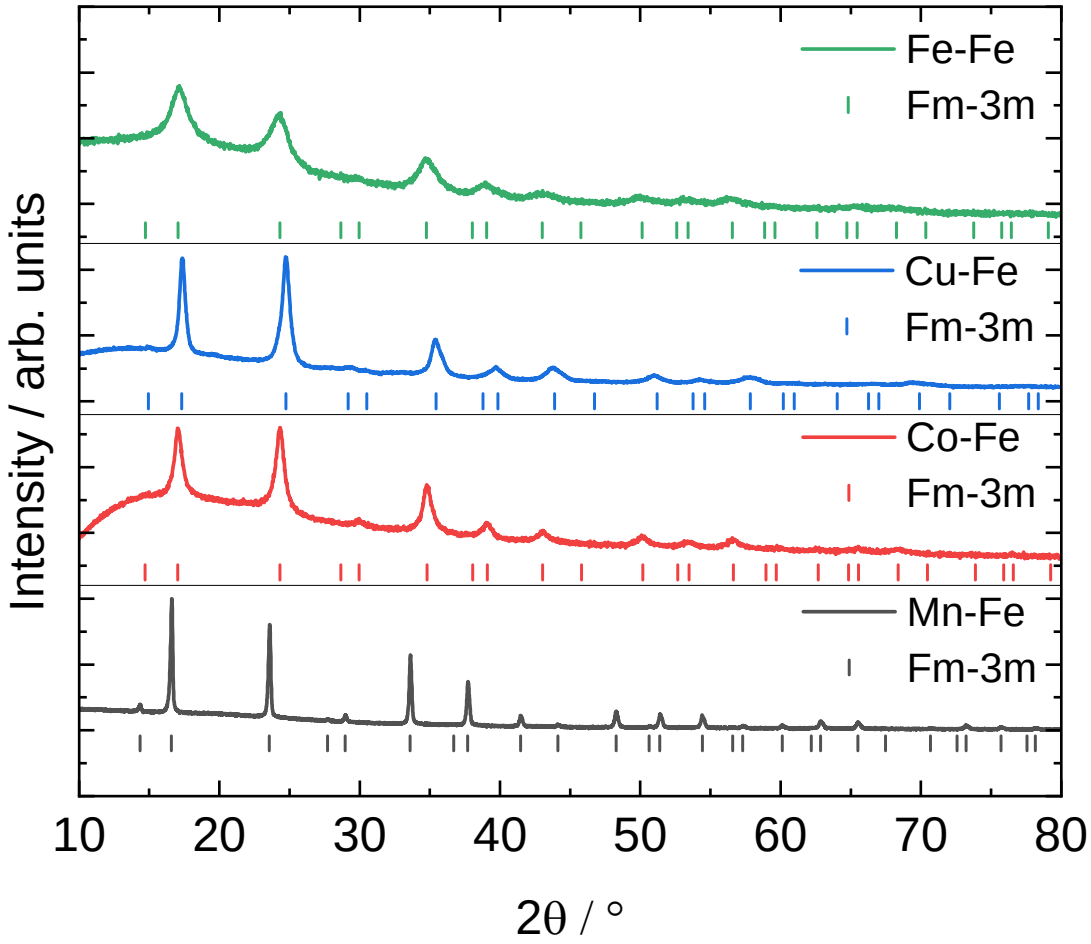


Figure 5.2: XRD patterns of mixed-valence transition metal hexacyanoferrates. All materials can be indexed in the cubic $Fm\bar{3}m$ space group. In all materials but manganese hexacyanoferrate, strong peak broadening is observed. Compared to the other compositions, the (111) peak intensity at 14.5° of manganese hexacyanoferrate is increased.

a precipitate is obtained upon mixing the two respective solutions.

$K_3Fe(CN)_6$ +	$CrCl_2$	$MnCl_2$	$FeCl_2$	$CoCl_2$	$NiCl_2$	$CuCl_2$
Precipitate	*a*	*c*	*c*	*c*	None	*c*

Table 5.2: Summary of attempted syntheses of mixed-valence hexacyanoferrate-based PBA materials in NMF. *a* indicates the formation of an amorphous precipitate, *c* a crystalline precipitate.

A crystalline precipitate forms in all attempted syntheses, except with $NiCl_2$ and $CrCl_2$. The precipitation reaction is expected to follow the formula

$$\begin{aligned} P^{2+} + Fe(CN)_6{}^{3-} + K^+ &\longrightarrow KP[Fe(CN)_6] \text{ or} \\ P^{2+} + \frac{2}{3}\,Fe(CN)_6{}^{3-} &\longrightarrow P[Fe(CN)_6]_{2/3} \end{aligned} \tag{5.2}$$

depending on the success or failure of the vacancy suppressing effect of NMF in the syntheses of the respective composition. The materials' XRD patterns are depicted in fig. 5.2. All materials can be indexed in the prototypical cubic $Fm\bar{3}m$ space group, demonstrating that the formed precipitates are in fact PBAs. The Bragg peaks of the $K_xCo[Fe]_y$, $K_xCu[Fe]_y$ and $K_xFe[Fe]_y$ materials are substantially broadened, which is an effect of their small particle sizes. In the XRD patterns of these materials, the intensity of the (111) peak is very small, which hints at a low vacancy concentration.[322] The diffractogram of $K_xMn[Fe]_y$, on the other hand, shows very different characteristics. Firstly, it exhibits much sharper Bragg peaks, which indicates the formation of larger crystallites. Secondly, its comparatively high (111) peak intensity at 14.5° signifies the presence of vacancies. The lattice parameter and mean particle sizes are extracted from the XRD data for all compositions. The obtained results are summarised in table 5.3. The lattice parameters of $K_xCo[Fe]_y$, $K_xCu[Fe]_y$ and $K_xFe[Fe]_y$ are in good agreement with literature.[2, 33, 59, 126, 193, 214, 322, 325–327] The lattice of the synthesised $K_xMn[Fe]_y$ is expanded in comparison to previous reports, as will be discussed below.[214, 223, 328] Due to the substantial peak broadening, a quantification of occupancies is not attempted via Rietveld refinement and instead measured via chemical analysis, as described below.

Material	$K_xMn[Fe]_y$	$K_xCo[Fe]_y$	$K_xCu[Fe]_y$	$K_xFe[Fe]_y$
Lattice parameter / Å	10.6456(2)	10.223(1)	10.021(2)	10.245(3)
Mean crystallite size / nm	73.2	14.7	22.6	5.9

Table 5.3: Parameters from structural analysis of mixed-valence materials synthesised in NMF.

The infrared spectra of the materials $K_xCo[Fe]_y$, $K_xCu[Fe]_y$ and $K_xFe[Fe]_y$ show a single absorption band in the ν(CN) region, located at 2078 cm^{-1}, 2071 cm^{-1} and 2052 cm^{-1}, respectively (see fig. 5.3A). The IR absorption peak of $K_xFe[Fe]_y$ agrees well with reported data for PB.[329] The peaks of $K_xCo[Fe]_y$, $K_xCu[Fe]_y$, however, appear at lower wavenumbers than reported for $Fe^{III}-C\equiv N-Co^{II}$ and $Fe^{III}-C\equiv N-Cu^{II}$.[33, 147, 322] Instead, the positions match with reported frequencies for the charge-inverted $Fe^{II}-C\equiv N-Co^{III}$ and $Fe^{II}-C\equiv N-Cu^{III}$.[126, 325] As

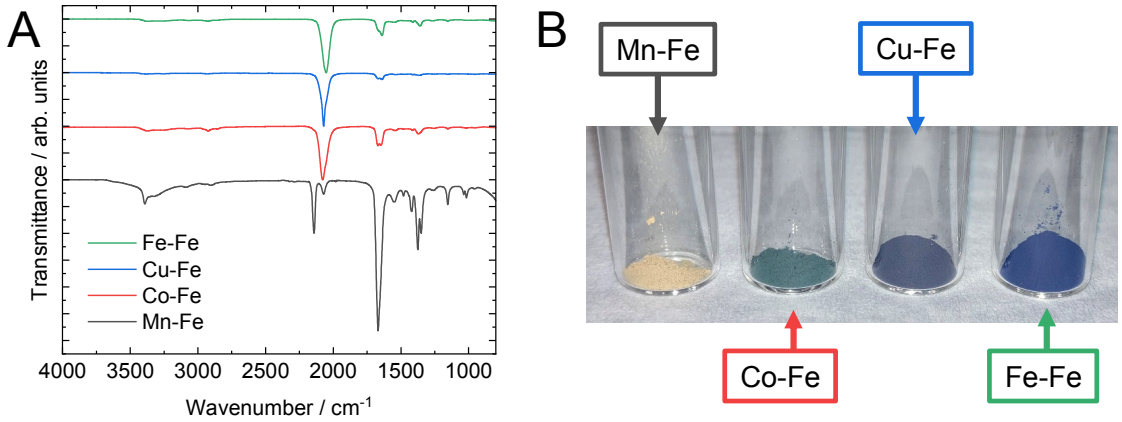


Figure 5.3: FTIR spectra (A) and appearance (B) of mixed-valence transition metal hexacyanoferrates. Cobalt, copper and iron hexacyanoferrate exhibit a single peak in the ν(CN) region at 2078 cm^{-1}, 2071 cm^{-1} and 2052 cm^{-1}, respectively. Manganese hexacyanoferrate shows two peaks at 2071 cm^{-1} and 2142 cm^{-1}, as well as a comparatively larger signal from residual NMF solvent, located < 1700 cm^{-1} and between 2800 cm^{-1} to 3500 cm^{-1}. The observed green and purple colour of mixed-valent cobalt and copper hexacyanoferrate, respectively, are in contrast to observations for materials synthesised from standard aqueous syntheses.

shown comprehensively by Shimamoto *et al.*, such charge transfer phenomena are correlated with the amount of vacancies present in the materials.[325] According to this report, the raised oxidation state of the P-site transition metal is a sign of low vacancy content in the material. The difference in the electronic structure indicated in the IR spectrum for these compositions also manifests itself in different colours. While $K_xFe[Fe]_y$ shows its characteristic blue colour, $K_xCo[Fe]_y$ and $K_xCu[Fe]_y$ are dark green and purple, respectively, deviating from the red and brown colours typically found for these materials when formed in aqueous media (fig. 5.3B). For $K_xMn[Fe]_y$, two ν(CN) peaks are found in the IR spectrum at 2071 cm^{-1} and 2142 cm^{-1}. The appearance and positions of the two peaks are consistent with literature results for this composition from aqueous synthesis, and correspond to stretching vibrations of $Mn^{II}-C\equiv N-Fe^{III}$ and $Mn^{III}-C\equiv N-Fe^{II}$ moieties present in the material.[223, 330, 331] Its colour is brown, as found for materials formed in aqueous media (fig. 5.3B). It is noteworthy that in the FTIR spectra of all analysed materials, the signal of residual NMF molecules is present (peaks at < 1700 cm^{-1} and 2800 cm^{-1} to 3500 cm^{-1}). In the spectrum of $K_xMn[Fe]_y$, the relative intensities of

Material	$K_xMn[Fe]_y$	$K_xCo[Fe]_y$	$K_xCu[Fe]_y$	$K_xFe[Fe]_y$
Fe : P ratio	0.667(19)	0.998(22)	1.04(2)	N/A
K : P ratio	0.167(4)	1.11(1)	1.31(2)	0.435(8)

Table 5.4: Elemental stoichiometric ratios of mixed-valence materials synthesised in NMF determined by ICP-OES chemical analysis including statistical error of measurement.

the solvent's signal is considerably higher than for the other compositions. Although not reliably quantifiable, this could indicate an increased amount of solvent present, as discussed in more detail below. The characterisation via XRD and IR spectroscopy confirms that the formed materials are the expected PBAs obtained via the reactions given in the formulas 5.2. However, determining which of the respective pathways is assumed for the individual materials requires further analysis.

The different (111) peak intensities mentioned above qualitatively hint at a different vacancy content and therefore a different formation mechanism for the individual materials. To gain precise quantitative information, a chemical analysis is carried out. In the case of all materials but $K_xFe[Fe]_y$, the composition can be quantified using stoichiometric ratios of the constituent metals determined by ICP-OES. Table 5.4 summarises the measured K : P and Fe : P ratios. These ratios correspond to materials compositions of $K_{0.17}Mn[Fe]_{0.67}$, $K_{1.1}Co[Fe]_{1.0}$ and $K_{1.3}Cu[Fe]_{1.0}$. Although the statistical error of the experiment is low, a substantially higher systematic error in the content of K in the materials is expected. This is based on the abundance of potassium and its presence as a trace element in the environment and the acids used in digestion. The true potassium content is expected to be better described by charge balance. Therefore, in accord with this principle, compositions of $Mn[Fe]_{2/3}$, KCo[Fe] and KCu[Fe] are used in this discussion. In the case of KFe[Fe], the vacancy fraction cannot be extracted from the Fe : Fe ratio for obvious reasons. The two sites could be distinguished via Mössbauer spectroscopy, but this analysis is out of the scope of this work. However, based on the missing (111) peak in the material's XRD pattern (fig. 5.2), the material is expected to exhibit a vanishingly small vacancy content. With this input, the measured potassium content corresponds to a composition of $K_{0.87}Fe[Fe]$,

close to the charge-balanced KFe[Fe]. The results show that the non-aqueous synthesis has led to low-vacancy KCo[Fe], KCu[Fe] and KFe[Fe] materials. In contrast, the manganese analogue $Mn[Fe]_{2/3}$ forms as a highly vacant material. The comparison to materials synthesised in aqueous media demonstrates that NMF exerts a vacancy-suppressing effect on the studied mixed-valence cobalt, copper and iron hexacyanoferrates. In mixed-valence manganese hexacyanoferrate, however, the use of NMF does not inhibit vacancy formation and the resulting material possesses a high vacancy concentration with a composition equivalent to what is obtained from aqueous syntheses. This leaves the question of why NMF suppresses the formation of vacancies some of the tested compositions, but not all.

To rule out residual water as the cause of vacancy formation, the water content in the $MnCl_2$ solution is measured. The determined amount of 63.7 ppm is too low to have a considerable effect and can be neglected. Therefore, the different mechanisms are suggested to have a more fundamental origin.

As was reasoned in earlier work, the mechanism of vacancy suppression is an effect of steric hindrance of solvent molecules inside the PBA structure, which leads to the inability of solvent molecules to enter the structure and stabilise vacancies.[273] For a given material, this takes effect when the solvent molecules are too large to be inserted into the structure. In other words, a lower critical molecular size exists to facilitate vacancy suppression. This suggests that for a given solvent an upper critical unit cell size exists, up to which vacancies are suppressed.

$Mn[Fe]_{2/3}$ has in fact a larger unit cell than all other studied compositions (table 5.3). While the resulting increased distances between charged species around vacancies lowers the energy toll of vacancies, electrostatics and aspects regarding ligand field stabilisation are still expected to render uncoordinated vacancies highly thermodynamically disadvantageous. Vacancy formation therefore likely requires the shielding effect from coordinated solvents within the structure. The observed high vacancy content could indicate that $Mn[Fe]_{2/3}$ possesses a unit cell size above the critical value for vacancy suppression by the chosen solvent

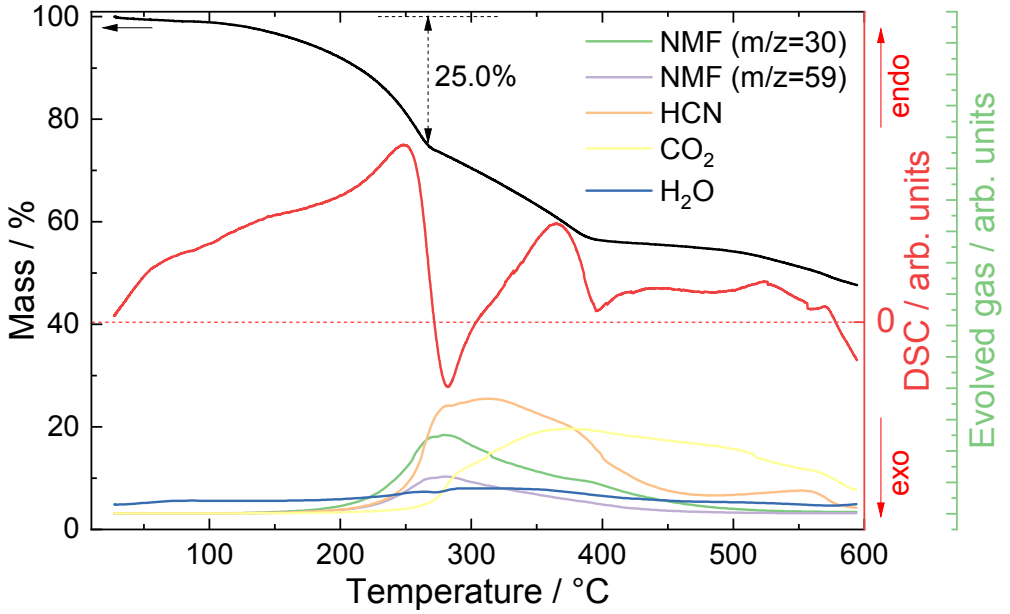


Figure 5.4: TGA-MS analysis of $Mn[Fe]_{2/3}$. 25% of the sample's mass is lost up to a temperature of 267 °C through an endothermic process under release of NMF. In this temperature region, an increasing evolution of NMF solvent is detected. The material decomposes in two exothermic steps at 267 °C and 390 °C, under the typical release of HCN and CO_2. The water signal remains at background level throughout the measured temperature range.

NMF, whereas in the other studied materials the unit cell is sufficiently small to observe vacancy suppression.

In order to test this hypothesis, the presence of NMF molecules in the crystal structure of $Mn[Fe]_{2/3}$ must be examined. FTIR spectroscopy is able to identify the presence of NMF molecules. However, the characteristic peaks are visible in the spectra for all studied materials, as mentioned above. Although the visible enlargement of these peaks for $Mn[Fe]_{2/3}$ is striking, this technique is not suitable to extract quantitative information. Due to the many degrees of freedom in the system to be refined, a quantitative structural analysis is impractical. A thermogravimetric analysis of the material, coupled with exhaust gas analysis, is suitable to quantify the amount of NMF in the structure.

The TGA-MS traces for $Mn[Fe]_{2/3}$ are depicted in fig. 5.4. The mass loss curve exhibits the typical behaviour for a highly vacant PBA. Up to 267 °C, the material gradually loses 25 % of its mass. The DSC signal shows that this process

is endothermic. In this temperature range, the solvent molecules evaporate from the material. The evolved gas analysis shows that the detected water signal does not rise beyond the background level, which confirms the absence of water in the material. Instead, the MS signal of the two characteristic lines for NMF ($CH_2NH_2^+$ $m/z = 30$ and $C_2H_5NO^+$ $m/z = 59$) increases in accordance with the measured mass loss. This supports the presence of NMF in the material, amounting to 25.0 % of the material's mass and corresponding to 1.11 NMF molecules per formula unit. The solvent is released far above its bulk boiling point ($\approx 180\,^\circ$C), which shows that the NMF molecules are bonded within the material. Right above the drying of the material, its thermal decomposition begins, as is evidenced by the sharp increase in the HCN and CO_2 levels. This happens in two clearly distinguishable steps at 267 °C and 390 °C. Both decomposition processes are accompanied by exothermic spikes in the DSC trace, as expected. Interestingly, NMF is released throughout the first decomposition step. Although not conclusive, this could indicate that lattice destabilisation is caused by the amount of solvent falling below a critical value.

The results from the thermal analysis of $Mn[Fe]_{2/3}$ demonstrate that bonded NMF molecules in the structure enable the formation $Fe(CN)_6^{3-}$ vacancies. In stark contrast to the observed results for Cr[Cr] shown in fig. 3.8, sufficient amounts of NMF can be inserted into the structure to obtain their vacancy-stabilising effect. The finding of large NMF molecules in the structure is also consistent with the expanded unit cell parameter of $Mn[Fe]_{2/3}$. These results confirm the hypothesis that vacancy suppression effect results from steric hindrance of solvent molecules in the PBA structure. Additionally, they support the existence of a critical unit cell size up to which this effect is observable. Based on the tested compositions in this chapter and chapter 3, the critical unit cell volume, V_{crit}, for NMF lies between $1097\,\text{Å}^3 < V_{\mathrm{crit}} < 1206\,\text{Å}^3$. To obtain solvent-mediated vacancy suppression in PBA materials with larger unit cells, the presented results advise the use of solvents with increased molecule sizes.

5.5 Conclusion

This chapter explores the extension of the non-aqueous synthesis used in chapter 3 to other PBA compositions using fully reduced and mixed-valence transition metal hexacyanoferrates as test system. The results show that even in highly polar solvents the solubility of precursors remains a limitation. This obstacle prevents the synthesis of fully reduced transition metal hexacyanoferrates in NMF. An alternative route starting from a simple cyanide precursor and divalent iron ions is shown to result in a poorly crystalline material, likely due to the low retention time of the intermediate complex in solution. The formation of a variety of mixed-valence compositions is however successful in the non-aqueous medium. Physicochemical analysis demonstrates that the formed precipitates are crystalline, vacancy-less KCu[Fe], KCo[Fe] and KFe[Fe] nanoparticles.

The presented strategy marks the first viable way to achieve vacancy-suppressed mixed-valence PBAs without the use of large counterions. As such, the results open up new possibilities in energy storage research, where the nature of inserted ions is pre-determined by the studied system. Since the materials' available interstitial sites are half occupied by inserted ions, the KCo[Fe] and KFe[Fe] materials with two redox centres per formula unit can act as both a source and sink of ions in electrochemical systems. This makes them relevant as reference electrodes in K-ion batteries, which were identified as one of the critical challenges in this highly active research field.[164] A limitation of the synthetic methodology is the obtained small particle sizes, which can lead to accelerated material dissolution and surface-driven side reactions in electrochemical applications. The synthesised materials' performance remains to be tested as suggested future work.

In contrast to these compositions, mixed-valence manganese hexacyanoferrate forms as the highly vacant $Mn[Fe(CN)_6]_{2/3}$. The analysis of this phenomenon enables the exploration of the boundaries of solvent-mediated vacancy suppression. The results show that NMF molecules can occupy sites within the PBA structure and stabilise vacancies in this composition. This is consistent with the increased unit cell size of $Mn[Fe(CN)_6]_{2/3}$ compared to the other studied compositions. These

results confirm that the explored vacancy suppressing effect is caused by steric hindrance of solvent molecules in the PBA structure due to their large molecular size. The compositions studied in this chapter and chapter 3 indicate that NMF prevents the formation of vacancies in materials with unit cell volumes up to a critical value between 1097 $Å^3$ and 1206 $Å^3$. This range could be further narrowed by studying additional compositions, for example mixed-valence materials in the hexacyanocobaltate family, for which a wide range of lattice parameters from 10.2 Å to 10.6 Å has been reported.[332–335]

The work presented in this chapter challenges the view of the solvent used for PBA synthesis as merely being a reaction medium. Instead, a careful choice and combination of solvent chemistries could allow for the formation of materials with tailored structural features and properties.

5.6 Experimental

For the attempted synthesis of fully reduced iron hexacyanoferrate, NaCN and RbCl are weighed out, vacuum-dried and brought into an argon-filled glovebox for use. The NaCN and RbCl are dissolved in 5 mL anhydrous NMF to form a 240 mM and 160 mM solution, respectively. $FeCl_2$ is dissolved in 5 mL anhydrous NMF to form a 80 mM solution. The KCN and RbCl solution is heated to 180 °C, at which temperature the $FeCl_2$ solution is added dropwise. After mixing, the liquid is allowed to cool down inside the glovebox. It is then sealed and centrifuged outside the glovebox. The material is washed twice by redispersing into anhydrous NMF followed by centrifugation. The material is dried in vacuum and brought into the glovebox without air exposure.

For the synthesis of mixed-valence materials, transition metal chloride salts are dehydrated under vacuum at 100 °C and brought into an argon-filled glovebox for use and storage. $FeCl_2$ is bought as anhydrous and used as received. In the glovebox, the respective transition metal chloride salts are dissolved in 5 mL anhydrous NMF to form a 50 mM solution. $K_3Fe(CN)_6$ is dissolved separately in 5 mL anhydrous NMF to form a 50 mM solution. The $K_3Fe(CN)_6$ solution is heated to 180 °C, at which

temperature the respective transition metal chloride solution is added dropwise under constant strong stirring. After mixing, the liquid is allowed to cool down inside the glovebox, before it is filled into a centrifuge tube and brought outside the glovebox for further processing. The material is collected via centrifugation and repeatedly redispersed into clean NMF and centrifuged twice to wash out unreacted precursors. The material is dried in vacuum at 100 °C.

For ICP measurements, the materials are additionally washed twice with ultrapure water due to the slow dissolution of $K_3Fe(CN)_6$ in NMF.

For the TGA measurement, the $Mn[Fe]_{2/3}$ sample is dried at 40 °C in vacuum instead of 100 °C to preserve possible solvent in the structure.

6
Conclusion and outlook

Contents

6.1 Conclusion 133
6.2 Outlook 135

6.1 Conclusion

PBAs are a fascinating materials system, whose wide range of unique properties has sparked interest for many fields of application. Especially in the context of battery materials and molecular magnetism, PBAs are among the most promising materials due to their high electrochemical potentials and ion storage capacities, as well as stimuli-responsive and high-temperature magnetic ordering. All of these attributes are deeply rooted in the materials' chemistry and structure. It is therefore a crucial research front to expand the composition space in order to find a so-far missing high-capacity PBA anode material, an air-stable room-temperature molecular magnet and other functional materials with capabilities yet to be discovered.

In this thesis, a synthesis methodology recently developed in this group is optimised and applied to various PBA compositions, chosen on the basis of substantiated theories for their magnetic and electrochemical properties. This work

has led to the successful synthesis and characterisation of previously inaccessible PBA compositions with intriguing properties, and sheds light on the fundamental mechanisms underlying PBA formation.

The results found contribute to the understanding in this wide and vast research field that is PBAs. The work presented herein will hopefully act as a stepping stone for the development of molecular magnetic devices and urgently needed future energy storage solutions.

In brief summary, the individual chapters resulted in the following outcomes.

In chapter 3, a non-aqueous synthesis procedure is improved, which allows for the synthesis of reduced and fully oxidised chromium hexacyanochromate. This has enabled a thorough and quantitative physicochemical characterisation of the formed materials, which proves the absence of vacancies in their structure. Additionally, a new synthesis approach explores the formation of mixed-valence chromium hexacyanochromate. Through the realisation of this composition in its three oxidation states, long-standing ambiguities about its oxidation states could be resolved conclusively. The work in this chapter lays the foundation for the analysis of this composition's performance as battery and magnetic material in the following chapter.

Chapter 4 studies the magnetic and electrochemical properties of the fully oxidised chromium hexacyanochromate synthesised in chapter 3. Against expectations, the material is not a room-temperature magnet, but loses its magnetic order at 240 K. Due to a slight spin imbalance, the material is ferrimagnetic below this temperature, which gives rise to a superparamagnetic behaviour because of its nanometer-sized particle dimensions. The material's electrochemical properties are measured in both K^+ and Na^+ electrolytes. Results of galvanostatic experiments show two clearly distinguishable, reversible redox processes at low potentials. A reversible capacity of $(127 \pm 4)\,\mathrm{mA\,h\,g^{-1}}$ and $(145 \pm 2)\,\mathrm{mA\,h\,g^{-1}}$ is found respectively for the two inserting ions. These values mark the current highest-capacity PBA anode material. Furthermore, despite the small particle size and low potentials, the material exhibits remarkable cycling stability.

In chapter 5, the non-aqueous synthetic approach is extended to the family of iron-based PBA compositions. Experiments show that with the chosen solvent, the formation of reduced-state transition metal hexacyanoferrates is inaccessible due to the insolubility of the ferrocyanide complex. In contrast, the synthesis successfully yields several crystalline mixed-valence materials. The compositional analysis shows that the synthetic methodology is able to afford vacancy-free materials, analogous to the chromium-based materials in chapter 3. The results further elaborate that the solvent's vacancy suppressing effect is limited to materials with a sufficiently low unit cell size. Using the tested compositions, a lower and upper boundary for a critical unit cell volume is determined for the used solvent, above which highly vacant materials form.

6.2 Outlook

The results presented in this thesis suggest the investigation of the following aspects in further work.

- The results on vacancy-free chromium hexacyanochromate are a strong pointer towards further increasing its particle size. Attempts should be made using slow diffusion and microfluidic mixing as possible routes to achieve this goal. The described strategy to synthesise the mixed-valence material as intermediate is especially promising as it does not require to start from toxic simple cyanides and the involved K^+ is easier to extract from the interstitial sites than the Rb^+ used when synthesising the reduced material, which is a considerable problem since the larger particles need to be fully chemically oxidised. This strategy has the added benefit that the P and R site constituents stem from different unique precursors, which could allow for the growth of larger particles layer-by-layer by alternating addition of precursors during the reaction.

- The magnetic characterisation presented in this work suggests that the magnetic ordering temperature of the studied material might be held back

by its limited particle size. When this is mitigated, as discussed in the previous point, chromium hexacyanochromate might be the first air-stable PBA with room-temperature magnetisation. In larger, multi-domain particles the material will additionally possess a more robust magnetisation and could act as a platform for doping to tune the exact magnetic behaviour.

- Efforts should be made to achieve the full theoretical ion storage capacity of chromium hexacyanochromate. This could be achieved by an optimised electrode preparation which ensures optimal electronic and ionic contact. Also in this context a larger particle size is beneficial, as it decreases the amount of inactive conductive matrix needed to achieve electric contact and reduces parasitic surface reactions as well as active material dissolution. Furthermore, the material should be tested with the currently most promising contestant as cathode material, manganese hexacyanoferrate in Na^+ and K^+ full cells. These studies should be carried out in a suitable electrolyte to assess the expected high rate capability of the PBA-PBA battery cell.

- The synthesised zero-vacancy mixed-valence transition metal hexacyanoferrates should be explored as possible reference electrodes and active materials in electrochemical systems. Apart from this application, their half-charged state makes them also interesting for Cs^+ sorption, as is required for nuclear wastewater treatment.[336] Additionally, their electronic properties should be looked at in detail. Because of the observed charge transfer in the synthesised materials, they could allow for insights into the relationship between vacancies and electronic state, which is crucial for the understanding of the stimuli-responsive charge transfer processes reported in these materials.[50, 148, 337]

- In light of the successful synthesis of PBAs based on Cr and Fe demonstrated in this work, the non-aqueous synthetic approach should be used to explore additional, so far inaccessible compositions. The methodology is especially well suited for air- and moisture-sensitive compounds, such as reduced hexacyanochromates and hexacyanovanadates. Using a soluble V^{II}

salt, it should be tested if a PBA with composition $A_2V[V]$ can be made. So far, divalent vanadium has been reported in both the P and R site of the PBA, but never together in one material.[123, 132] From magnetic orbital theories, this composition could be the PBA material with highest magnetic ordering temperature achievable.

- Analogous to the point above, other solvents and solvent mixtures should be explored for PBA synthesis. Altering the parameters molecular size and dielectric constant, different reaction media could allow for the tuning of structural and compositional parameters for different materials in a controlled manner. Such a solvent-as-reactant approach is entirely unexplored in PBA science so far.

References

[1] Alexander Kraft. “On the Discovery and History of Prussian Blue”. In: *Bull. Hist. Chem.* 32.2 (2008), pp. 61–67.

[2] H. J. Buser et al. “The crystal structure of Prussian Blue: Fe4[Fe(CN)6]3.xH2O”. In: *Inorg. Chem.* 16.11 (1977), pp. 2704–2710.

[3] John Brown. “V. Observation and experiments upon the foregoing preparation”. In: *Philos. Trans. R. Soc. London* 33.381 (1724), pp. 17–24.

[4] Kevin Hurlbutt et al. “Prussian Blue Analogs as Battery Materials”. In: *Joule* 2.10 (2018), pp. 1950–1960.

[5] Robert A. Huggins. “Review—A New Class of High Rate, Long Cycle Life, Aqueous Electrolyte Battery Electrodes”. In: *J. Electrochem. Soc.* 164.1 (2017), A5031–A5036.

[6] Michel Verdaguer and Gregory S. Girolami. “Magnetic Prussian Blue Analogs”. In: *Magn. Mol. to Mater.* Vol. 5-5. Weinheim, Germany: Wiley-VCH Verlag GmbH & Co. KGaA, 2005, pp. 283–346.

[7] N. A. Curry and W. A. Runciman. “A neutron-diffraction study of potassium cobalticyanide”. In: *Acta Crystallogr.* 12.9 (1959), pp. 674–678.

[8] D. T. Cromer and A. C. Larson. “The use of electron population parameters to distinguish between carbon and nitrogen in cyanide complexes”. In: *Acta Crystallogr. Sect. B Struct. Crystallogr. Cryst. Chem.* 29.2 (1973), pp. 251–253.

[9] Kim R. Dunbar and Robert A. Heintz. “Chemistry of Transition Metal Cyanide Compounds: Modern Perspectives”. In: *Prog. Inorg. Chem. Vol. 45*. Wiley, 1997, pp. 283–391.

[10] S. F. A. Kettle. *Physical Inorganic Chemistry : A Coordination Chemistry Approach*. 1st ed. Berlin, Heidelberg: Springer Berlin, Heidelberg, 1996.

[11] Janice P. Eaton and David Nicholls. “The complex cyanides of chromium(II) and chromium(0)”. In: *Transit. Met. Chem.* 6.4 (1981), pp. 203–206.

[12] W.P. Griffith. “Cyanide complexes of the early transition metals (groups IVa-VIIa)”. In: *Coord. Chem. Rev.* 17.2-3 (1975), pp. 177–247.

[13] Kliment I Kugel’ and D I Khomskiĭ. “The Jahn-Teller effect and magnetism: transition metal compounds”. In: *Sov. Phys. Uspekhi* 25.4 (1982), pp. 231–256.

[14] J.R. Armstrong et al. “Single crystal vibrational spectroscopic and neutron diffraction studies of the hexacyanometallates, Cs2LiM(CN)6 (M = Cr, Mn, Fe and Co)”. In: *Inorg. Nucl. Chem. Lett.* 9.10 (1973), pp. 1025–1029.

[15] M.-A. Arrio et al. “Characterization of Chemical Bonds in Bimetallic Cyanides Using X-ray Absorption Spectroscopy at L 2,3 Edges”. In: *J. Am. Chem. Soc.* 118.27 (1996), pp. 6422–6427.

[16] A. K. van Bever. “The crystal structure of some ferricyanides with bivalent kations”. In: *Recl. des Trav. Chim. des Pays-Bas* 57.11 (2010), pp. 1259–1268.

[17] Hyun-Wook Lee et al. “Effect of the alkali insertion ion on the electrochemical properties of nickel hexacyanoferrate electrodes”. In: *Faraday Discuss.* 176 (2014), pp. 69–81.

[18] Mauro Pasta et al. “Full open-framework batteries for stationary energy storage”. In: *Nat. Commun.* 5.1 (2014), p. 3007.

[19] L.J.M. Coleby. “A history of Prussian blue”. In: *Ann. Sci.* 4.2 (1939), pp. 206–211.

[20] Richard E. Wilde, Surendra Nath Ghosh, and Billy J. Marshall. “The Prussian Blues”. In: *Inorg. Chem.* 9.11 (1970), pp. 2512–2516.

[21] Yongsheng Yang et al. “Quantitative measurement of cyanide released from Prussian Blue”. In: *Clin. Toxicol.* 45.7 (2007), pp. 776–781.

[22] Philipp Marzak et al. “Electrodeposited Na2Ni[Fe(CN)6] Thin-Film Cathodes Exposed to Simulated Aqueous Na-Ion Battery Conditions”. In: *J. Phys. Chem. C* 122.16 (2018), pp. 8760–8768.

[23] E. Reguera et al. “Unique Coordination of Copper in Hexacyanometallates”. In: *Zeitschrift für Phys. Chemie* 220.12 (2006), pp. 1609–1619.

[24] Sidney F.A. Kettle et al. “The vibrational spectra of the cyanide ligand revisited: The ν(CN) infrared and Raman spectroscopy of Prussian blue and its analogues”. In: *J. Raman Spectrosc.* 42.11 (2011), pp. 2006–2014.

[25] Janos Mink et al. “Vibrational properties and bonding analysis of copper hexacyanoferrate complexes in solid state”. In: *Appl. Spectrosc. Rev.* 54.5 (2019), pp. 369–424.

[26] Toshiaki Moriya et al. “Persistence and Amalgamation Types of CN Stretching Mode in Oxidation Process of Prussian Blue Analogues”. In: *J. Phys. Soc. Japan* 89.6 (2020), p. 064708.

[27] John Cattermull, Mauro Pasta, and Andrew L. Goodwin. “Structural complexity in Prussian blue analogues”. In: *Mater. Horizons* 8.12 (2021), pp. 3178–3186. arXiv: 2107.07448.

[28] W.-D. Griebler and D. Babel. “Röntgenograpliische und magnetische Untersuchungen an perowskitverwandten Cyanoverbindungen CsM II M III (CN) 6 / X-Ray and Magnetic Studies of Perovskite-Related Cyano Compounds CsM II M III (CN) 6”. In: *Zeitschrift für Naturforsch. B* 37.7 (1982), pp. 832–837.

[29] John Cattermull et al. “Uncovering the Interplay of Competing Distortions in the Prussian Blue Analogue K 2 Cu[Fe(CN) 6]”. In: *Chem. Mater.* 34.11 (2022), pp. 5000–5008.

[30] Xiaofei Bie et al. “A novel K-ion battery: hexacyanoferrate(ii)/graphite cell”. In: *J. Mater. Chem. A* 5.9 (2017), pp. 4325–4330.

[31] Hanna L. B. Boström et al. “High-pressure behaviour of Prussian blue analogues: interplay of hydration, Jahn-Teller distortions and vacancies”. In: *Dalt. Trans.* 48.5 (2019), pp. 1647–1655.

[32] Wataru Kosaka et al. “Synthesis of Ferromagnetic CsCuCr Prussian Blue Analogue with a Tetragonal Structure”. In: *Chem. Lett.* 34.9 (2005), pp. 1278–1279.

[33] Dickson O. Ojwang et al. “Structure Characterization and Properties of K-Containing Copper Hexacyanoferrate”. In: *Inorg. Chem.* 55.12 (2016), pp. 5924–5934.

[34] Dariusz Wardecki et al. “Neutron Diffraction and EXAFS Studies of K 2 x /3 Cu[Fe(CN) 6] 2/3 · n H 2 O”. In: *Cryst. Growth Des.* 17.3 (2017), pp. 1285–1292.

[35] Yutaro Kurihara, Tomoyuki Matsuda, and Yutaka Moritomo. “Structural Properties of Manganese Hexacyanoferrates against Li Concentration”. In: *Jpn. J. Appl. Phys.* 52 (2013), p. 017301.

[36] T. Matsuda, Y. Kurihara, and Y. Moritomo. “Lithium intercalation properties in manganese-iron Prussian blue analogues”. In: *J. Phys. Conf. Ser.* 428.1 (2013), p. 012019.

[37] Yutaka Moritomo et al. “Cubic-Rhombohedral Structural Phase Transition in Na1.32Mn[Fe(CN)6]0.83 · 3.6 H2O”. In: *J. Phys. Soc. Japan* 80.7 (2011), p. 074608.

[38] Yue Xu et al. “Structure Distortion Induced Monoclinic Nickel Hexacyanoferrate as High-Performance Cathode for Na-Ion Batteries”. In: *Adv. Energy Mater.* 9.4 (2019), p. 1803158.

[39] Bingxing Xie et al. “Understanding the Structural Evolution and Lattice Water Movement for Rhombohedral Nickel Hexacyanoferrate upon Sodium Migration”. In: *ACS Appl. Mater. Interfaces* 11.50 (2019), pp. 46705–46713.

[40] Wanlin Wang et al. “Reversible structural evolution of sodium-rich rhombohedral Prussian blue for sodium-ion batteries”. In: *Nat. Commun.* 11.1 (2020), p. 980.

[41] Jae-Hyuk Her et al. “Anomalous Non-Prussian Blue Structures and Magnetic Ordering of K 2 Mn II [Mn II (CN) 6] and Rb 2 Mn II [Mn II (CN) 6]”. In: *Inorg. Chem.* 49.4 (2010), pp. 1524–1534.

[42] Christopher M. Kareis et al. “Non-Prussian Blue Structures and Magnetic Ordering of Na 2 Mn II [Mn II (CN) 6] and Na 2 Mn II [Mn II (CN) 6] · 2H 2 O”. In: *J. Am. Chem. Soc.* 134.4 (2012), pp. 2246–2254.

[43] K. Tennakone and W G D Dharmaratne. “Experimental and theoretical study of electronic conduction in H 2 O-doped Prussian blue”. In: *J. Phys. C Solid State Phys.* 16.29 (1983), pp. 5633–5639.

[44] Kevin Hurlbutt et al. “Electronic Structure and Electron-Transport Properties of Three Metal Hexacyanoferrates”. In: *Chem. Mater.* 33.17 (2021), pp. 7067–7074.

[45] Kingo Itaya et al. “Prussian-blue-modified electrodes: An application for a stable electrochromic display device”. In: *J. Appl. Phys.* 53.1 (1982), pp. 804–805.

[46] L. M.N. Assis et al. “Prussian blue for electrochromic devices”. In: *J. Electroanal. Chem.* 777 (2016), pp. 33–39.

[47] Naike Shi et al. “Negative thermal expansion in cubic FeFe(CN) 6 Prussian blue analogues”. In: *Dalt. Trans.* 48.11 (2019), pp. 3658–3663.

[48] Andrew L. Goodwin and Cameron J. Kepert. "Negative thermal expansion and low-frequency modes in cyanide-bridged framework materials". In: *Phys. Rev. B* 71.14 (2005), p. 140301.

[49] David M. Rogers and J. Olof Johansson. "Metal-to-metal charge-transfer transitions in Prussian blue hexacyanochromate analogues". In: *Mater. Sci. Eng. B* 227 (2018), pp. 28–38.

[50] Marco Cammarata et al. "Charge transfer driven by ultrafast spin transition in a CoFe Prussian blue analogue". In: *Nat. Chem.* 13.1 (2021), pp. 10–14.

[51] Michel Verdaguer and Alain N. Gleizes. "Magnetism: Molecules to Build Solids". In: *Eur. J. Inorg. Chem.* 2020.9 (2020), pp. 723–731.

[52] Jiangfeng Qian et al. "Prussian Blue Cathode Materials for Sodium-Ion Batteries and Other Ion Batteries". In: *Adv. Energy Mater.* 8.17 (2018), pp. 1–24.

[53] Victor K. LaMer and Robert H Dinegar. "Theory, Production and Mechanism of Formation of Monodispersed Hydrosols". In: *J. Am. Chem. Soc.* 72.11 (1950), pp. 4847–4854.

[54] Long Wang et al. "A Superior Low-Cost Cathode for a Na-Ion Battery". In: *Angew. Chemie Int. Ed.* 52.7 (2013), pp. 1964–1967.

[55] Xiaofei Bie et al. "Synthesis and electrochemical properties of Na-rich Prussian blue analogues containing Mn, Fe, Co, and Fe for Na-ion batteries". In: *J. Power Sources* 378.September 2017 (2018), pp. 322–330.

[56] Wei-Jie Li et al. "Facile Method To Synthesize Na-Enriched Na 1+ x FeFe(CN) 6 Frameworks as Cathode with Superior Electrochemical Performance for Sodium-Ion Batteries". In: *Chem. Mater.* 27.6 (2015), pp. 1997–2003.

[57] Hyun-Wook Lee et al. "Manganese hexacyanomanganate open framework as a high-capacity positive electrode material for sodium-ion batteries". In: *Nat. Commun.* 5.1 (2014), p. 5280.

[58] Michele Fiore et al. "Paving the Way toward Highly Efficient, High-Energy Potassium-Ion Batteries with Ionic Liquid Electrolytes". In: *Chem. Mater.* 32.18 (2020), pp. 7653–7661.

[59] Fumiyuki Shiba et al. "Preparation of Monodisperse Cobalt(II) Hexacyanoferrate(III) Nanoparticles Using Cobalt Ions Released from a Citrate Complex". In: *J. Phys. Chem. C* 116.5 (2012), pp. 3394–3399.

[60] Samuel Wheeler et al. "Low-Potential Prussian Blue Analogues for Sodium-Ion Batteries: Manganese Hexacyanochromate". In: *Chem. Mater.* 31.7 (2019), pp. 2619–2626.

[61] Leqing Deng et al. "Defect-free potassium manganese hexacyanoferrate cathode material for high-performance potassium-ion batteries". In: *Nat. Commun.* 12.1 (2021), p. 2167.

[62] J. Bácskai et al. "Polynuclear nickel hexacyanoferrates: monitoring of film growth and hydrated counter-cation flux/storage during redox reactions". In: *J. Electroanal. Chem.* 385.2 (1995), pp. 241–248.

[63] Kavita M. Jeerage, William A. Steen, and Daniel T. Schwartz. "Correlating Nanoscale Structure with Ion Intercalation in Electrodeposited Nickel Hexacyanoferrate Thin Films". In: *Chem. Mater.* 14.2 (2002), pp. 530–535.

[64] Wei Chen, Jian Tang, and Xing-Hua Xia. “Composition and Shape Control in the Construction of Functional Nickel Hexacyanoferrate Nanointerfaces”. In: *J. Phys. Chem. C* 113.52 (2009), pp. 21577–21581.

[65] Vladimir D. Ivanov. “Four decades of electrochemical investigation of Prussian blue”. In: *Ionics (Kiel).* 26.2 (2020), pp. 531–547.

[66] Paulo Roberto Bueno et al. “Synchrotron Structural Characterization of Electrochemically Synthesized Hexacyanoferrates Containing K + : A Revisited Analysis of Electrochemical Redox”. In: *J. Phys. Chem. C* 112.34 (2008), pp. 13264–13271.

[67] Wayne E. Buschmann et al. “Reversed (Negative) Magnetization for Electrochemically Deposited High-Tc Thin Films of Chromium Hexacyanide Magnets”. In: *Chem. Mater.* 10.5 (1998), pp. 1386–1395.

[68] Xianyong Wu et al. “Low Defect FeFe(CN) 6 Framework as Stable Host Material for High Performance Li-Ion Batteries”. In: *ACS Appl. Mater. Interfaces* 8.36 (2016), pp. 23706–23712.

[69] Ya You et al. “High-quality Prussian blue crystals as superior cathode materials for room-temperature sodium-ion batteries”. In: *Energy Environ. Sci.* 7.5 (2014), pp. 1643–1647.

[70] William R. Brant et al. “Selective Control of Composition in Prussian White for Enhanced Material Properties”. In: *Chem. Mater.* 31.18 (2019), pp. 7203–7211.

[71] Jianhui Yang et al. “Large-Scale Synthesis of Berlin Green Fe[Fe(CN) 6] Microcubic Crystals”. In: *Cryst. Growth Des.* 6.11 (2006), pp. 2438–2440.

[72] *CATL Unveils Its Latest Breakthrough Technology by Releasing Its First Generation of Sodium-ion Batteries*. 2021.

[73] Arthur L. Robinson. “Powerful New Magnet Material Found”. In: *Science* 223.4639 (1984), pp. 920–922.

[74] M. Sagawa et al. “New material for permanent magnets on a base of Nd and Fe (invited)”. In: *J. Appl. Phys.* 55.6 (1984), pp. 2083–2087.

[75] R. M. White. “Opportunities in Magnetic Materials”. In: *Science* 229.4708 (1985), pp. 11–15.

[76] Joel S. Miller and Arthur J. Epstein. “Organic and Organometallic Molecular Magnetic Materials—Designer Magnets”. In: *Angew. Chemie Int. Ed. English* 33.4 (1994), pp. 385–415.

[77] Yulong Huang and Shenqiang Ren. “Multifunctional Prussian blue analogue magnets: Emerging opportunities”. In: *Appl. Mater. Today* 22 (2021), p. 100886.

[78] Stephen Blundell. *Magnetism in Condensed Matter*. Oxford: Oxford University Press, 2001.

[79] Olivier Kahn. *Molecular Magnetism*. New York: Dover Publications, 2021.

[80] J. Samuel Smart. “The Néel Theory of Ferrimagnetism”. In: *Am. J. Phys.* 23.6 (1955), pp. 356–370.

[81] Humberto O. Stumpf et al. “Dimensionality of manganese(II)-copper(II) bimetallic compounds and design of molecular-based magnets”. In: *J. Am. Chem. Soc.* 115.15 (1993), pp. 6738–6745.

[82] Humberto O. Stumpf et al. “Chemistry and Physics of a Molecular-Based Magnet Containing Three Spin Carriers, with a Fully Interlocked Structure”. In: *J. Am. Chem. Soc.* 116.9 (1994), pp. 3866–3874.

[83] Kendric J. Nelson et al. “[Cr III (NCMe) 6] 3+ a Labile Cr III Source Enabling Formation of Cr[M(CN) 6] (M = V, Cr, Mn, Fe) Prussian Blue-Type Magnetic Materials”. In: *Inorg. Chem.* 46.24 (2007), pp. 10093–10107.

[84] M. Louis Néel. “Propriétés magnétiques des ferrites ; ferrimagnétisme et antiferromagnétisme”. In: *Ann. Phys. (Paris).* 12.3 (1948), pp. 137–198.

[85] Oliver Kahn and B. Briat. “Exchange interaction in polynuclear complexes. Part 1.—Principles, model and application to the binuclear complexes of chromium(III)”. In: *J. Chem. Soc., Faraday Trans. 2* 72.5 (1976), pp. 268–281.

[86] Olivier Kahn and Bernard Briat. “Exchange interaction in polynuclear complexes. Part 2.—Antiferromagnetic coupling in binuclear oxo-bridged iron(III) complexes”. In: *J. Chem. Soc., Faraday Trans. 2* 72.5 (1976), pp. 1441–1446.

[87] Jean Jacques Girerd, Yves Journaux, and Olivier Kahn. “Natural or orthogonalized magnetic orbitals: Two alternative ways to describe the exchange interaction”. In: *Chem. Phys. Lett.* 82.3 (1981), pp. 534–538.

[88] P. Jeffrey Hay, Jack C. Thibeault, and Roald Hoffmann. “Orbital interactions in metal dimer complexes”. In: *J. Am. Chem. Soc.* 97.17 (1975), pp. 4884–4899.

[89] Louis Noodleman. “Valence bond description of antiferromagnetic coupling in transition metal dimers”. In: *J. Chem. Phys.* 74.10 (1981), pp. 5737–5743.

[90] Jean-Marie Mouesca. “Quantitative harmonization of the three molecular orbital, valence bond, and broken symmetry approaches to the exchange coupling constant: Corrections and discussion”. In: *J. Chem. Phys.* 113.23 (2000), pp. 10505–10511.

[91] Eliseo Ruiz et al. “Is It Possible To Get High T C Magnets with Prussian Blue Analogues? A Theoretical Prospect”. In: *Chem. - A Eur. J.* 11.7 (2005), pp. 2135–2144.

[92] Tim Krah, Nadia Ben Amor, and Vincent Robert. “Switching magnetic interactions in the NiFe Prussian Blue Analogue: an ab initio inspection”. In: *Phys. Chem. Chem. Phys.* 16.20 (2014), pp. 9509–9514.

[93] M.-F. Charlot, J.-J. Girerd, and O. Kahn. “Molecular orbital approach of antiferromagnetic coupling in linear chains AMCl3 with M = V, Mn, and Ni and A = Cs or N(CH3)4”. In: *Phys. Status Solidi* 86.2 (1978), pp. 497–504.

[94] Olivier Kahn. “Design of binuclear complexes exhibiting expected magnetic properties”. In: *J. Magn. Magn. Mater.* 54-57 (1986), pp. 1459–1463.

[95] M. Verdaguer. “Rational synthesis of molecular magnetic materials: a tribute to Olivier Kahn”. In: *Polyhedron* 20.11-14 (2001), pp. 1115–1128.

[96] Kasper S. Pedersen, Jesper Bendix, and Rodolphe Clérac. “Single-molecule magnet engineering: building-block approaches”. In: *Chem. Commun.* 50.34 (2014), pp. 4396–4415.

[97] Dominique Luneau. “Molecular magnets”. In: *Curr. Opin. Solid State Mater. Sci.* 5.2-3 (2001), pp. 123–129.

[98] George Christou et al. “Single-Molecule Magnets”. In: *MRS Bull.* 25.11 (2000), pp. 66–71.

[99] Lapo Bogani and Wolfgang Wernsdorfer. “Molecular spintronics using single-molecule magnets”. In: *Nat. Mater.* 7.3 (2008), pp. 179–186.

[100] Dong Shao and Xin-Yi Wang. “Development of Single-Molecule Magnets”. In: *Chinese J. Chem.* 38.9 (2020), pp. 1005–1018.

[101] Joel S. Miller. “Organometallic- and Organic-Based Magnets: New Chemistry and New Materials for the New Millennium”. In: *Inorg. Chem.* 39.20 (2000), pp. 4392–4408.

[102] Arthur J Banister et al. “Spontaneous Magnetization in a Sulfur–Nitrogen Radical at 36 K”. In: *Angew. Chemie Int. Ed. English* 35.21 (1996), pp. 2533–2535.

[103] J Rawson and G D McManus. “Benzo-fused dithiazolyl radicals: from chemical curiosities to materials chemistry”. In: *Coord. Chem. Rev.* 189.1 (1999), pp. 135–168.

[104] Andrea Caneschi et al. “Toward molecular magnets: the metal-radical approach”. In: *Acc. Chem. Res.* 22.11 (1989), pp. 392–398.

[105] Joel S. Miller et al. “Decamethylmanganocenium tetracyanoethenide, [Mn(C 5 Me 5) 2] + [TCNE] - —a molecular ferromagnet with an 8.8 K T c”. In: *Adv. Mater.* 3.6 (1991), pp. 309–311.

[106] Juan M Manriquez et al. “A Room-Temperature Molecular/Organic-Based Magnet”. In: *Science* 252.5011 (1991), pp. 1415–1417.

[107] Joel S. Miller. “Oliver Kahn Lecture: Composition and structure of the V[TCNE]x (TCNE=tetracyanoethylene) room-temperature, organic-based magnet – A personal perspective”. In: *Polyhedron* 28.9-10 (2009), pp. 1596–1605.

[108] Panagiota Perlepe et al. “Metal-organic magnets with large coercivity and ordering temperatures up to 242°C”. In: *Science* 370.6516 (2020), pp. 587–592.

[109] Stephen M. Holmes and Gregory S. Girolami. “New prussian blue analogues constructed from the [Cr(CN)5NO3-] and [Cr(CN)64-] anions. A building block approach to high TN ferrimagnets”. In: *Mol. Cryst. Liq. Cryst. Sci. Technol. Sect. A Mol. Cryst. Liq. Cryst.* 305 (1997), pp. 279–290.

[110] Michel Verdaguer et al. “Molecules to build solids: high TC molecule-based magnets by design and recent revival of cyano complexes chemistry”. In: *Coord. Chem. Rev.* 190-192 (1999), pp. 1023–1047.

[111] Stephen M. Holmes and Gregory S. Girolami. “Sol-Gel Synthesis of KV II [Cr III (CN) 6] · 2H 2 O: A Crystalline Molecule-Based Magnet with a Magnetic Ordering Temperature above 100 °C”. In: *J. Am. Chem. Soc.* 121.23 (1999), pp. 5593–5594.

[112] David Davidson and Lars A. Welo. “The Nature of Prussian Blue.” In: *J. Phys. Chem.* 32.8 (1928), pp. 1191–1196.

[113] R. M. Bozorth, H. J. Williams, and Dorothy E. Walsh. “Magnetic Properties of Some Orthoferrites and Cyanides at Low Temperatures”. In: *Phys. Rev.* 103.3 (1956), pp. 572–578.

[114] A. N. Holden et al. “New Low-Temperature Ferromagnets”. In: *Phys. Rev.* 102.6 (1956), pp. 1463–1463.

[115] A. Ito, M. Suenaga, and K. Ôno. “Mössbauer study of soluble prussian blue, insoluble prussian blue, and turnbull’s blue”. In: *J. Chem. Phys.* 48.8 (1968), pp. 3597–3599.

[116] Liviu Toma et al. “Synthesis, crystal structures and magnetic properties of cyanide- and phenolate-bridged [M III Ni II] 2 tetranuclear complexes (M = Fe and Cr)”. In: *Dalt. Trans.* 8 (2005), pp. 1357–1364.

[117] Jean-Noël Rebilly and Talal Mallah. “Synthesis of Single-molecule Magnets Using Metallocyanates”. In: *Single-Molecule Magnets Relat. Phenom.* Berlin/Heidelberg: Springer-Verlag, 2006, pp. 103–131.

[118] F. Herren et al. “Neutron diffraction study of Prussian Blue, Fe4[Fe(CN)6]3.xH2O. Location of water molecules and long-range magnetic order”. In: *Inorg. Chem.* 19.4 (1980), pp. 956–959.

[119] D. Babel. “Magnetism and Structure: Model Studies on Transition Metal Fluorides and Cyanides”. In: *Comments Inorg. Chem.* 5.6 (1986), pp. 285–320.

[120] Høgni Weihe and Hans U. Güdel. “Magnetic Exchange Across the Cyanide Bridge”. In: *Comments Inorg. Chem.* 22.1-2 (2000), pp. 75–103.

[121] Mihail Atanasov, Peter Comba, and Claude A. Daul. “DFT studies on the magnetic exchange across the cyanide bridge”. In: *J. Phys. Chem. A* 110.49 (2006), pp. 13332–13340.

[122] Masamichi Nishino, Yasunori Yoshioka, and Kizashi Yamaguchi. “Effective exchange interactions and magnetic phase transition temperatures in Prussian blue analogs: a study by density functional theory”. In: *Chem. Phys. Lett.* 297.1-2 (1998), pp. 51–59.

[123] William R. Entley and Gregory S. Girolami. “High-Temperature Molecular Magnets Based on Cyanovanadate Building Blocks: Spontaneous Magnetization at 230 K”. In: *Science* 268.5209 (1995), pp. 397–400.

[124] V. Gadet et al. “High-Tc Molecular-Based Magnets: A Ferromagnetic Bimetallic Chromium(III)-Nickel(II) Cyanide with Tc= 90 K”. In: *J. Am. Chem. Soc.* 114.23 (1992), pp. 9213–9214.

[125] S. Juszczyk et al. “Ferromagnetism of the Me3[Fe(CN)6]2.H20 compounds , where Me = Ni and CO”. In: *J. Phys. Condens. Matter* 6 (1994), pp. 5697–5706.

[126] C.W Ng et al. “Structure and magnetic properties of copper(II) hexacyanoferrate(III) compound”. In: *J. Phys. Chem. Solids* 62.4 (2001), pp. 767–775.

[127] N. Bagkar et al. “Magnetic properties of substitutional solid solutions of nickel and iron hexacyanoferrate–hexacyanochromate”. In: *Philos. Mag.* 85.31 (2005), pp. 3659–3672.

[128] V Gadet et al. “Towards High TC Ferro and Ferrimagnetic BI and Tridimensional Materials from Molecular Precursors BT - Magnetic Molecular Materials”. In: *Magn. Mol. Mater.* Ed. by Dante Gatteschi et al. Dordrecht: Springer Netherlands, 1991, pp. 281–295.

[129] Maria Zentkova and Marian Mihalik. “The Effect of Pressure on Magnetic Properties of Prussian Blue Analogues”. In: *Crystals* 9.2 (2019), p. 112.

[130] Heinz Nakotte et al. “Magnetic properties of some transition-metal Prussian Blue Analogs with composition M[M(C,N)] · xHO”. In: *J. Sci. Adv. Mater. Devices* 1.2 (2016), pp. 113–120.

[131] T. Mallah et al. “High-Tc Molecular-Based Magnets: Ferrimagnetic Mixed-Valence Chromium(III)-Chromium(II) Cyanides with Tc at 240 and 190 Kelvin”. In: *Science* 262.5139 (1993), pp. 1554–1557.

[132] S. Ferlay et al. “A room-temperature organometallic magnet based on Prussian blue”. In: *Nature* 378.6558 (1995), pp. 701–703.

[133] Øyvind Hatlevik et al. “Enhancement of the magnetic ordering temperature and air stability of a mixed valent vanadium hexacyanochromate(III) magnet to 99°C (372 K)”. In: *Adv. Mater.* 11.11 (1999), pp. 914–918.

[134] Pramod Bhatt et al. “Magnetic properties of electrochemically prepared crystalline films of Prussian blue-based molecular magnets K j CrIIk [CrIII(CN)6] l · mH 2O”. In: *J. Solid State Electrochem.* 17.5 (2013), pp. 1285–1293.

[135] William R Entley and Gregory S. Girolami. “New Three-Dimensional Ferrimagnetic Materials: K2Mn[Mn(CN)6], Mn3[Mn(CN)6]2 12 H2O, and CsMn[Mn(CN)6] 1/2 H2O”. In: *Inorg. Chem.* 33.23 (1994), pp. 5165–5166.

[136] R. Klenze et al. “Manganese hexacyanomanganate: Magnetic interactions via cyanide in a mixed valence Prussian blue type compound”. In: *J. Chem. Phys.* 72.11 (1980), pp. 5819–5828.

[137] M. Zentková et al. “Effect of pressure on the magnetic properties of TM 3 [Cr(CN) 6] 2 · 12H 2 O”. In: *J. Phys. Condens. Matter* 19.26 (2007), p. 266217.

[138] Isabelle Maurin et al. “Evidence for complex multistability in photomagnetic cobalt hexacyanoferrates from combined magnetic and synchrotron x-ray diffraction measurements”. In: *Phys. Rev. B - Condens. Matter Mater. Phys.* 79.6 (2009), pp. 1–9.

[139] G. Champion et al. “Photoinduced ferrimagnetic systems in Prussian blue analogues CIxCo4[Fe(CN)6]y (CI = alkali cation). 4. Characterization of the ferrimagnetism of the photoinduced metastable state in Rb1.8Co4 [Fe(CN)6]3.3 · 13H2O by K edges x-ray magnetic circular dichroism”. In: *J. Am. Chem. Soc.* 123.50 (2001), pp. 12544–12546.

[140] Shin-ichi Ohkoshi and Kazuhito Hashimoto. “Ferromagnetism of cobalt-chromium polycyanides”. In: *Chem. Phys. Lett.* 314.3-4 (1999), pp. 210–214.

[141] Tomohiro Nuida et al. “Nonlinear Magnetooptical Effects Caused by Piezoelectric Ferromagnetism in F-43m-type Prussian Blue Analogues”. In: *J. Am. Chem. Soc.* 127.33 (2005), pp. 11604–11605.

[142] Nitin Bagkar et al. “Crystalline thin films of transition metal hexacyanochromates grown under Langmuir monolayer”. In: *Thin Solid Films* 513.1-2 (2006), pp. 325–330.

[143] Shin-ichi Ohkoshi et al. “Magnetic properties and optical control of electrochemically prepared iron–chromium polycyanides”. In: *J. Electroanal. Chem.* 473.1-2 (1999), pp. 245–249.

[144] Eugenio Coronado et al. “Pressure-Tuning of Magnetism and Linkage Isomerism in Iron(II) Hexacyanochromate”. In: *J. Am. Chem. Soc.* 127.13 (2005), pp. 4580–4581.

[145] Wataru Kosaka et al. “Observation of an Fe(II) spin-crossover in a cesium iron hexacyanochromate”. In: *J. Am. Chem. Soc.* 127.24 (2005), pp. 8590–8591.

[146] Yusuke Sato et al. “Solvatomagnetism-Induced Faraday Effect in a Cobalt Hexacyanochromate-Based Magnet”. In: *J. Am. Chem. Soc.* 125.47 (2003), pp. 14590–14595.

[147] O. Sato et al. “Photoinduced Magnetization of a Cobalt-Iron Cyanide”. In: *Science* 272.5262 (1996), pp. 704–705.

[148] Hiroko Tokoro et al. “Visible-Light-Induced Reversible Photomagnetism in Rubidium Manganese Hexacyanoferrate”. In: *Chem. Mater.* 20.2 (2008), pp. 423–428.

[149] Shin Ichi Ohkoshi et al. “Humidity-induced magnetization and magnetic pole inversion in a cyano-bridged metal assembly”. In: *Nat. Mater.* 3.12 (2004), pp. 857–861.

[150] Raquel Garde, Françoise Villain, and Michel Verdaguer. “Molecule-Based Room-Temperature Magnets: Catalytic Role of V(III) in the Synthesis of Vanadium-Chromium Prussian Blue Analogues”. In: *J. Am. Chem. Soc.* 124.35 (2002), pp. 10531–10538.

[151] Raquel Garde et al. “Molecule-based magnets with TC above room temperature: Improved synthesis of vanadium-chromium Prussian blue analogues with inserted alkali cations”. In: *Inorganica Chim. Acta* 361.12-13 (2008), pp. 3597–3602.

[152] S. Ferlay et al. “A Chromium-Vanadyl Ferrimagnetic Molecule-Based Magnet: Structure, Magnetism, and Orbital Interpretation”. In: *Inorg. Chem.* 38.2 (1999), pp. 229–234.

[153] Yong Hu et al. “Printing Air-Stable High- T c Molecular Magnet with Tunable Magnetic Interaction”. In: *Nano Lett.* 22.2 (2022), pp. 545–553.

[154] K. I. Pokhodnya, Arthur J Epstein, and Joel S Miller. “Thin-Film V[TCNE]x Magnets”. In: *Adv. Mater.* 12.6 (2000), pp. 410–413.

[155] D. Haskel et al. “Local structural order in the disordered vanadium tetracyanoethylene room-temperature molecule-based magnet”. In: *Phys. Rev. B - Condens. Matter Mater. Phys.* 70.5 (2004), pp. 1–9.

[156] W. B. Brinckerhoff et al. “Magnetization of High-T c Molecule-Based Magnet V/TCNE/CH 2 Cl 2”. In: *Mol. Cryst. Liq. Cryst. Sci. Technol. Sect. A. Mol. Cryst. Liq. Cryst.* 272.1 (1995), pp. 195–205.

[157] Vernon D. Neff. “Electrochemical Oxidation and Reduction of Thin Films of Prussian Blue”. In: *J. Electrochem. Soc.* 125.6 (1978), pp. 886–887.

[158] D Ellis, M Eckhoff, and V D Neff. “Electrochromism in the mixed-valence hexacyanides. 1. Voltammetric and spectral studies of the oxidation and reduction of thin films of Prussian blue”. In: *J. Phys. Chem.* 85.9 (1981), pp. 1225–1231.

[159] Kainila P. Rajan and Vernon D. Neff. “Electrochromism in the mixed-valence hexacyanides. 2. Kinetics of the reduction of ruthenium purple and Prussian blue”. In: *J. Phys. Chem.* 86.22 (1982), pp. 4361–4368.

[160] Kingo Itaya, Tatsuaki Ataka, and Shinobu Toshima. "Spectroelectrochemistry and electrochemical preparation method of Prussian blue modified electrodes". In: *J. Am. Chem. Soc.* 104.18 (1982), pp. 4767–4772.

[161] Kingo Itaya, Isamu Uchida, and Vernon D. Neff. "Electrochemistry of polynuclear transition metal cyanides: Prussian blue and its analogues". In: *Acc. Chem. Res.* 19.6 (1986), pp. 162–168.

[162] Arkady A. Karyakin. "Prussian Blue and Its Analogues: Electrochemistry and Analytical Applications". In: *Electroanalysis* 13.10 (2001), pp. 813–819.

[163] Kei Kubota et al. "Towards K-Ion and Na-Ion Batteries as "Beyond Li-Ion"". In: *Chem. Rec.* 18.4 (2018), pp. 459–479.

[164] Shobhan Dhir et al. "Outlook on K-Ion Batteries". In: *Chem* 6.10 (2020), pp. 2442–2460.

[165] Ekta Meena Bibra et al. *Global EV Outlook 2022: Securing supplies for an electric future*. Tech. rep. International Energy Agency, 2022, p. 185.

[166] A. D. McNaught and A. Wilkinson, eds. *The IUPAC Compendium of Chemical Terminology*. 2nd ed. Research Triangle Park, NC: International Union of Pure and Applied Chemistry (IUPAC), 2019.

[167] Andreas Jossen. "Fundamentals of battery dynamics". In: *J. Power Sources* 154.2 (2006), pp. 530–538.

[168] Shobhan Dhir et al. "Fundamental investigations on the ionic transport and thermodynamic properties of non-aqueous potassium-ion electrolytes". In: *Nat. Commun.* 14.1 (2023), p. 3833.

[169] K. Mizushima et al. "LixCoO2 (0<x<-1): A new cathode material for batteries of high energy density". In: *Mater. Res. Bull.* 15.6 (1980), pp. 783–789.

[170] Elsa A. Olivetti et al. "Lithium-Ion Battery Supply Chain Considerations: Analysis of Potential Bottlenecks in Critical Metals". In: *Joule* 1.2 (2017), pp. 229–243.

[171] Haegyeom Kim et al. "Next-Generation Cathode Materials for Non-aqueous Potassium-Ion Batteries". In: *Trends Chem.* 1.7 (2019), pp. 682–692.

[172] Jun Xiao et al. "Recent progress of emerging cathode materials for sodium ion batteries". In: *Mater. Chem. Front.* 5.10 (2021), pp. 3735–3764.

[173] Tianwei Yu et al. "The research and industrialization progress and prospects of sodium ion battery". In: *J. Alloys Compd.* 958 (2023), p. 170486.

[174] Jang-Yeon Hwang, Seung-Taek Myung, and Yang-Kook Sun. "Sodium-ion batteries: present and future". In: *Chem. Soc. Rev.* 46.12 (2017), pp. 3529–3614.

[175] Tomooki Hosaka et al. "Highly concentrated electrolyte solutions for 4 V class potassium-ion batteries". In: *Chem. Commun.* 54.60 (2018), pp. 8387–8390.

[176] Yongjin Fang et al. "Recent Advances in Sodium-Ion Battery Materials". In: *Electrochem. Energy Rev.* 1.3 (2018), pp. 294–323.

[177] Qingshi Meng et al. "Tuning the Closed Pore Structure of Hard Carbons with the Highest Na Storage Capacity". In: *ACS Energy Lett.* 4.11 (2019), pp. 2608–2612.

[178] Robert Usiskin et al. “Fundamentals, status and promise of sodium-based batteries”. In: *Nat. Rev. Mater.* 6.11 (2021), pp. 1020–1035.

[179] Sun Il Park et al. “Electrochemical Properties of NaTi2(PO4)3 Anode for Rechargeable Aqueous Sodium-Ion Batteries”. In: *J. Electrochem. Soc.* 158.10 (2011), A1067.

[180] Duan Bin et al. “Progress in Aqueous Rechargeable Sodium-Ion Batteries”. In: *Adv. Energy Mater.* 8.17 (2018), pp. 1–31.

[181] Mingrui Yang et al. “Aqueous Rechargeable Sodium-Ion Batteries: From Liquid to Hydrogel”. In: *Batteries* 8.10 (2022).

[182] Yibo Li et al. “An ultra-long life aqueous full K-ion battery”. In: *J. Mater. Chem. A* 9.5 (2021), pp. 2822–2829.

[183] Xiao Zhang et al. “Recent advances and perspectives in aqueous potassium-ion batteries”. In: *Energy Environ. Sci.* 15.9 (2022), pp. 3750–3774.

[184] Kevin Hurlbutt et al. “Origin of the High Specific Capacity in Sodium Manganese Hexacyanomanganate”. In: *Chem. Mater.* 34.10 (2022), pp. 4336–4343.

[185] Fritz Scholz and Aleš Dostal. “The Formal Potentials of Solid Metal Hexacyanometalates”. In: *Angew. Chemie Int. Ed. English* 34.23/24 (1995), pp. 2685–2687.

[186] Colin D. Wessells et al. “The Effect of Insertion Species on Nanostructured Open Framework Hexacyanoferrate Battery Electrodes”. In: *J. Electrochem. Soc.* 159.2 (2011), A98–A103.

[187] Jeongsik Yun, Jonas Pfisterer, and Aliaksandr S. Bandarenka. “How simple are the models of Na intercalation in aqueous media?” In: *Energy Environ. Sci.* 9.3 (2016), pp. 955–961.

[188] Richard Y. Wang et al. “Reversible Multivalent (Monovalent, Divalent, Trivalent) Ion Insertion in Open Framework Materials”. In: *Adv. Energy Mater.* 5.12 (2015), p. 1401869.

[189] Chen Ling, Jiajun Chen, and Fuminori Mizuno. “First-Principles Study of Alkali and Alkaline Earth Ion Intercalation in Iron Hexacyanoferrate: The Important Role of Ionic Radius”. In: *J. Phys. Chem. C* 117.41 (2013), pp. 21158–21165.

[190] Yutaka Moritomo et al. “Size Dependent Cation Channel in Nanoporous Prussian Blue Lattice”. In: *Appl. Phys. Express* 2.8 (2009), p. 085001.

[191] Masamitsu Takachi, Yuya Fukuzumi, and Yutaka Moritomo. “Na + diffusion kinetics in nanoporous metal-hexacyanoferrates”. In: *Dalt. Trans.* 45.2 (2016), pp. 458–461.

[192] Colin D. Wessells et al. “Nickel Hexacyanoferrate Nanoparticle Electrodes For Aqueous Sodium and Potassium Ion Batteries”. In: *Nano Lett.* 11.12 (2011), pp. 5421–5425.

[193] Colin D. Wessells, Robert A. Huggins, and Yi Cui. “Copper hexacyanoferrate battery electrodes with long cycle life and high power”. In: *Nat. Commun.* 2.1 (2011), p. 550.

[194] Ji-Hoon Lee et al. “Metal-Organic Framework Cathodes Based on a Vanadium Hexacyanoferrate Prussian Blue Analogue for High-Performance Aqueous Rechargeable Batteries”. In: *Adv. Energy Mater.* 7.2 (2017), p. 1601491.

[195] Tomoyuki Matsuda, Masamitsu Takachi, and Yutaka Moritomo. “A sodium manganese ferrocyanide thin film for Na-ion batteries”. In: *Chem. Commun.* 49.27 (2013), p. 2750.

[196] Angelo Mullaliu et al. “Highlighting the Reversible Manganese Electroactivity in Na-Rich Manganese Hexacyanoferrate Material for Li- and Na-Ion Storage”. In: *Small Methods* 4.1 (2020), p. 1900529.

[197] Yun Tang et al. “Investigation of alkali-ion (Li, Na and K) intercalation in manganese hexacyanoferrate KxMnFe(CN)6 as cathode material”. In: *Chem. Eng. J.* 396.March (2020), p. 125269.

[198] Masamitsu Takachi, Tomoyuki Matsuda, and Yutaka Moritomo. “Redox Reactions in Prussian Blue Analogue Films with Fast Na + Intercalation”. In: *Jpn. J. Appl. Phys.* 52.9R (2013), p. 090202.

[199] Masamitsu Takachi, Tomoyuki Matsuda, and Yutaka Moritomo. “Cobalt Hexacyanoferrate as Cathode Material for Na + Secondary Battery”. In: *Appl. Phys. Express* 6.2 (2013), p. 025802.

[200] Xianyong Wu et al. “Highly Crystallized Na 2 CoFe(CN) 6 with Suppressed Lattice Defects as Superior Cathode Material for Sodium-Ion Batteries”. In: *ACS Appl. Mater. Interfaces* 8.8 (2016), pp. 5393–5399.

[201] Long Wang et al. “Rhombohedral Prussian White as Cathode for Rechargeable Sodium-Ion Batteries”. In: *J. Am. Chem. Soc.* 137.7 (2015), pp. 2548–2554.

[202] Guang He and Linda F. Nazar. “Crystallite Size Control of Prussian White Analogues for Nonaqueous Potassium-Ion Batteries”. In: *ACS Energy Lett.* 2.5 (2017), pp. 1122–1127.

[203] Zhilong Shen et al. “Na-Rich Prussian White Cathodes for Long-Life Sodium-Ion Batteries”. In: *ACS Sustain. Chem. Eng.* 6.12 (2018), pp. 16121–16129.

[204] Cheryldine Q. X. Lim and Zhi-Kuang Tan. “Prussian White with Near-Maximum Specific Capacity in Sodium-Ion Batteries”. In: *ACS Appl. Energy Mater.* 4.6 (2021), pp. 6214–6220.

[205] Radu Bors et al. “Chromium(II) Hexacyanoferrate-Based Thin Films as a Material for Aqueous Alkali Metal Cation Batteries”. In: *ACS Omega* 3.5 (2018), pp. 5111–5115.

[206] Dominika Baster et al. “Sodium chromium hexacyanoferrate as a potential cathode material for aqueous sodium-ion batteries”. In: *Chem. Commun.* 55.97 (2019), pp. 14633–14636.

[207] Liang Chen et al. “Water-mediated cation intercalation of open-framework indium hexacyanoferrate with high voltage and fast kinetics”. In: *Nat. Commun.* 7.1 (2016), p. 11982.

[208] H. Huang, S.-C. Yin, and L. F. Nazar. “Approaching Theoretical Capacity of LiFePO[sub 4] at Room Temperature at High Rates”. In: *Electrochem. Solid-State Lett.* 4.10 (2001), A170.

[209] G. X. Wang et al. “A study on LiFePO4 and its doped derivatives as cathode materials for lithium-ion batteries”. In: *J. Power Sources* 159.1 SPEC. ISS. (2006), pp. 282–286.

[210] Aijun Zhou et al. “Hexacyanoferrate-Type Prussian Blue Analogs: Principles and Advances Toward High-Performance Sodium and Potassium Ion Batteries”. In: *Adv. Energy Mater.* 2000943 (2020), p. 2000943.

[211] Xinyi Liu, Yu Cao, and Jie Sun. “Defect Engineering in Prussian Blue Analogs for High-Performance Sodium-Ion Batteries”. In: *Adv. Energy Mater.* 12.46 (2022), p. 2202532.

[212] Zhuo-Er Yu et al. “A vacancy-free sodium manganese hexacyanoferrate as cathode for sodium-ion battery by high-salt-concentration preparation”. In: *J. Alloys Compd.* 887 (2021), p. 161388.

[213] Aijun Zhou et al. “Size-, Water-, and Defect-Regulated Potassium Manganese Hexacyanoferrate with Superior Cycling Stability and Rate Capability for Low-Cost Sodium-Ion Batteries”. In: *Small* 15.42 (2019), p. 1902420.

[214] Yuhao Lu et al. “Prussian blue: a new framework of electrode materials for sodium batteries”. In: *Chem. Commun.* 48.52 (2012), p. 6544.

[215] Jie Song et al. “Removal of Interstitial H 2 O in Hexacyanometallates for a Superior Cathode of a Sodium-Ion Battery”. In: *J. Am. Chem. Soc.* 137.7 (2015), pp. 2658–2664.

[216] David N. Hume and I. M. Kolthoff. “The Oxidation Potential of the Chromocyanide—Chromicyanide Couple and the Polarography of the Chromium Cyanide Complexes 1”. In: *J. Am. Chem. Soc.* 65.10 (1943), pp. 1897–1901.

[217] Ales Dostal, Uwe Schroeder, and Fritz Scholz. “Electrochemistry of Chromium(II) Hexacyanochromate(III) and Electrochemically Induced Isomerization of Solid Iron(II) Hexacyanochromate(III) Mechanically Immobilized on the Surface of a Graphite Electrode”. In: *Inorg. Chem.* 34.7 (1995), pp. 1711–1717.

[218] Ali Firouzi et al. “Monovalent manganese based anodes and co-solvent electrolyte for stable low-cost high-rate sodium-ion batteries”. In: *Nat. Commun.* 9.1 (2018), p. 861.

[219] Kosuke Nakamoto et al. “Over 2 V Aqueous Sodium-Ion Battery with Prussian Blue-Type Electrodes”. In: *Small Methods* 3.4 (2019), pp. 3–7.

[220] Kevin Hurlbutt. “Modeling the Prussian blue analogs from first principles for battery applications”. Ph.D. thesis. University of Oxford, 2021.

[221] Junsheng Chen et al. “High-energy-density aqueous sodium-ion batteries enabled by chromium hexacycnochromate anodes”. In: *Chem. Eng. J.* 415.January (2021), p. 129003.

[222] Ma José Piernas-Muñoz et al. “K1-xFe2+x/3(CN)6 · yH2O, Prussian Blue as a displacement anode for lithium ion batteries”. In: *J. Power Sources* 271 (2014), pp. 489–496.

[223] Peixun Xiong et al. “Prussian blue analogues Mn[Fe(CN) 6] 0.6667 · nH 2 O cubes as an anode material for lithium-ion batteries”. In: *Dalt. Trans.* 44.38 (2015), pp. 16746–16751.

[224] Ping Nie et al. “Prussian blue analogues: a new class of anode materials for lithium ion batteries”. In: *J. Mater. Chem. A* 2.16 (2014), pp. 5852–5857.

[225] Takayuki Shibata, Masamitsu Takachi, and Yutaka Moritomo. “Low Voltage Charge/Discharge Behavior of Manganese Hexacyanoferrate”. In: *Batteries* 3.4 (2017), p. 7.

[226] Erich H Kisi and Christopher J Howard. *Applications of Neutron Powder Diffraction*. 2008.

[227] B D Cullity and S R Stock. *Elements of X-Ray Diffraction*. 3rd ed. Essex: Pearson Education, Limited, 2013.

[228] C. Suryanarayana and M. Grant Norton. *X-Ray Diffraction : A Practical Approach*. 1st ed. New York: Springer, 1998.

[229] John M. Cowley. “Radiations and their scattering by matter”. In: *Diffr. Phys.* 3rd ed. Amsterdam: Elsevier, 1995, pp. 77–92.

[230] H. M. Rietveld. “A profile refinement method for nuclear and magnetic structures”. In: *J. Appl. Crystallogr.* 2.2 (1969), pp. 65–71.

[231] R A Young. *The Rietveld Method*. Oxford: Oxford University Press, 1993.

[232] Brian H. Toby. “R factors in Rietveld analysis: How good is good enough?” In: *Powder Diffr.* 21.1 (2006), pp. 67–70.

[233] Brian H. Toby and Robert B. Von Dreele. “GSAS-II : the genesis of a modern open-source all purpose crystallography software package”. In: *J. Appl. Crystallogr.* 46.2 (2013), pp. 544–549.

[234] Laurent C. Chapon et al. “Wish: The New Powder and Single Crystal Magnetic Diffractometer on the Second Target Station”. In: *Neutron News* 22.2 (2011), pp. 22–25.

[235] Juan Rodriguez-Carvajal. “FULLPROF: a program for Rietveld refinement and pattern matching analysis”. In: *Satell. Meet. powder Diffr. XV Congr. IUCr.* Toulouse, France, 1990.

[236] Takeshi Hasegawa. *Quantitative Infrared Spectroscopy for Understanding of a Condensed Matter*. Tokyo: Springer Japan, 2017.

[237] Peter J. Larkin. “Basic Principles”. In: *Infrared Raman Spectrosc.* Elsevier, 2018, pp. 7–28.

[238] Max Diem. *Modern Vibrational Spectroscopy and Micro-Spectroscopy : Theory, Instrumentation and Biomedical Applications*. John Wiley & Sons, 2015.

[239] Peter J. Larkin. “Instrumentation and Sampling Methods”. In: *Infrared Raman Spectrosc.* Elsevier, 2018, pp. 29–61.

[240] Jaroslav Sestak. “Understanding of temperature, heat, gradients and related thermodynamics”. In: *Therm. Anal. Thermodyn. Prop. Solids*. Elsevier, 2021, pp. 25–59.

[241] Peter G Laye. “Differential Thermal Analysis and Differential Scanning Calorimetry”. In: *Princ. Therm. Anal. Calorim.* Ed. by Peter Haines. The Royal Society of Chemistry, 2002, pp. 55–93.

[242] Howard E. Taylor. "Inductively Coupled Plasmas". In: *Inductively Coupled Plasma-Mass Spectrom.* Elsevier, 2001, pp. 15–27.

[243] Robert Thomas. *Practical Guide to ICP-MS : A Tutorial for Beginners.* 3rd ed. Taylor & Francis Group, 2013.

[244] Michael A. Rutzke. "Atomic Absorption, Inductively Coupled Plasma Optical Emission Spectroscopy, and Infrared Spectroscopy". In: *Encycl. Geochemistry.* Ed. by William M White. Springer, Cham, 2018, pp. 76–83.

[245] Gerhard A. Meyer. "ICP: still the panacea for trace metals analysis?" In: *Anal. Chem.* 59.23 (1987), 1345A–1354A.

[246] John W Olesik. "Elemental analysis using ICP-OES and ICP/MS". In: *Anal. Chem.* 63.1 (1991), 12A–21A.

[247] Geoff Tyler. *ICP Optical Emission Spectroscopy Technical Note 5: ICP-OES, ICP-MS and AAS Techniques Compared.* Tech. rep. Jobin Yvon S.A.S, Horiba Group, 1995.

[248] Tomoko Ariga et al. "Cold Plasma: Effective Control of Argon Emission Line Interferences on the Measurement of Rubidium by Axial-view ICP-OES". In: *Chem. Lett.* 46.12 (2017), pp. 1751–1753.

[249] Anwar Ul-Hamid. *A Beginners' Guide to Scanning Electron Microscopy.* Cham: Springer International Publishing, 2018.

[250] Ludwig Reimer. *Scanning Electron Microscopy.* Vol. 45. Springer Series in Optical Sciences. Berlin, Heidelberg: Springer Berlin Heidelberg, 1998.

[251] R. L. Fagaly. "Superconducting quantum interference device instruments and applications". In: *Rev. Sci. Instrum.* 77 (2006), p. 101101.

[252] Randy K. Dumas and Tom Hogan. "Recent Advances in SQUID Magnetometry". In: *Magn. Meas. Tech. Mater. Charact.* Ed. by V. Franco and B Dodrill. Cham: Springer International Publishing, 2021, pp. 39–62.

[253] R. K. Zheng et al. "The origin of the non-monotonic field dependence of the blocking temperature in magnetic nanoparticles". In: *J. Phys. Condens. Matter* 18.26 (2006), pp. 5905–5910.

[254] H. Mamiya et al. "Extraction of blocking temperature distribution from zero-field-cooled and field-cooled magnetization curves". In: *IEEE Trans. Magn.* 41.10 (2005), pp. 3394–3396.

[255] P. A. Joy, P S Anil Kumar, and S. K. Date. "The relationship between field-cooled and zero-field-cooled susceptibilities of some ordered magnetic systems". In: *J. Phys. Condens. Matter* 10.48 (1998), pp. 11049–11054.

[256] Sam Mugiraneza and Alannah M. Hallas. "Tutorial: a beginner's guide to interpreting magnetic susceptibility data with the Curie-Weiss law". In: *Commun. Phys.* 5.1 (2022), p. 95.

[257] Elangbam Chitra Devi and Shougaijam Dorendrajit Singh. "Tracing the Magnetization Curves: a Review on Their Importance, Strategy, and Outcomes". In: *J. Supercond. Nov. Magn.* 34.1 (2021), pp. 15–25.

[258] E. L. Fertman et al. "Exchange bias phenomenon in (Nd1- x Y x)2/3Ca1/3MnO3 (x = 0, 0.1) perovskites". In: *Low Temp. Phys.* 41.12 (2015), pp. 1001–1005.

[259] Yue Ma, Jun Ma, and Guanglei Cui. "Small things make big deal: Powerful binders of lithium batteries and post-lithium batteries". In: *Energy Storage Mater.* 20.November 2018 (2019), pp. 146–175.

[260] György Inzelt. "Pseudo-reference Electrodes". In: *Handb. Ref. Electrodes*. Berlin, Heidelberg: Springer Berlin Heidelberg, 2013, pp. 331–332.

[261] D. I. Iermakova et al. "On the Comparative Stability of Li and Na Metal Anode Interfaces in Conventional Alkyl Carbonate Electrolytes". In: *J. Electrochem. Soc.* 162.13 (2015), A7060–A7066.

[262] Joanna Conder and Claire Villevieille. "How reliable is the Na metal as a counter electrode in Na-ion half cells?" In: *Chem. Commun.* 55.9 (2019), pp. 1275–1278.

[263] Lukas Schafzahl et al. "An Electrolyte for Reversible Cycling of Sodium Metal and Intercalation Compounds". In: *ChemSusChem* 10.2 (2017), pp. 401–408.

[264] Jaegi Lee et al. "Ultraconcentrated sodium bis(fluorosulfonyl)imide-based electrolytes for high-performance sodium metal batteries". In: *ACS Appl. Mater. Interfaces* 9.4 (2017), pp. 3723–3732.

[265] Tomooki Hosaka et al. "Potassium Metal as Reliable Reference Electrodes of Nonaqueous Potassium Cells". In: *J. Phys. Chem. Lett.* 10.12 (2019), pp. 3296–3300.

[266] Neng Xiao, William D. McCulloch, and Yiying Wu. "Reversible Dendrite-Free Potassium Plating and Stripping Electrochemistry for Potassium Secondary Batteries". In: *J. Am. Chem. Soc.* 139.28 (2017), pp. 9475–9478.

[267] Gary A. Mabbott. "An introduction to cyclic voltammetry". In: *J. Chem. Educ.* 60.9 (1983), pp. 697–702.

[268] Noémie Elgrishi et al. "A Practical Beginner's Guide to Cyclic Voltammetry". In: *J. Chem. Educ.* 95.2 (2018), pp. 197–206.

[269] Allen J. Bard and Larry R. Faulkner. *Electrochemical methods : fundamentals and applications*. Second edi. New York: Wiley, 2001.

[270] Jarred Z. Olson, Carmen M. López, and Edmund J.F. Dickinson. "Differential Analysis of Galvanostatic Cycle Data from Li-Ion Batteries: Interpretative Insights and Graphical Heuristics". In: *Chem. Mater.* 35.4 (2023), pp. 1487–1513.

[271] Steven K. MacLeod. "Moisture determination using Karl Fischer titrations". In: *Anal. Chem.* 63.10 (1991), 557A–566A.

[272] P J Hore. *Nuclear magnetic resonance*. eng. Second. Oxford chemistry primers. Oxford: Oxford University Press, 2015.

[273] Samuel Wheeler. "Prussian blue analogue materials for energy storage applications". Ph.D. thesis. University of Oxford, 2020.

[274] Stephen F. Lincoln. "Mechanistic Studies of Metal Aqua Ions: A Semi-Historical Perspective". In: *Helv. Chim. Acta* 88.3 (2005), pp. 523–545.

[275] Odin T Christensen. "Ueber die Darstellung der dem rothen und dem gelben Blutlaugensalz analogen Chrom-und Manganverbindungen". In: *J. für Prakt. Chemie* 31.1 (1885), pp. 163–173.

[276] David N. Hume and Hosmer W. Stone. "The Preparation and Magnetic Properties of Some Complex Compounds of Divalent Chromium". In: *J. Am. Chem. Soc.* 63.5 (1941), pp. 1200–1203.

[277] Kendric J. Nelson et al. "The Myth of Cyanide Always Being a Strong-Field Ligand: Synthesis and Structural Characterization of HomolepticS=2 Pentacyanochromate(II), [CrII(CN)5]3-, and Nonacyanodichromate(II), [(CN)9]5-". In: *Angew. Chemie Int. Ed.* 44.20 (2005), pp. 3129–3132.

[278] Richard L. Lord and Mu Hyun Baik. "Why does cyanide pretend to be a weak field ligand in [Cr(CN) 5]3-?" In: *Inorg. Chem.* 47.10 (2008), pp. 4413–4420.

[279] Robert J. Deeth. "A Theoretical Rationale for the Formation, Structure and Spin State of Pentacyanochromate(II)". In: *Eur. J. Inorg. Chem.* 2006.13 (2006), pp. 2551–2555.

[280] O. Sato et al. "Electrochemically Tunable Magnetic Phase Transition in a High- T c Chromium Cyanide Thin Film". In: *Science* 271.5245 (1996), pp. 49–51.

[281] Osamu Sato et al. "Electrochemical Syntheses and Electrochromic Properties of Chromium Cyanide Magnetic Thin Films". In: *Chem. Lett.* 26.1 (1997), pp. 37–38.

[282] Wayne E. Buschmann et al. "Magnetic field induced reversed (Negative) magnetization for electrochemically deposited Tc = 260 K Oxidized Films of Chromium Cyanide Magnets". In: *Adv. Mater.* 9.8 (1997), pp. 645–647.

[283] A. L. Patterson. "The scherrer formula for X-ray particle size determination". In: *Phys. Rev.* 56.10 (1939), pp. 978–982.

[284] J W Mullin. *Crystallization*. 4th ed. Oxford: Elsevier Science & Technology, 2001.

[285] Vien Vo et al. "A new route for obtaining Prussian blue nanoparticles". In: *Mater. Chem. Phys.* 107.1 (2008), pp. 6–8.

[286] Akira Takahashi et al. "Unveiling Cs-adsorption mechanism of Prussian blue analogs: Cs + -percolation via vacancies to complete dehydrated state". In: *RSC Adv.* 8.61 (2018), pp. 34808–34816.

[287] D. E. DeGraaf and G. B. B. M. Sutherland. "Vibrational Spectrum of N-Methyl Formamide". In: *J. Chem. Phys.* 26.3 (1957), pp. 716–717.

[288] E. Reguera et al. "On the low stability of molecular magnets based on transition metal hexacyanochromates (III)". In: *Zeitschrift fur Phys. Chemie* 224.6 (2010), pp. 807–826.

[289] Zdeněk Samec and Karl Doblhofer. "Mechanism of peroxodisulfate reduction at a polycrystalline gold electrode". In: *J. Electroanal. Chem.* 367.1-2 (1994), pp. 141–147.

[290] Petr Vanýsek. "Electrochemical Series". In: *CRC Handb. Chem. Phys.* Ed. by W M Haynes, D R Lide, and T J Bruno. 95th ed. Boca Raton: CRC Press, 2014, pp. 5–80.

[291] Julia M. Kurth, Christiane Dahl, and Julea N. Butt. "Catalytic Protein Film Electrochemistry Provides a Direct Measure of the Tetrathionate/Thiosulfate Reduction Potential". In: *J. Am. Chem. Soc.* 137.41 (2015), pp. 13232–13235.

[292] M. Okubo et al. “Switching Redox-Active Sites by Valence Tautomerism in Prussian Blue Analogues A x Mn y [Fe(CN) 6] · n H 2 O (A: K, Rb): Robust Frameworks for Reversible Li Storage”. In: *J. Phys. Chem. Lett.* 1.14 (2010), pp. 2063–2071.

[293] Aleš Dostal et al. “Lattice contractions and expansions accompanying the electrochemical conversions of Prussian blue and the reversible and irreversible insertion of rubidium and thallium ions”. In: *J. Electroanal. Chem.* 406.1-2 (1996), pp. 155–163.

[294] *Formamide, N-methyl-*.

[295] Stephen M. Holmes. “MOLECULE-BASED MAGNETS CONSTRUCTED FROM HEXACYANOMETALATES”. PhD thesis. University of Illinois at Urbana-Champaign, 1999.

[296] Eugenio Coronado et al. “Magneto-Optical Properties of Electrodeposited Thin Films of the Molecule-Based Magnet Cr5.5(CN)12 · 11.5H2O”. In: *Adv. Mater.* 23.37 (2011), pp. 4323–4326.

[297] Helena Prima-Garcia et al. “Tailoring magnetic properties of electrodeposited thin films of the molecule-based magnet Cr5.5(CN)12 11.5H2O”. In: *Nanoscale Res. Lett.* 7.1 (2012), p. 232.

[298] Kingo Itaya, Haruo Akahoshi, and Shinobu Toshima. “Electrochemistry of Prussian Blue Modified Electrodes: An Electrochemical Preparation Method”. In: *J. Electrochem. Soc.* 129.7 (1982), pp. 1498–1500.

[299] Kingo Itaya and Isamu Uchida. “Nature of intervalence charge-transfer bands in Prussian blues”. In: *Inorg. Chem.* 25.3 (1986), pp. 389–392.

[300] Hochun Lee et al. “Anion Transport in Prussian Blue Films in Acetonitrile and Propylene Carbonate Solutions”. In: *J. Electrochem. Soc.* 147.10 (2000), p. 3801.

[301] David Basset Brown, Duward F. Shriver, and Lyle Howard Schwartz. “Solid-state reactions of iron(II) hexacyanochromate(III)”. In: *Inorg. Chem.* 7.1 (1968), pp. 77–83.

[302] David Basset Brown and Duward F. Shriver. “Structures and solid-state reactions of Prussian blue analogs containing chromium, manganese, iron, and cobalt”. In: *Inorg. Chem.* 8.1 (1969), pp. 37–42.

[303] E Reguera, J.A. Bertrán, and L. Nuñez. “Study of the linkage isomerization process in hexacyanometallates”. In: *Polyhedron* 13.10 (1994), pp. 1619–1624.

[304] Ali Eftekhari. “A high-voltage solid-state secondary cell based on chromium hexacyanometallates”. In: *J. Power Sources* 117.1-2 (2003), pp. 249–254.

[305] M. J. Benitez et al. “Fingerprinting the magnetic behavior of antiferromagnetic nanostructures using remanent magnetization curves”. In: *Phys. Rev. B - Condens. Matter Mater. Phys.* 83.13 (2011), pp. 1–9.

[306] Louis Néel. “Superparamagnétisme des grains très fins antiferromagnétiques”. In: *Comptes Rendus Hebd. Des Seances L Acad. Des Sci.* 252.26 (1961), pp. 4075–4080.

[307] James T. Richardson and W. O. Milligan. “Magnetic Properties of Colloidal Nickelous Oxide”. In: *Phys. Rev.* 102.5 (1956), pp. 1289–1294.

[308] W. J. Schuele and V. D. Deetscreek. "Appearance of a Weak Ferromagnetism in Fine Particles of Antiferromagnetic Materials". In: *J. Appl. Phys.* 33.3 (1962), pp. 1136–1137.

[309] R. W. Chantrell et al. "Calculations of the susceptibility of interacting superparamagnetic particles". In: *Phys. Rev. B* 63.2 (2000), p. 024410.

[310] Yoann Prado et al. "Tailored coordination nanoparticles: Assessing the magnetic single-domain critical size". In: *Chem. Commun.* 47.3 (2011), pp. 1051–1053.

[311] Yoann Prado et al. "Magnetization Reversal in CsNi II Cr III (CN) 6 Coordination Nanoparticles: Unravelling Surface Anisotropy and Dipolar Interaction Effects". In: *Adv. Funct. Mater.* 24.34 (2014), pp. 5402–5411.

[312] Steen Mørup et al. "Experimental and theoretical studies of nanoparticles of antiferromagnetic materials". In: *J. Phys. Condens. Matter* 19.21 (2007), pp. 1–31.

[313] N.P. Grazhdankina. "Magnetic first order phase transitions". In: *Uspekhi Fiz. Nauk* 96.10 (1968), pp. 291–325.

[314] Yuka Kawamoto et al. "Thermodynamic investigation by heat capacity measurements of ferrimagnetic A2Mn[Mn(CN)6] (A=K, Rb, Cs) Prussian blue compounds". In: *J. Phys. Condens. Matter* 26.1 (2014).

[315] X. G. Zheng et al. "Finite-size effect on Néel temperature in antiferromagnetic nanoparticles". In: *Phys. Rev. B* 72.1 (2005), p. 014464.

[316] Huwei Wang et al. "Highly stable potassium metal batteries enabled by regulating surface chemistry in ether electrolyte". In: *Energy Storage Mater.* 42.July (2021), pp. 526–532.

[317] Marcin A. Malik et al. "Countercation intercalation and kinetics of charge transport during redox reactions of nickel hexacyanoferrate". In: *Electrochim. Acta* 49.25 (2004), pp. 4253–4258.

[318] Arkadiy Simonov et al. "Hidden diversity of vacancy networks in Prussian blue analogues". In: *Nature* 578.7794 (2020), pp. 256–260. arXiv: 1908.10596.

[319] Xinying Xie et al. "Microfluidic synthesis as a new route to produce novel functional materials". In: *Biomicrofluidics* 16.4 (2022).

[320] Naoaki Yabuuchi and Shinichi Komaba. "Recent research progress on iron- and manganese-based positive electrode materials for rechargeable sodium batteries". In: *Sci. Technol. Adv. Mater.* 15.4 (2014), p. 043501.

[321] Sascha Keßler et al. "Synthesis of nickel hexacyanoferrate nanocubes with tuneable dimensions via temperature-controlled Ni 2+ -citrate complexation". In: *Chem. Commun.* 56.92 (2020), pp. 14439–14442.

[322] Anne Bleuzen et al. "Photoinduced Ferrimagnetic Systems in Prussian Blue Analogues C I x Co 4 [Fe(CN) 6] y (C I = Alkali Cation). 1. Conditions to Observe the Phenomenon". In: *J. Am. Chem. Soc.* 122.28 (2000), pp. 6648–6652.

[323] Ya You et al. "Sodium iron hexacyanoferrate with high Na content as a Na-rich cathode material for Na-ion batteries". In: *Nano Res.* 8.1 (2015), pp. 117–128.

[324] María José Piernas-Muñoz et al. "Higher voltage plateau cubic Prussian White for Na-ion batteries". In: *J. Power Sources* 324 (2016), pp. 766–773.

[325] Naonobu Shimamoto et al. “Control of Charge-Transfer-Induced Spin Transition Temperature on Cobalt-Iron Prussian Blue Analogues”. In: *Inorg. Chem.* 41.4 (2002), pp. 678–684.

[326] S. Liu et al. “Copper hexacyanoferrate nanoparticles as cathode material for aqueous Al-ion batteries”. In: *J. Mater. Chem. A* 3.3 (2015), pp. 959–962.

[327] J. F. KEGGIN and F. D. MILES. “Structures and Formulæ of the Prussian Blues and Related Compounds”. In: *Nature* 137.3466 (1936), pp. 577–578.

[328] R. Martínez-García et al. “Crystal structures of some manganese(II) and cadmium hexacyanoferrates (II,III) and structural transformations related to the sorption of Cesium”. In: *Powder Diffr.* 19.3 (2004), pp. 255–264.

[329] Surendra Nath Ghosh. “Infrared spectra of the Prussian blue analogs”. In: *J. Inorg. Nucl. Chem.* 36.11 (1974), pp. 2465–2466.

[330] Huan Pang et al. “Uniform manganese hexacyanoferrate hydrate nanocubes featuring superior performance for low-cost supercapacitors and nonenzymatic electrochemical sensors”. In: *Nanoscale* 7.38 (2015), pp. 16012–16019.

[331] S Ohkoshi, H Tokoro, and K Hashimoto. “Temperature- and photo-induced phase transition in rubidium manganese hexacyanoferrate”. In: *Coord. Chem. Rev.* 249.17-18 (2005), pp. 1830–1840.

[332] A. Ludi and H. U. Güdel. “Die Struktur der Hydrate von Co 3 [Co(CN) 6] 2 und Cd 3 [Co(CN) 6] 2”. In: *Helv. Chim. Acta* 51.8 (1968), pp. 2006–2016.

[333] G. W. Beall et al. “Crystal structure of trimanganese bis(hexakis(cyano)cobaltate) dodecahydrate and tricadmium bis(hexakis(cyano)cobaltate) dodecahydrate by neutron and x-ray diffraction”. In: *Inorg. Chem.* 16.11 (1977), pp. 2715–2718.

[334] N. Karikalan et al. “A copper hexacyanocobaltate nanocubes based dopamine sensor in the presence of ascorbic acid”. In: *RSC Adv.* 6.54 (2016), pp. 48523–48529.

[335] Angelo Mullaliu et al. “Operando XAFS and XRD Study of a Prussian Blue Analogue Cathode Material: Iron Hexacyanocobaltate”. In: *Condens. Matter* 3.4 (2018), p. 36.

[336] Paul A. Haas. “A Review of Information on Ferrocyanide Solids for Removal of Cesium from Solutions”. In: *Sep. Sci. Technol.* 28.17-18 (1993), pp. 2479–2506.

[337] Pauline Higel et al. “Solid-state magnetic switching triggered by proton-coupled electron-transfer assisted by long-distance proton-alkali cation transport”. In: *J. Am. Chem. Soc.* 136.17 (2014), pp. 6231–6234.